The Astrophysical Journal, 836:76 (37pp), 2017 February 10 https://doi.org/10.3847/1538-4357/836/1/76

Powerful H_2 Line Cooling in Stephan's Quintet. II. Group-wide Gas and Shock Modeling of the Warm H_2 and a Comparison with [C II] 157.7 μm Emission and Kinematics

P. N. Appleton[1], P. Guillard[2], A. Togi[3], K. Alatalo[4,10], F. Boulanger[5], M. Cluver[6], G. Pineau des Forêts[5,7], U. Lisenfeld[8], P. Ogle[9], and C. K. Xu[1,9]

[1] NASA *Herschel*Science Center, IPAC, Caltech, 770S Wilson Av., Pasadena, CA 91125, USA; apple@ipac.caltech.edu
[2] Sorbonne Universités, UPMC Univ. Paris 6 et CNRS, UMR 7095, Institut d'Astrophysique de Paris, 98 bis Bd Arago, F-75014 Paris, France
[3] Department of Physics and Astronomy, The University of Toledo, 2825 West Bancroft Street, Toledo, OH 43606, USA
[4] Observatories of the Carnegie Institution for Science, 813 Santa Barbara Street, Pasadena, CA 91101, USA
[5] Institut d'Astrophysique Spatiale, F-91405 Orsay, Université Paris Sud et CNRS, France
[6] Department of Physics and Astronomy, University of Western Cape, Robert Sobukwe Road, Bellville, 7535, South Africa
[7] DAEC, Observatoire de Paris, F-92195 Meudon Principal Cedex, France
[8] Departamento de Física Teorica y del Cosmos, Universidad de Granada, Spain and Instituto Carlos I de Física Teorica y Computacional, Facultad de Ciencias, E-18071 Granada, Spain
[9] NASA Extragalactic Database, IPAC, Caltech, 1200 E. California Boulevard, Caltech, Pasadena, CA 91125, USA
Received 2016 September 8; revised 2016 December 21; accepted 2017 January 10; published 2017 February 9

Abstract

We map for the first time the two-dimensional H_2 excitation of warm intergalactic gas in Stephan's Quintet on group-wide (50×35 kpc^2) scales to quantify the temperature, mass, and warm H_2 mass fraction as a function of position using *Spitzer*. Molecular gas temperatures are seen to rise (to $T > 700$ K) and the slope of the power-law density–temperature relation flattens along the main ridge of the filament, defining the region of maximum heating. We also performed MHD modeling of the excitation properties of the warm gas, to map the velocity structure and energy deposition rate of slow and fast molecular shocks. Slow magnetic shocks were required to explain the power radiated from the lowest-lying rotational states of H_2, and strongly support the idea that energy cascades down to small scales and low velocities from the fast collision of NGC 7318b with group-wide gas. The highest levels of heating of the warm H_2 are strongly correlated with the large-scale stirring of the medium as measured by [C II] spectroscopy with *Herschel*. H_2 is also seen associated with a separate bridge that extends toward the Seyfert nucleus in NGC 7319, from both *Spitzer* and CARMA CO observations. This opens up the possibility that both galaxy collisions and outflows from active galactic nuclei can turbulently heat gas on large scales in compact groups. The observations provide a laboratory for studying the effects of turbulent energy dissipation on group-wide scales, which may provide clues about the heating and cooling of gas at high z in early galaxy and protogalaxy formation.

Key words: galaxies: individual (Stephan's Quintet – NGC 7318a, NGC 7318b, NGC 7319)

1. Introduction

Stephan's Quintet (hereafter the Quintet) is one of the most studied of nearby compact groups of galaxies. Observations have been made across a wide range of the electromagnetic spectrum, from X-rays (Bahcall et al. 1984; Sulentic et al. 1995; Trinchieri et al. 2003; O'Sullivan et al. 2009), UV (Xu et al. 2005), visible light (Moles et al. 1998; Gallagher et al. 2001; Fedotov et al. 2011), IR (Sulentic et al. 2001; Cluver et al. 2010; Guillard et al. 2010; Natale et al. 2010; Suzuki et al. 2011; Bitsakis et al. 2014) to radio waves (Allen & Hartsuiker 1972; van der Hulst & Rots 1981; Xu et al. 2003; Nikiel-Wroczyński et al. 2013). These papers have revealed that much of the gas lies either in tidal tails outside the galaxies or in a large intergalactic filament. The filament, which lies between NGC 7319 and NGC 7318b, was first observed in radio continuum emission and later in X-rays. Observations strongly suggest that the gas in the filament is heated by shocks driven into the intergroup medium by the "intruder" galaxy NGC 7318b (Gao & Xu 2000; Xu et al. 2003, 2005; O'Sullivan et al. 2009; Iglesias-Páramo et al. 2012; Konstantopoulos et al. 2014; Rodríguez-Baras et al. 2014). The galaxy is likely colliding from behind the group with a blueshifted radial velocity of 800–1000 km s^{-1} with respect to the majority of the gas in the group. The Quintet has also been the subject of several detailed numerical simulations (Renaud et al. 2010; Geng et al. 2012; Hwang et al. 2012), which help to explain the H I and optical bridges and tails associated with the large Seyfert II galaxy NGC 7319, as well as the interaction of the intruder galaxy with the group (Moles et al. 1997; Sulentic et al. 1995, 2001; Williams et al. 2002).

Spitzer mid-IR spectroscopy of the filament revealed unusually bright pure-rotational emission lines of molecular hydrogen (Appleton et al. 2006; Cluver et al. 2010, hereafter Paper 1) associated with the filament. Although the observations presented in Paper 1 could not spectrally resolve the emission or accurately measure the systemic velocity, a reanalysis of the *Spitzer* Infrared Spectrograph (IRS) higher resolution ($R = 500$) data from Appleton et al. (2006) was performed to provide some limited information (see Appendix A of Paper 1). Those results showed the gas to be kinematically broad (FWHM ~ 800 km s^{-1}), and approximately centered at a velocity between that of the high-velocity intruder galaxy and the velocity of the gas in the main body of the group. This suggested that the warm H_2 is highly turbulent post-shocked gas accelerated during the encounter.

The H_2 emission defines not only the main north/south filament seen at other wavelengths, but also a second

[10] Hubble Fellow.

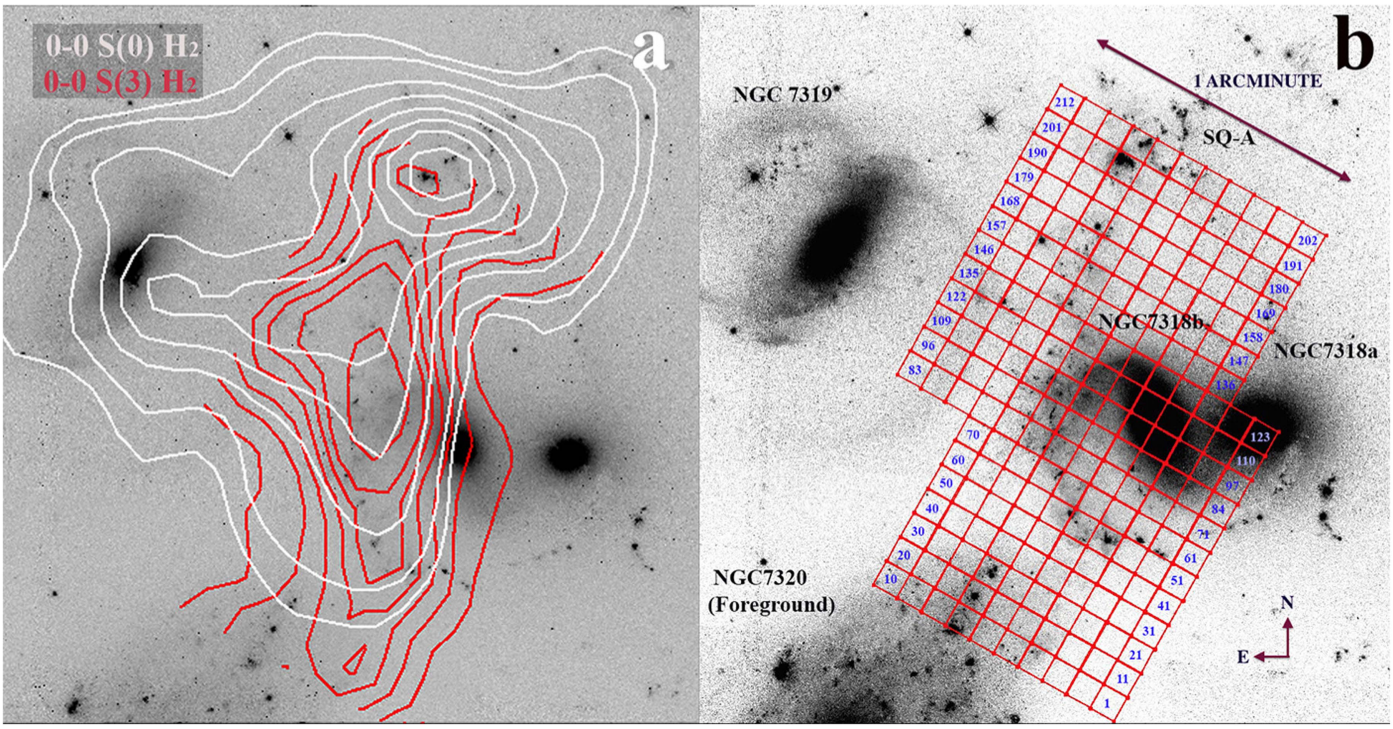

Figure 1. (a) *Spitzer* warm H_2 line maps of 0–0 S(0) 28.2 μm (white contours) and 0–0 S(3) 9.7 μm (red contours) superimposed on the *Hubble Space Telescope* (*HST*) F665N Hα image of Stephan's Quintet (see Paper 1). The 0–0 S(0) map was made in the IRS long-low module and covers a larger area than the 0–0 S(3) map, which was made in the short-low module. White contours are 0.075, 0.1, 0.15, 0.2, 0.25, 0.3, 0.35, and 0.4 MJy sr^{-1}, and red contours are 0.1, 0.2, 0.3, 0.4, 0.5, 0.6, and 0.7 MJy sr^{-1}. (b) Spectral extraction grid used in this paper to investigate the excitation of the gas over the main H_2 filament; it includes only those areas common to both the long-low and short-low modules. The numbered extraction boxes are 5.55 × 5.55 arcsec^2 (2.5 × 2.5 kpc^2 at D = 94 Mpc) in area. The background image is again the F665N *HST* image. The overall extent of the warm H_2 emission is ~50 × 35 kpc^2.

bridge-like structure, which extends eastward from the main shock toward the center of NGC 7319 (see Figure 1(a)). This possible bridge is also seen faintly in X-ray emission and extended Hα observations (Trinchieri et al. 2003; Xu et al. 2003). Based on the high values of the warm H_2/PAH (polycyclic aromatic hydrocarbons), H_2/IR, and H_2/X-ray luminosities (Paper 1), it was concluded that the main heating mechanism for the warm H_2 emission was the dissipation of mechanical energy in the shocks, channeled to small scales and low velocities by supersonic turbulence (see modeling by Guillard et al. 2009; Lesaffre et al. 2013). Recent observations of far-IR cooling lines ([C II], [O I], and H_2O) with *Herschel* (Appleton et al. 2013) show that although these lines are boosted in the filament, the dominant cooling still occurs in the low-J pure-rotational lines of H_2.

Early attempts at detecting CO (1–0) emission from the Quintet appeared to show only emission from the brightest regions in NGC 7319, and in two extragalactic star-forming regions (Gao & Xu 2000; Smith & Struck 2001; Lisenfeld et al. 2002; Petitpas & Taylor 2005). Smith & Struck (2001) also detected faint broad emission from the direction of the intruder galaxy NGC 7318b, but in retrospect this may have been the first detection of CO from the main shocked filament, which lies in the large NRAO 12 m beam.

Much deeper single-dish (Guillard et al. 2012) IRAM 30 m observations, using a broadband receiver system, revealed the presence of extensive faint CO emission from the filament with large line widths, and with as many as three different velocity components at some positions. This multiplicity of velocity components (also confirmed with optical spectroscopy of the faint ionized gas by Iglesias-Páramo et al. 2012; Konstantopoulos et al. 2014; Rodríguez-Baras et al. 2014) implies a complex interplay between the intruder galaxy's gas and the pre- and post-shocked gas lying in the group. Unfortunately, although we expect the warm H_2 emission discussed in the current paper to primarily be post-shocked gas, we do not have the velocity resolution to make a detailed comparison with the previously published spectroscopy.

In Paper 1, we described the integrated properties of the warm pure-rotational mid-IR H_2 emission, including a comparison with the X-ray distribution, PAH bands, and several fine-structure lines detected with *Spitzer*. In the current paper we explore for the first time the full 2D excitation properties of the warm H_2 to derive physical properties within the gas. We also compare these data with observations taken of other gas phases, including [C II] observations with *Herschel*, IRAM 30 m observations in the CO (1–0) line, and new CO interferometer observations. We present three methods of modeling the H_2 excitation diagrams, including a simple two-temperature fit, a more general power-law technique, and finally multi-component shock modeling. The shock modeling allows us to quantify the mechanical energy dissipation in the gas caused by the intruder galaxy.

The paper is organized as follows. Section 2 describes the observations presented in the paper from *Spitzer* and *Herschel*, and Section 3 summarizes the main observational results. Section 4 describes three methods of modeling the H_2 excitation of the Quintet. Section 5 shows the results of the modeling. Section 6 explores the different estimates of the warm molecular mass and warm mass fraction using the various methods, and Section 7 describes the spatial distribution of the derived properties, including kinetic energy deposition rates and shock properties both across and along

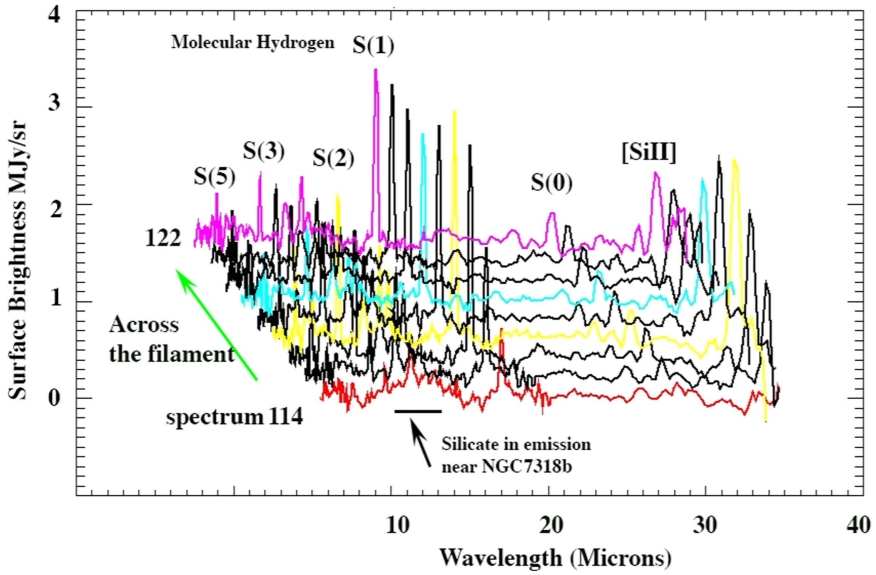

Figure 2. Schematically, we show a short run of nine (of the 212) IRS spectra from the Stephan's Quintet system (positions 114–122 across the main shock; see Figure 1(b)). This demonstrates how the mapping was achieved. Examples of some sample spectra of regions of interest are shown in Appendix A (Figures 15(a) and (b)). The dominant emission is from the rotational lines of warm molecular hydrogen and [Si II] 34.8 μm. The red spectrum (114) is extracted close to the center of NGC 7318b and shows silicates in emission around 10 μm (see also Figure 15(e)). There is no significance to the colors of the spectra other than to make them more identifiable. Note the rapid rise in strength of the 0–0 S(1) and higher rotational lines as one proceeds into the shock, and in this case across the high-excitation region of the so-called "Bridge" region (see text).

the main filament. This includes a strong correlation between the enhanced warm gas fraction and the kinematics of the gas (Section 7.1), as well as a discussion of additional heating from an outflow of an active galactic nucleus (AGN) from NGC 7319 (Section 7.2). Section 8 presents out conclusions, including the relevance of the observations for future far-IR studies of high-z galaxies and protogalaxies. For consistency with Paper 1, we assume a distance to the Quintet of 94 Mpc for $H_0 = 70\,\mathrm{km\,s^{-1}\,Mpc^{-1}}$, based on an assumed group systemic heliocentric velocity of $6600\,\mathrm{km\,s^{-1}}$.

2. The Observations

2.1. Spitzer Observations

Observations of the Quintet filament were made on 2008 January 11 and 2007 December 10 using the short-low (SL with spectral resolution $R = 60$–127; SL2 covering $\lambda = 5.2$–7.7 μm, and submodule SL1 $\lambda = 7.4$–14.5 μm) and long-low modules (LL; $R = 57$–126, with submodules LL2 $\lambda = 14.0$–21.3 μm and LL1, $\lambda = 19.5$–38 μm) of the *Spitzer* IRS (Houck et al. 2004). A full description of the observations, data reductions, and processing was presented in Paper 1. The LL module (repeated separately for the submodules LL1 and LL2) spectrally mapped an area of $\sim 2.8 \times 3.2$ arcmin^2 in 21 steps of 8 arcsec ($0.75 \times$ the slit width) and was designed to cover whole radio/X-ray-emitting filament. Figure 2 illustrates how 1D spectra are built up to accomplish 2D mapping. Similarly, the SL module (covering a slightly smaller area than LL) performed two partially overlapping scans perpendicular to the LL slit, in 2×23 steps of 2.8 arcsec ($0.75 \times$ slit width) for each submodule. After processing through the *Spitzer* Science Center S17 pipelines, all the individual frames were median-combined, calibrated, corrected, and assembled into two-dimensional data cubes using the CUBISM software (Smith et al. 2007a). This resulted in cubes for the SL and LL mapped onto the sky with a pixel scale of 1.85×1.85 arcsec^2 and 5.1×5.1 arcsec^2 respectively.

In order to ensure that we extracted spectra of the molecular hydrogen lines at a common spatial resolution, set by the longest-wavelength 28 μm 0–0 S(0) H_2 line, we convolved, at each wavelength, the individual layers of the SL1, SL2, and LL2 cubes (covering 5–21.3 μm) to the scale of 7 arcsec (the FWHM of the 28 μm H_2 line) using a Gaussian kernel. It was not necessary to smooth the LL1 cube because the only line of interest in this paper is the 28.2 μm line, and so this cube was left in its native form. This procedure has two positive effects. First it ensured that our spectral extractions were not affected by differences in resolution over the 5–28 μm range of the H_2 lines (almost a factor of 5 in spatial resolution from 0–0 S(5) 6.1 μm compared with the 0–0 S(0) 28.2 μm line). Second, the procedure improved the signal-to-noise ratio of the shorter-wavelength data significantly (compared with Paper 1, which did not include smoothing), allowing us to produce high-quality spectra over the full range of observed wavelengths. The resulting data cubes were carefully checked for flux conservation by extracting regions of the convolved cubes over large-scale features, and comparing the extracted fluxes with those obtained from the cube with native resolution. The results were in very close agreement to a few per cent.

In this paper, we present extractions from the spectral maps over those regions that were mapped by both LL and SL modules using PAHFIT (Smith et al. 2007b). Spectra were extracted from the SL1, SL2, LL1, and LL2 cubes, and then stitched together to form the full mid-IR spectra. In general, no scaling was needed in stitching the spectra together. The IRS spectral extractions were performed in CUBISM on the SL and LL cubes using the four corners of 3×3 native SL pixels to define the extraction areas over a continuous grid. This resulted in boxes of area 5.55×5.55 arcsec^2. Figure 1(b) shows the extraction grid of 212 spectra superimposed on a continuum-subtracted Hα *HST* (F665N) image of the Quintet. We only sample regions that are well covered in both the SL and LL cubes, and so we have been conservative about the edges of the

Table 1
Mass of Warm Molecular Hydrogen ($T > 120$ K) and Warm Gas Fraction

Method	$M(H_2)T > 120$ K ($10^8 M_\odot$)	$M(H_2)T > 50$ K ($10^8 M_\odot$)	$M(H_2)_{CO}$[a] ($10^9 M_\odot$)	Warm ($T > 100$ K) Fraction	Warm/Total Ratio Method
Two-temp. (All)	11.2	⋯	5.0	0.22	CO obs.[a]
Power law (All)	7.14	70.9	⋯	0.1	power-law method[b]
Shocks (All)	10.0	27.0	⋯	0.38	shock model[c]
Two-temp. T_1 (only)	11.1	⋯	⋯	⋯	⋯
Two-temp. T_2 (only)	0.12	⋯	⋯	⋯	⋯
Two-temp. (IRAM-R1[e])	0.87[d]	⋯	1.3	0.07	CO obs.[a,e]
Two-temp. (IRAM-R2[e])	0.69[d]	⋯	1.3	0.05	CO obs.[a,e]
Two-temp. (IRAM-R3[e])	0.94[d]	⋯	1.2	0.08	CO obs.[a,e]
$V_{shock} < 20$ km s^{-1}	9.76	26.0	⋯	0.38	shock model[c]
$V_{shock} \geqslant 20$ km s^{-1}	0.40	1.0	⋯	0.4	shock model[c]

Notes.
[a] Using the total H_2 masses derived from Guillard et al. (2012) based on CO (1–0) observations and an assumed $N(H_2)/I_{co}$of 2×10^{20} cm^{-2} (K km s^{-1})$^{-1}$. This would include gas with a potentially lower temperature than 50 K.
[b] Ratio of H_2 with $T > 120$ K to the gas with $T > 50$ K using the power law method. This is the average value for the whole structure and may miss colder gas that the method is not sensitive to. However, as discussed in the text and shown in Figure 10, this ratio can reach values >50% at the peak of the shock.
[c] Total mass is evaluated from the shock model (see text).
[d] Warm H_2 masses from the T_1/T_2 method were evaluated over the IRAM 30 m CO (1–0) beam.
[e] A subset of positions along the shock ridge described in Guillard et al. (2012). These positions are dominated by warm gas with a high temperature and generally lower warm molecular masses than the average for the filament.

mapped area to ensure good coverage at all wavelengths. The results of the extractions are presented in Table 2.

2.2. Herschel Observations

Observations were made using the PACS integral field spectrometer (Poglitsch et al. 2010) on the *Herschel Space Observatory* (Pilbratt et al. 2010) on 2011 December 7 and 8. In Appleton et al. (2013) we presented initial results and gas modeling of the [C II] excitation from these observations, showing that the [C II] line flux is boosted by collisional heating from the warm H_2 gas. In the current paper we extend the analysis to include moment maps of the emission to explore the possible relationship between the [C II] kinematics and the heating of the warm H_2 gas.

The [C II] 157.74 μm observations were made in the first-order gratings using a short "range-scan" mode covering the redshifted wavelength range 160.4–161.74 μm (5050–7600 km s^{-1} heliocentric) with a velocity resolution of 235 km s^{-1}. The PACS integral field unit (IFU) uses an image slicer and reflective optics to project 5 × 5 spatial pixels (each 9.4 × 9.4 arcsec^2 on the sky). Three separate "pointed mode" chop/nod observations were made (3 arcmin chopper throw) with 4 hr of integration time per pointing to cover the main parts of the Quintet filament (see Figure 1(b) of Appleton et al. 2013). Unlike in the analysis presented in that paper, we combine all three pointings into a single data cube using the software *specInterpolate*[11], which was not available at the time of that publication. This software creates a single data cube combined from the three separate pointings, combining all the spaxel positions using an interpolation scheme to ensure the best possible combination of the data given that the filament was not mapped in a fully sampled way. The integrated [C II] map of the Quintet filament is shown in Figure 3; this was created by summing up the spectral flux in the projected cube over the range where emission is detected using the *Herschel* Interactive Processing Environment 12 (HIPE 12).

[11] See *Herschel* PACS User Manual.

3. Observational Results: Mid-IR H_2 Emission and Spectra

In Appleton et al. (2006) and in Paper 1, we presented strong evidence that the molecular hydrogen lines in the Quintet are excited by shocks over most of the filament. The lines are particularly strong along the main filament (see also Figure 1(a)), especially in the center. Except for a few regions on the western side of the mapped area, there are very few places in the entire 212 extraction regions (Figure 1(b)) where no H_2 lines are detected. The current paper concentrates on differences in excitation across the filament, including the region that extends to the east toward the Seyfert galaxy NGC 7319 and westward to include NGC 7318b and 7318a. In Appendix A, we present some examples of the extracted spectra to show the quality of these data, and the generally high signal-to-noise ratio of the molecular hydrogen line detections. We note the detection of silicate emission peaking at approximately 10 μm from spectra taken near the center of both NGC 7318a and NGC 7318b (Figures 15(e) and (h)). Silicate emission is relatively rare, and its detection usually indicates the existence of a warm dust torus surrounding an AGN but seen from above (Li et al. 2008; Hatziminaoglou et al. 2015). We note that both galaxies show weak nuclear X-ray emission (see Figure 2 of O'Sullivan et al. 2009), although NGC 7318a is brighter (with $L(0.3\text{–}3\,\mathrm{keV}) = 9.4 \times 10^{39}$ erg s^{-1} for $D = 94$ Mpc; Trinchieri et al. 2005) and also contains a nuclear radio source (0.95 mJy at 20 cm) (Xu et al. 2003) with a spectral index of 0.62. It is therefore likely that both galaxies contain low-luminosity AGNs.

4. Models of the H_2 Excitation

Molecular hydrogen, being homonuclear, has no allowable dipole transitions, and so only weak quadrupole transitions with $\Delta J = \pm 2$ are allowed. H_2 excitation diagrams are a convenient way of exploring the distribution of level populations in H_2 molecules in galaxies (e.g., Rigopoulou et al. 2002; Roussel et al. 2007). This paper will compare three approaches to fitting the H_2 excitation data derived from the

Table 2
Extracted Line Properties for Each Region Shown in Figure 1(b). Line Fluxes in Units of 10^{-18} W m^{-2}

Region (Figure 1(b))[a]	R.A. (J2000) (deg)	Decl. (J2000) (deg)	0–0 S(0) (unc.) (28.2 μm)[b]	0–0 S(1) (unc.) (17.0 μm)[b]	0–0 S(2) (unc.) (12.3 μm)[b]	0–0 S(3) (unc.) (9.7 μm)[b]	0–0 S(4) (unc.) (8.0 μm)[b]	0–0 S(5) (unc.) (6.9 μm)[b]	0–0 S(6) (unc.) (6.1 μm)[b]	Detected Lines[c]
1	338.99647	33.95042	<0.13[d]	<0.17	<0.25	<0.38	<0.56	<0.39	<0.39	no lines
2	338.99808	33.95118	<0.13	0.25 (0.06)	0.40 (0.07)	<0.38	<0.56	0.79 (0.04)	<0.39	1
3	338.99970	33.95194	<0.13	0.47 (0.06)	0.71 (0.10)	<0.38	<0.56	<0.39	<0.39	12
4	339.00132	33.95270	0.11 (0.04)	1.32 (0.06)	1.01 (0.08)	3.05 (0.13)	<0.56	<0.39	<0.39	123
5	339.00293	33.95346	<0.13	1.21 (0.06)	0.66 (0.16)	2.13 (0.13)	<0.56	<0.39	<0.39	123
6	339.00455	33.95422	<0.13	0.91 (0.06)	<0.25	<0.38	<0.56	0.29 (0.04)	<0.39	1
7	339.00617	33.95498	<0.13	1.06 (0.06)	0.85 (0.40)	1.77 (0.13)	<0.56	2.18 (0.30)	<0.39	135
8	339.00778	33.95574	<0.13	1.11 (0.05)	<0.25	2.14 (0.13)	<0.56	0.86 (0.05)	<0.39	135
9	339.00940	33.95650	<0.13	0.92 (0.05)	0.66 (0.08)	1.75 (0.13)	<0.56	<0.39	<0.39	123
10	339.01102	33.95726	0.22 (0.05)	0.81 (0.04)	<0.25	1.48 (0.14)	<0.56	0.52 (0.04)	<0.39	135
11	338.99555	33.95176	<0.13	0.24 (0.04)	0.24 (0.07)	0.27 (0.11)	<0.56	<0.39	<0.39	no lines
12	338.99717	33.95252	<0.13	0.88 (0.06)	0.52 (0.08)	0.91 (0.12)	<0.56	<0.39	<0.39	123
13	338.99878	33.95328	0.23 (0.04)	2.29 (0.06)	0.80 (0.08)	1.88 (0.13)	<0.56	[1.38 (0.46)]	<0.39	0123[5]
14	339.00040	33.95404	0.26 (0.04)	2.34 (0.06)	1.51 (0.08)	3.37 (0.13)	0.74 (0.16)	2.62 (0.14)	1.67 (0.13)	0123456
15	339.00202	33.95480	0.17 (0.05)	1.67 (0.06)	1.10 (0.08)	1.67 (0.12)	0.49 (0.17)	1.66 (0.14)	1.66 (0.13)	0123456
16	339.00363	33.95556	0.14 (0.04)	1.52 (0.06)	0.75 (0.08)	1.00 (0.12)	<0.56	[1.58 (0.53)]	<0.39	0123[5]
17	339.00525	33.95632	0.29 (0.05)	1.81 (0.06)	1.15 (0.08)	2.34 (0.13)	0.54 (0.17)	1.40 (0.13)	<0.39	012345
18	339.00687	33.95708	0.11 (0.06)	1.20 (0.05)	0.75 (0.08)	1.10 (0.13)	<0.56	<0.39	<0.39	123
19	339.00848	33.95784	<0.13	0.71 (0.05)	0.56 (0.08)	<0.38	<0.56	<0.39	<0.39	12
20	339.01010	33.95860	0.19 (0.05)	0.72 (0.05)	0.45 (0.08)	0.58 (0.11)	<0.56	0.88 (0.14)	1.56 (0.13)	012345
21	338.99463	33.95310	<0.13	0.39 (0.05)	0.60 (0.08)	<0.38	<0.56	<0.39	<0.39	12
22	338.99625	33.95386	<0.13	1.06 (0.06)	0.63 (0.08)	0.51 (0.11)	<0.56	<0.39	<0.39	123
23	338.99787	33.95462	0.20 (0.06)	1.90 (0.06)	1.17 (0.08)	1.53 (0.19)	<0.56	[0.38 (0.13)]	<0.39	0123[5]
24	338.99948	33.95538	0.21 (0.04)	2.37 (0.06)	1.45 (0.08)	2.11 (0.18)	<0.56	1.52 (0.13)	<0.39	01235
25	339.00110	33.95614	0.24 (0.04)	2.21 (0.06)	1.30 (0.08)	1.93 (0.19)	<0.56	1.56 (0.13)	<0.39	01235
26	339.00272	33.95690	0.23 (0.05)	1.54 (0.06)	1.12 (0.08)	1.37 (0.12)	<0.56	1.13 (0.13)	<0.39	01235
27	339.00433	33.95766	<0.13	1.17 (0.05)	<0.25	1.45 (0.18)	<0.56	1.37 (0.13)	<0.39	135
28	339.00595	33.95842	<0.13	1.07 (0.06)	<0.25	0.64 (0.11)	<0.56	0.66 (0.13)	<0.39	135
29	339.00756	33.95919	<0.13	0.76 (0.05)	0.65 (0.08)	<0.38	<0.56	<0.39	<0.39	12
30	339.00918	33.95995	<0.13	0.60 (0.06)	0.75 (0.08)	<0.38	<0.56	<0.39	<0.39	12
31	338.99372	33.95444	0.11 (0.04)	0.24 (0.06)	0.29 (0.07)	<0.38	<0.56	<0.39	<0.39	01
32	338.99533	33.95520	0.10 (0.05)	0.46 (0.05)	0.33 (0.08)	<0.38	<0.56	<0.39	<0.39	12
33	338.99695	33.95596	0.19 (0.05)	1.00 (0.06)	0.51 (0.09)	0.71 (0.11)	<0.56	[0.77 (0.26)]	<0.39	0123[5]
34	338.99856	33.95672	0.09 (0.05)	2.07 (0.06)	1.17 (0.08)	2.01 (0.13)	0.46 (0.17)	1.28 (0.06)	<0.39	01235
35	339.00018	33.95748	0.28 (0.04)	1.95 (0.06)	1.32 (0.08)	2.53 (0.17)	<0.56	1.47 (0.09)	<0.39	01235
36	339.00180	33.95824	0.30 (0.05)	1.37 (0.06)	0.92 (0.08)	1.37 (0.20)	<0.56	0.37 (0.14)	<0.39	01235
37	339.00341	33.95900	0.17 (0.08)	1.08 (0.05)	0.85 (0.10)	0.79 (0.12)	<0.56	[0.60 (0.20)]	<0.39	0123[5]
38	339.00503	33.95976	<0.13	1.00 (0.06)	0.83 (0.08)	0.61 (0.12)	<0.56	<0.39	<0.39	123
39	339.00665	33.96053	<0.13	0.85 (0.07)	0.45 (0.09)	0.54 (0.12)	<0.56	<0.39	<0.39	123
40	339.00826	33.96129	0.12 (0.04)	0.76 (0.05)	0.57 (0.09)	0.52 (0.12)	<0.56	[0.49 (0.16)]	<0.39	0123[5]
41	338.99280	33.95578	<0.13	0.30 (0.05)	0.37 (0.08)	0.71 (0.13)	<0.56	<0.39	<0.39	123
42	338.99441	33.95654	0.15 (0.04)	0.62 (0.06)	0.66 (0.08)	0.88 (0.13)	<0.56	[0.58 (0.19)]	<0.39	0123[5]
43	338.99603	33.95730	0.23 (0.06)	1.64 (0.06)	0.83 (0.08)	1.05 (0.13)	<0.56	[0.56 (0.19)]	<0.39	0123[5]
44	338.99765	33.95806	0.16 (0.05)	2.13 (0.06)	1.22 (0.08)	1.95 (0.13)	<0.56	[0.83 (0.25)]	<0.39	123[5]
45	338.99926	33.95882	0.15 (0.04)	2.11 (0.06)	1.32 (0.08)	2.97 (0.13)	0.61 (0.17)	1.40 (0.15)	<0.39	012345
46	339.00088	33.95958	0.31 (0.04)	1.77 (0.05)	0.78 (0.08)	1.69 (0.13)	<0.56	1.06 (0.18)	<0.39	01235
47	339.00250	33.96034	0.23 (0.05)	1.06 (0.06)	0.69 (0.08)	1.12 (0.13)	<0.56	[0.24 (0.08)]	<0.39	0123[5]

Table 2
(Continued)

Region (Figure 1(b))[a]	R.A. (J2000) (deg)	Decl. (J2000) (deg)	0–0 S(0) (unc.) (28.2 μm)[b]	0–0 S(1) (unc.) (17.0 μm)[b]	0–0 S(2) (unc.) (12.3 μm)[b]	0–0 S(3) (unc.) (9.7 μm)[b]	0–0 S(4) (unc.) (8.0 μm)[b]	0–0 S(5) (unc.) (6.9 μm)[b]	0–0 S(6) (unc.) (6.1 μm)[b]	Detected Lines[c]
48	339.00411	33.96110	0.17 (0.05)	1.03 (0.06)	0.67 (0.08)	1.06 (0.13)	<0.56	[0.26 (0.09)]	<0.39	0123[5]
49	339.00573	33.96187	0.21 (0.04)	1.14 (0.06)	0.45 (0.07)	1.03 (0.13)	<0.56	[0.33 (0.04)]	<0.39	0123[5]
50	339.00735	33.96263	<0.13	0.98 (0.07)	<0.25	0.83 (0.13)	<0.56	<0.39	<0.39	13
51	338.99188	33.95712	<0.13	0.42 (0.06)	<0.25	<0.38	<0.56	<0.39	<0.39	1
52	338.99350	33.95788	0.24 (0.05)	0.92 (0.06)	0.70 (0.08)	0.55 (0.13)	<0.56	1.33 (0.15)	<0.39	01235
53	338.99511	33.95864	0.22(0.04)	1.68 (0.06)	1.35 (0.08)	1.59 (0.13)	0.34 (0.19)	0.81 (0.04)	<0.39	012345
54	338.99673	33.95940	0.35 (0.05)	2.50 (0.06)	2.12 (0.08)	3.24 (0.13)	0.58 (0.19)	1.84 (0.05)	<0.39	012345
55	338.99835	33.96016	0.40 (0.04)	3.48 (0.06)	2.16 (0.08)	4.16 (0.13)	1.09 (0.20)	2.04 (0.06)	0.67 (0.06)	0123456
56	338.99996	33.96092	0.41 (0.04)	2.71 (0.06)	1.74 (0.08)	2.91 (0.13)	<0.60	1.31 (0.05)	0.83 (0.07)	012356
57	339.00158	33.96169	0.26 (0.04)	1.82 (0.06)	0.92 (0.08)	1.01 (0.13)	0.41 (0.16)	[0.72 (0.24)]	<0.39	0123[5]
58	339.00320	33.96245	0.23 (0.04)	1.38 (0.05)	0.68 (0.08)	0.77 (0.13)	<0.56	1.32 (0.15)	<0.39	01235
59	339.00481	33.96321	0.28 (0.04)	1.19 (0.06)	0.66 (0.08)	0.55 (0.12)	<0.56	0.51 (0.06)	<0.39	01235
60	339.00643	33.96397	0.17 (0.05)	1.06 (0.05)	0.53 (0.08)	0.35 (0.12)	<0.56	1.11 (0.30)	0.39 (0.07)	01235
61	338.99096	33.95846	<0.13	0.23 (0.05)	0.46 (0.07)	<0.38	<0.56	<0.39 <0.39	12	
62	338.99258	33.95922	0.17 (0.04)	0.84 (0.05)	0.43 (0.07)	0.42 (0.13)	<0.56	[0.25 (0.08)]	<0.39	0123[5]
63	338.99420	33.95998	0.30 (0.04)	1.61 (0.06)	0.85 (0.08)	0.99 (0.13)	<0.56	0.29 (0.04)	<0.39	01235
64	338.99581	33.96074	0.44 (0.04)	2.52 (0.06)	1.35 (0.08)	1.84 (0.13)	<0.56	0.78 (0.20)	<0.39	01235
65	338.99743	33.96150	0.39 (0.05)	2.89 (0.06)	1.79 (0.08)	3.11 (0.13)	0.77 (0.19)	<0.39	<0.39	01234
66	338.99905	33.96226	0.37 (0.04)	3.32 (0.06)	1.90 (0.08)	3.52 (0.17)	0.98 (0.19)	<0.39	<0.39	01234
67	339.00066	33.96303	0.36 (0.04)	2.57 (0.06)	1.29 (0.08)	1.87 (0.17)	0.56 (0.17)	<0.39	<0.39	01234
68	339.00228	33.96379	0.28 (0.04)	1.70 (0.06)	0.71 (0.08)	1.03 (0.17)	<0.56	[0.45 (0.15)]	<0.39	0123[5]
69	339.00390	33.96455	0.20 (0.05)	1.26 (0.06)	0.57 (0.08)	0.72 (0.12)	<0.56	[0.70 (0.23)]	<0.39	0123[5]
70	339.00551	33.96531	0.20 (0.06)	1.09 (0.06)	0.40 (0.08)	0.68 (0.12)	<0.56	[0.77 (0.26)]	<0.39	0123[5]
71	338.99005	33.95980	<0.13	0.22 (0.06)	<0.25	0.31 (0.11)	<0.56	<0.39	<0.39	13
72	338.99166	33.96056	0.12 (0.04)	0.61 (0.06)	<0.25	0.34 (0.11)	<0.56	<0.39	<0.39	013
73	338.99328	33.96132	0.30 (0.05)	1.22 (0.06)	0.39 (0.07)	0.59 (0.13)	<0.56	[0.11 (0.04)]	<0.39	0123[5]
74	338.99490	33.96208	0.33 (0.05)	1.60 (0.06)	0.75 (0.08)	1.14 (0.17)	<0.56	[0.53 (0.18)]	<0.39	0123[5]
75	338.99651	33.96284	0.37 (0.05)	2.28 (0.06)	0.75 (0.08)	1.41 (0.17)	<0.56	[0.19 (0.06)]	<0.39	0123[5]
76	338.99813	33.96360	0.37 (0.04)	3.47 (0.06)	1.53 (0.08)	2.97 (0.13)	0.84 (0.17)	0.76 (0.08)	<0.39	012345
77	338.99974	33.96437	0.49 (0.04)	3.61 (0.06)	2.33 (0.08)	4.63 (0.13)	0.93 (0.19)	2.49 (0.05)	0.72 (0.15)	0123456
78	339.00136	33.96513	0.42 (0.04)	2.64 (0.06)	1.22 (0.08)	2.80 (0.13)	0.48 (0.19)	1.48 (0.10)	<0.39	012345
79	339.00298	33.96589	0.27 (0.04)	1.69 (0.06)	0.46 (0.08)	1.12 (0.13)	<0.56	[0.65 (0.22)]	<0.39	0123[5]
80	339.00459	33.96665	0.23 (0.04)	1.38 (0.06)	0.45 (0.08)	1.09 (0.13)	<0.56	[0.16 (0.05)]	<0.39	0123[5]
81	339.00621	33.96741	0.20 (0.04)	1.32 (0.06)	0.40 (0.07)	0.85 (0.13)	0.83 (0.19)	<0.39	<0.39	01234
82	339.00783	33.96817	0.16 (0.04)	1.38 (0.05)	0.36 (0.07)	1.23 (0.13)	<0.56	[0.38 (0.13)]	<0.39	0123[5]
83	339.00944	33.96893	0.20 (0.04)	1.41 (0.05)	<0.25	1.18 (0.13)	<0.56	<0.39	<0.39	013
84	338.98913	33.96114	<0.13	<0.17	<0.25	<0.38	<0.56	<0.39	<0.39	no lines
85	338.99074	33.96190	0.06 (0.05)	0.34 (0.06)	<0.25	0.76 (0.13)	<0.56	<0.39	<0.39	013
86	338.99236	33.96266	0.21 (0.05)	0.97 (0.06)	0.30 (0.08)	0.75 (0.13)	<0.56	[0.02 (0.01)]	<0.39	0123[5]
87	338.99398	33.96342	0.33 (0.04)	1.60 (0.06)	0.47 (0.08)	1.17 (0.13)	<0.56	[0.29 (0.08)]	<0.39	0123[5]
88	338.99559	33.96419	0.34 (0.04)	2.03 (0.06)	0.69 (0.08)	1.63 (0.13)	0.47 (0.21)	<0.39	<0.39	01234
89	338.99721	33.96495	0.41 (0.05)	3.17 (0.06)	1.32 (0.08)	3.11 (0.13)	0.62 (0.17)	0.96 (0.09)	<0.39	012345
90	338.99882	33.96571	0.45 (0.06)	4.15 (0.06)	2.06 (0.08)	5.20 (0.13)	1.35 (0.20)	2.59 (0.12)	<0.29	012345
91	339.00044	33.96647	0.53 (0.04)	3.61 (0.06)	1.90 (0.08)	4.81 (0.13)	1.09 (0.24)	2.97 (0.12)	<0.39	012345
92	339.00206	33.96723	0.39 (0.04)	2.53 (0.06)	0.93 (0.08)	2.20 (0.13)	0.83 (0.20)	1.11 (0.12)	<0.39	012345
93	339.00367	33.96799	0.33 (0.04)	1.88 (0.06)	0.55 (0.08)	1.50 (0.13)	0.59 (0.20)	0.27 (0.08)	<0.39	012345
94	339.00529	33.96875	0.36 (0.06)	1.79 (0.06)	0.73 (0.08)	1.52 (0.13)	0.97 (0.20)	<0.39	<0.39	01234

Table 2
(Continued)

Region (Figure 1(b))[a]	R.A. (J2000) (deg)	Decl. (J2000) (deg)	0–0 S(0) (unc.) (28.2 μm)[b]	0–0 S(1) (unc.) (17.0 μm)[b]	0–0 S(2) (unc.) (12.3 μm)[b]	0–0 S(3) (unc.) (9.7 μm)[b]	0–0 S(4) (unc.) (8.0 μm)[b]	0–0 S(5) (unc.) (6.9 μm)[b]	0–0 S(6) (unc.) (6.1 μm)[b]	Detected Lines[c]
95	339.00691	33.96951	0.41 (0.05)	1.85 (0.06)	0.73 (0.08)	1.78 (0.13)	<0.56	[0.08 (0.03)]	<0.39	0123[5]
96	339.00853	33.97027	0.26 (0.04)	1.88 (0.06)	0.76 (0.08)	1.44 (0.13)	<0.56	[0.55 (0.18)]	<0.39	0123[5]
97	338.98821	33.96248	0.20 (0.04)	<0.17	<0.25	<0.63	<0.56	<0.39	<0.39	0
98	338.98982	33.96324	<0.13	0.23 (0.05)	<0.25	<0.68	<0.56	<0.39	<0.39	1
99	338.99144	33.96400	0.09 (0.04)	0.68 (0.06)	<0.25	0.41 (0.13)	<0.56	<0.39	<0.39	013
100	338.99306	33.96476	0.22 (0.04)	1.20 (0.06)	0.19 (0.07)	0.75 (0.13)	<0.56	[0.30 (0.10)]	<0.39	0123[5]
101	338.99468	33.96553	0.27 (0.04)	1.67 (0.06)	0.48 (0.08)	1.28 (0.13)	<0.56	[0.36 (0.12)]	<0.39	0123[5]
102	338.99629	33.96629	0.39 (0.04)	2.94 (0.06)	1.04 (0.08)	2.68 (0.13)	0.48 (0.19)	1.25 (0.12)	<0.39	012345
103	338.99791	33.96705	0.40 (0.05)	4.39 (0.06)	1.95 (0.08)	5.16 (0.13)	1.16 (0.19)	2.47 (0.13)	0.56 (0.13)	0123456
104	338.99953	33.96781	0.54 (0.04)	4.33 (0.06)	2.25 (0.08)	5.94 (0.13)	1.73 (0.25)	3.63 (0.14)	0.73 (0.13)	0123456
105	339.00114	33.96857	0.44 (0.04)	3.33 (0.06)	1.58 (0.08)	3.54 (0.13)	0.88 (0.18)	2.39 (0.14)	0.49 (0.12)	0123456
106	339.00276	33.96933	0.48 (0.06)	2.71 (0.06)	0.74 (0.08)	2.06 (0.13)	0.55 (0.20)	0.72 (0.09)	<0.39	012345
107	339.00437	33.97009	0.44 (0.06)	2.34 (0.06)	0.68 (0.08)	1.85 (0.13)	0.90 (0.21)	<0.39	<0.39	01234
108	339.00599	33.97085	0.50 (0.05)	2.61 (0.06)	0.85 (0.08)	2.22 (0.13)	1.15 (0.20)	[0.69 (0.12)]	<0.39	01234[5]
109	339.00761	33.97161	0.52 (0.06)	3.31 (0.07)	1.17 (0.08)	2.52 (0.13)	0.85 (0.22)	1.19 (0.12)	<0.39	012345
110	338.98729	33.96382	0.20 (0.05)	0.34 (0.07)	<0.25	<0.38	<0.56	<0.39	<0.39	01
111	338.98891	33.96458	<0.13	0.34 (0.07)	<0.25	0.75 (0.13)	<0.56	<0.39	<0.39	13
112	338.99052	33.96534	<0.13	0.38 (0.08)	<0.25	0.68 (0.13)	<0.56	<0.39	<0.39	13
113	338.99214	33.96610	0.15 (0.05)	0.80 (0.05)	<0.25	1.06 (0.13)	<0.56	<0.39	<0.39	013
114	338.99376	33.96687	0.24 (0.04)	1.20 (0.06)	0.24 (0.08)	1.23 (0.13)	<0.56	[0.49 (0.16)]	<0.39	0123[5]
115	338.99537	33.96763	0.34 (0.04)	2.47 (0.06)	0.77 (0.08)	2.46 (0.13)	0.45 (0.19)	1.19 (0.13)	0.39 (0.07)	012345
116	338.99699	33.96839	0.49 (0.05)	4.31 (0.06)	1.93 (0.08)	5.86 (0.13)	1.47 (0.28)	3.34 (0.14)	0.62 (0.14)	0123456
117	338.99861	33.96915	0.49 (0.04)	4.54 (0.06)	2.24 (0.08)	6.43 (0.13)	1.84 (0.19)	3.54 (0.14)	0.71 (0.14)	0123456
118	339.00023	33.96991	0.47 (0.04)	3.71 (0.06)	1.51 (0.08)	4.45 (0.13)	1.37 (0.28)	2.62 (0.12)	<0.39	012345
119	339.00184	33.97067	0.48 (0.06)	3.29 (0.06)	1.05 (0.08)	3.13 (0.13)	1.02 (0.20)	1.71 (0.14)	<0.39	012345
120	339.00346	33.97143	0.54 (0.04)	3.52 (0.06)	1.32 (0.08)	3.46 (0.13)	0.94 (0.23)	1.44 (0.12)	<0.39	012345
121	339.00507	33.97219	0.59 (0.06)	3.61 (0.06)	1.51 (0.08)	3.37 (0.13)	0.86 (0.18)	1.58 (0.14)	0.61 (0.14)	0123456
122	339.00669	33.97295	0.48 (0.04)	3.69 (0.05)	1.47 (0.08)	3.03 (0.13)	0.99 (0.18)	1.66 (0.12)	<0.39	012345
123	338.98637	33.96516	0.22 (0.05)	0.25 (0.04)	<0.25	<0.38	<0.56	<0.39	<0.39	01
124	338.98799	33.96592	0.12 (0.05)	0.33 (0.08)	<0.25	<0.38	<0.56	<0.39	<0.39	01
125	338.98961	33.96669	0.02 (0.05)	0.32 (0.06)	<0.25	0.57 (0.13)	<0.56	<0.39	<0.39	13
126	338.99123	33.96745	<0.13	0.60 (0.05)	<0.25	0.59 (0.13)	<0.56	<0.39	<0.39	13
127	338.99284	33.96821	0.22 (0.05)	0.81 (0.06)	<0.25	0.69 (0.13)	<0.56	<0.39	<0.39	013
128	338.99446	33.96897	0.25 (0.05)	1.77 (0.06)	0.47 (0.08)	1.43 (0.13)	0.68 (0.17)	<0.39	<0.39	01234
129	338.99607	33.96973	0.47 (0.05)	3.51 (0.06)	1.23 (0.08)	3.31 (0.13)	0.83 (0.19)	1.74 (0.13)	0.54 (0.13)	0123456
130	338.99769	33.97049	0.48 (0.05)	4.10 (0.06)	1.80 (0.08)	4.73 (0.13)	1.30 (0.19)	2.29 (0.13)	0.71 (0.13)	0123456
130	338.99769	33.97049	0.48 (0.05)	4.10 (0.06)	1.80 (0.08)	4.73 (0.13)	1.30 (0.19)	2.29 (0.13)	0.71 (0.13)	0123456
131	338.99931	33.97125	0.50 (0.04)	3.65 (0.06)	1.46 (0.08)	3.81 (0.13)	1.08 (0.18)	1.90 (0.14)	0.53 (0.14)	0123456
132	339.00092	33.97201	0.56 (0.04)	3.75 (0.06)	1.38 (0.08)	3.70 (0.13)	0.80 (0.18)	1.87 (0.14)	<0.39	012345
133	339.00254	33.97277	0.53 (0.04)	3.58 (0.06)	1.58 (0.08)	3.76 (0.13)	1.25 (0.18)	1.46 (0.13)	0.90 (0.13)	0123456
134	339.00416	33.97354	0.62 (0.05)	3.59 (0.06)	1.66 (0.08)	3.58 (0.13)	1.51 (0.18)	1.46 (0.13)	1.26 (0.13)	0123456
135	339.00578	33.97430	0.44 (0.04)	3.56 (0.05)	0.98 (0.08)	2.03 (0.17)	0.83 (0.19)	[1.19 (0.14)]	<0.39	01234[5]
136	338.98869	33.96803	0.13 (0.05)	0.31 (0.06)	<0.25	<0.38	<0.56	<0.39	<0.39	01
137	338.99031	33.96879	0.14 (0.05)	0.40 (0.06)	<0.25	<0.38	<0.56	<0.39	<0.39	01
138	338.99192	33.96955	0.13 (0.06)	0.66 (0.05)	<0.25	<0.38	<0.56	<0.39	<0.39	01
139	338.99354	33.97031	0.23 (0.05)	0.98 (0.06)	0.52 (0.08)	0.61 (0.13)	<0.56	[0.51 (0.17)]	<0.39	0123[5]
140	338.99516	33.97107	0.26 (0.06)	1.90 (0.06)	0.55 (0.09)	1.49 (0.13)	<0.56	[0.50 (0.17)]	<0.39	0123[5]

Table 2
(Continued)

Region (Figure 1(b))[a]	R.A. (J2000) (deg)	Decl. (J2000) (deg)	0–0 S(0) (unc.) (28.2 μm)[b]	0–0 S(1) (unc.) (17.0 μm)[b]	0–0 S(2) (unc.) (12.3 μm)[b]	0–0 S(3) (unc.) (9.7 μm)[b]	0–0 S(4) (unc.) (8.0 μm)[b]	0–0 S(5) (unc.) (6.9 μm)[b]	0–0 S(6) (unc.) (6.1 μm)[b]	Detected Lines[c]
141	338.99677	33.97183	0.38 (0.04)	3.10 (0.06)	1.10 (0.08)	3.05 (0.13)	<0.56	1.19 (0.13)	<0.39	01235
142	338.99839	33.97259	0.64 (0.06)	4.39 (0.06)	1.94 (0.08)	4.74 (0.13)	0.93 (0.17)	2.53 (0.06)	0.63 (0.06)	0123456
143	339.00001	33.97335	0.66 (0.04)	4.04 (0.06)	1.82 (0.08)	4.71 (0.13)	1.16 (0.21)	2.45 (0.05)	0.83 (0.06)	0123456
144	339.00162	33.97411	0.50 (0.04)	3.33 (0.06)	0.85 (0.08)	2.46 (0.13)	0.85 (0.17)	0.92 (0.13)	<0.39	012345
145	339.00324	33.97488	0.51 (0.05)	3.15 (0.06)	0.67 (0.09)	1.96 (0.13)	1.09 (0.17)	<0.39	<0.39	01234
146	339.00486	33.97564	0.46 (0.06)	1.98 (0.06)	0.51 (0.08)	1.27 (0.13)	0.67 (0.17)	1.43 (0.13)	<0.39	012345
147	338.98777	33.96937	0.20 (0.05)	0.41 (0.06)	0.39 (0.09)	<0.38	<0.56	<0.39	<0.39	012
148	338.98939	33.97013	<0.13	0.37 (0.06)	<0.25	<0.38	<0.56	<0.39	<0.39	1
149	338.99100	33.97089	<0.13	0.48 (0.05)	0.36 (0.08)	<0.38	<0.56	<0.39	<0.39	12
150	338.99262	33.97165	0.16 (0.04)	0.67 (0.05)	0.57 (0.08)	0.36 (0.13)	<0.56	[0.85 (0.28)]	<0.39	0123[5]
151	338.99424	33.97241	0.23 (0.06)	1.29 (0.06)	0.56 (0.08)	0.85 (0.13)	<0.56	[0.61 (0.20)]	<0.39	0123[5]
152	338.99585	33.97317	0.36 (0.04)	2.98 (0.06)	0.94 (0.08)	2.21 (0.15)	<0.56	[0.86 (0.29)]	<0.39	0123[5]
153	338.99747	33.97393	0.63 (0.06)	4.65 (0.06)	2.29 (0.08)	4.70 (0.15)	1.15 (0.17)	2.64 (0.14)	<0.39	012345
154	338.99909	33.97469	0.69 (0.04)	4.54 (0.06)	2.00 (0.08)	4.17 (0.16)	0.97 (0.20)	2.92 (0.14)	0.82 (0.14)	0123456
155	339.00070	33.97545	0.54 (0.04)	3.30 (0.06)	1.10 (0.08)	1.88 (0.18)	0.49 (0.17)	<0.39	<0.39	01234
156	339.00232	33.97622	0.41 (0.04)	1.99 (0.06)	0.64 (0.08)	0.99 (0.12)	0.71 (0.16)	<0.39	<0.39	01234
157	339.00394	33.97698	0.36 (0.06)	1.45 (0.06)	0.55 (0.08)	0.71 (0.13)	0.36 (0.16)	<0.39	<0.39	01234
158	338.98685	33.97071	0.14 (0.04)	0.27 (0.06)	0.18 (0.09)	0.34 (0.13)	<0.56	[0.54 (0.18)]	<0.39	0123[5]
159	338.98847	33.97147	<0.13	0.28 (0.06)	<0.25	<0.38	<0.56	<0.39	<0.39	1
160	338.99009	33.97223	<0.13	0.48 (0.06)	<0.25	<0.38	<0.56	<0.39	<0.39	1
161	338.99170	33.97299	<0.13	0.57 (0.06)	0.28 (0.08)	<0.38	<0.56	<0.39	<0.39	12
162	338.99332	33.97375	0.25 (0.04)	1.04 (0.05)	0.26 (0.07)	0.76 (0.12)	<0.56	[0.38 (0.13)]	<0.39	0123[5]
163	338.99494	33.97451	0.31 (0.04)	2.03 (0.06)	0.59 (0.08)	0.95 (0.12)	<0.56	[0.92 (0.31)]	<0.39	0123[5]
164	338.99655	33.97527	0.55 (0.05)	3.80 (0.06)	1.43 (0.08)	2.84 (0.12)	0.74 (0.20)	1.65 (0.13)	<0.39	012345
165	338.99817	33.97604	0.57 (0.04)	4.26 (0.06)	1.82 (0.08)	3.57 (0.13)	1.24 (0.20)	2.42 (0.14)	<0.39	012345
166	338.99979	33.97680	0.55 (0.04)	2.97 (0.06)	1.38 (0.08)	2.53 (0.13)	0.48 (0.17)	1.72 (0.14)	<0.39	012345
167	339.00140	33.97756	0.40 (0.04)	1.90 (0.06)	0.77 (0.08)	1.12 (0.12)	0.45 (0.20)	1.03 (0.05)	<0.39	012345
168	339.00302	33.97832	0.33 (0.04)	1.50 (0.06)	0.55 (0.08)	0.88 (0.17)	0.42 (0.17)	<0.39	<0.39	01234
169	338.98594	33.97205	0.16 (0.04)	0.58 (0.05)	0.17 (0.07)	<0.38	<0.56	<0.39	<0.39	012
170	338.98755	33.97281	0.26 (0.05)	0.50 (0.06)	0.41 (0.07)	<0.38	<0.56	<0.39	<0.39	012
171	338.98917	33.97357	0.18 (0.04)	0.54 (0.06)	0.31 (0.08)	0.50 (0.13)	<0.56	[0.90 (0.30)]	<0.39	0123[5]
172	338.99079	33.97433	0.13 (0.04)	0.62 (0.06)	0.24 (0.07)	0.40 (0.13)	<0.56	[0.84 (0.28)]	<0.39	0123[5]
173	338.99240	33.97509	0.27 (0.04)	1.10 (0.05)	0.16 (0.07)	0.59 (0.15)	<0.56	[0.52 (0.17)]	<0.39	0123[5]
174	338.99402	33.97585	0.37 (0.04)	1.85 (0.06)	0.41 (0.08)	0.93 (0.13)	<0.56	0.48 (0.13)	<0.39	01235
175	338.99564	33.97661	0.64 (0.06)	2.82 (0.06)	1.04 (0.08)	1.81 (0.13)	0.34 (0.18)	0.98 (0.13)	<0.39	012345
176	338.99725	33.97738	0.72 (0.06)	3.23 (0.06)	1.52 (0.08)	2.58 (0.13)	1.51 (0.18)	1.68 (0.14)	<0.39	012345
177	338.99887	33.97814	0.60 (0.04)	2.95 (0.06)	1.16 (0.09)	2.45 (0.13)	0.61 (0.21)	1.43 (0.14)	<0.39	012345
178	339.00049	33.97890	0.49 (0.04)	2.32 (0.06)	0.70 (0.10)	1.60 (0.14)	0.63 (0.20)	1.66 (0.14)	<0.39	012345
179	339.00210	33.97966	0.44 (0.04)	2.07 (0.06)	0.62 (0.12)	0.62 (0.13)	<0.56	1.51 (0.14)	<0.39	01235
180	338.98502	33.97339	0.24 (0.05)	0.60 (0.05)	0.40 (0.08)	<0.38	<0.56	<0.39	<0.39	012
181	338.98663	33.97415	0.26 (0.04)	0.67 (0.06)	0.47 (0.07)	<0.38	<0.56	<0.39	<0.39	012
182	338.98825	33.97491	0.31 (0.04)	1.14 (0.06)	0.61 (0.10)	0.76 (0.13)	<0.56	0.64 (0.14)	<0.39	01235
183	338.98987	33.97567	0.42 (0.04)	1.68 (0.06)	0.64 (0.08)	1.06 (0.13)	<0.56	0.63 (0.10)	<0.39	01235
184	338.99148	33.97643	0.48 (0.04)	1.86 (0.06)	0.57 (0.08)	0.77 (0.13)	<0.56	[1.17 (0.39)]	<0.39	0123[5]
185	338.99310	33.97719	0.74 (0.06)	2.11 (0.06)	0.57 (0.08)	0.93 (0.13)	<0.56	0.77 (0.10)	<0.39	01235
186	338.99472	33.97795	0.61 (0.04)	2.48 (0.06)	0.81 (0.08)	1.35 (0.13)	0.42 (0.17)	0.98 (0.10)	<0.39	012345
187	338.99633	33.97872	0.83 (0.04)	3.37 (0.06)	1.27 (0.08)	2.08 (0.13)	0.40 (0.18)	1.55 (0.13)	0.50 (0.15)	0123456

Table 2
(Continued)

Region (Figure 1(b))[a]	R.A. (J2000) (deg)	Decl. (J2000) (deg)	0–0 S(0) (unc.) (28.2 μm)[b]	0–0 S(1) (unc.) (17.0 μm)[b]	0–0 S(2) (unc.) (12.3 μm)[b]	0–0 S(3) (unc.) (9.7 μm)[b]	0–0 S(4) (unc.) (8.0 μm)[b]	0–0 S(5) (unc.) (6.9 μm)[b]	0–0 S(6) (unc.) (6.1 μm)[b]	Detected Lines[c]
188	338.99795	33.97948	0.75 (0.04)	3.55 (0.06)	1.05 (0.08)	2.06 (0.13)	0.57 (0.18)	<0.39	<0.39	01234
189	338.99957	33.98024	0.80 (0.06)	2.92 (0.06)	0.87 (0.08)	1.98 (0.13)	0.63 (0.21)	1.49 (0.13)	<0.39	012345
190	339.00119	33.98100	0.58 (0.06)	2.40 (0.06)	0.89 (0.08)	1.19 (0.18)	<0.56	1.38 (0.13)	<0.39	01235
191	338.98410	33.97473	0.18 (0.04)	0.52 (0.06)	0.59 (0.08)	0.31 (0.15)	<0.56	[0.59 (0.20)]	<0.39	0123[5]
192	338.98572	33.97549	0.29 (0.04)	0.89 (0.06)	0.77 (0.08)	0.71 (0.13)	<0.56	[0.86 (0.29)]	<0.39	0123[5]
193	338.98733	33.97625	0.39 (0.06)	1.64 (0.05)	1.01 (0.08)	0.90 (0.13)	<0.56	<0.39	<0.39	01235
194	338.98895	33.97701	0.62 (0.05)	2.21 (0.06)	1.42 (0.08)	1.78 (0.13)	<0.56	1.42 (0.13)	<0.39	01235
195	338.99057	33.97777	0.65 (0.05)	2.63 (0.06)	1.32 (0.08)	1.79 (0.13)	0.57 (0.18)	2.08 (0.13)	<0.39	01235
196	338.99218	33.97854	0.81 (0.04)	2.84 (0.07)	1.17 (0.08)	1.74 (0.13)	<0.56	1.65 (0.13)	<0.39	01235
197	338.99380	33.97930	1.00 (0.04)	3.73 (0.06)	1.38 (0.08)	2.10 (0.13)	0.33 (0.17)	0.71 (0.13)	0.50 (0.13)	0123456
198	338.99542	33.98006	1.24 (0.04)	4.70 (0.06)	1.87 (0.08)	3.04 (0.13)	0.57 (0.17)	1.63 (0.13)	<0.39	012345
199	338.99703	33.98082	0.93 (0.06)	4.12 (0.06)	1.77 (0.08)	3.16 (0.13)	0.50 (0.17)	1.56 (0.13)	<0.39	012345
200	338.99865	33.98158	0.69 (0.06)	3.13 (0.06)	1.43 (0.08)	2.39 (0.13)	<0.56	1.23 (0.13)	<0.39	01235
201	339.00027	33.98234	0.53 (0.06)	2.48 (0.06)	1.20 (0.08)	1.44 (0.17)	<0.56	[0.95 (0.32)]	<0.39	0123[5]
202	338.98318	33.97607	0.11 (0.04)	0.49 (0.06)	0.66 (0.08)	0.57 (0.13)	<0.56	<0.39	<0.39	123
203	338.98480	33.97683	0.30 (0.05)	1.07 (0.06)	0.43 (0.08)	1.21 (0.13)	<0.56	[1.00 (0.33)]	<0.39	0123[5]
204	338.98642	33.97759	0.47 (0.06)	1.60 (0.06)	0.53 (0.08)	1.02 (0.13)	<0.56	[0.68 (0.23)]	<0.39	0123[5]
205	338.98803	33.97835	0.56 (0.05)	2.34 (0.06)	0.96 (0.08)	1.90 (0.13)	<0.56	[1.04 (0.35)]	<0.39	0123[5]
206	338.98965	33.97911	0.67 (0.06)	2.94 (0.06)	1.29 (0.08)	2.21 (0.13)	1.47 (0.19)	<0.39	<0.39	01234
207	338.99127	33.97988	0.96 (0.04)	4.56 (0.06)	1.68 (0.08)	2.98 (0.13)	1.93 (0.19)	1.07 (0.13)	<0.39	012345
208	338.99288	33.98064	1.30 (0.06)	4.60 (0.06)	1.61 (0.08)	3.29 (0.13)	2.08 (0.22)	1.63 (0.13)	<0.39	012345
209	338.99450	33.98140	1.22 (0.06)	4.93 (0.06)	1.79 (0.08)	3.79 (0.13)	1.57 (0.21)	2.26 (0.13)	<0.39	012345
210	338.99612	33.98216	1.19 (0.04)	4.91 (0.06)	1.85 (0.08)	3.52 (0.13)	<0.56	[2.27 (0.76)]	<0.39	0123[5]
211	338.99773	33.98292	0.70 (0.06)	3.50 (0.06)	1.38 (0.08)	1.95 (0.13)	<0.56	[1.50 (0.50)]	<0.39	0123[5]
212	338.99935	33.98368	0.43 (0.04)	1.89 (0.06)	0.96 (0.08)	1.33 (0.13)	<0.56	[0.97 (0.32)]	<0.39	0123[5]

Notes.
[a] Extracted over regions defined in Figure 1(b) and of area 5.1 × 5.1 arcsec^2.
[b] 1σ uncertainties derived from PAHFIT.
[c] Lines detected 0 = 0–0 S(0), 1 = 0–0 S(1) etc. Square brackets denote "marginal detection" used to help constrain two-temperature fits in a minority of cases. Those fluxes are also denoted by square brackets.
[d] 3σ upper limits.

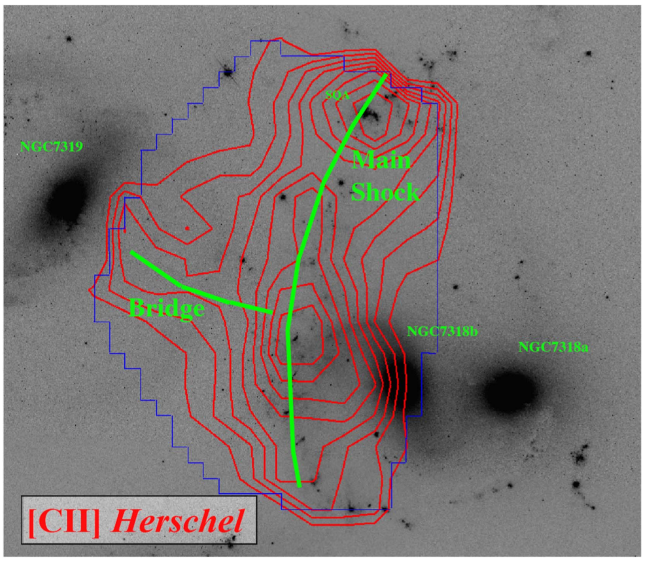

Figure 3. *Herschel* integrated map (contours) of the [C II] emission in Stephan's Quintet obtained with the PACS spectrometer. The map is a combination of three overlapping pointings of the IFU into one single image. The blue outline marks the edge of the mapping area (contours extend slightly beyond these boundaries because of contour interpolation). The [C II] emission extends along the main north–south filament (including the extragalactic star-forming region known as the SQ-A), as well defining part of the bridge seen the *Spitzer* data, which extends toward the nucleus of the galaxy NGC 7319. Contour are 5, 7.5, 10, 12.5, 15, 17.5, 19, 21, and 25 in units of 1.2×10^{-19} W m^{-2} pix^{-1}.

two-dimensional IRS mapping of the Quintet. The first is a traditional method of fitting single- or multiple-temperature components to the excitation diagrams. This method is commonly used in H_2 studies of galaxies. A second method is an extension of this idea, assuming that most galaxy excitation diagrams can be modeled as a single power-law distribution of temperatures. Both of these approaches assume that the gas is in thermal equilibrium. A third method assumes that the excitation of the warm H_2 is caused primarily by C- or J-shocks (or a combination of the two) following the methodology of Lesaffre et al. (2013). Arguments strongly in favor of shock excitation over other heating sources have been made in previous works (see particularly Appleton et al. 2006, 2013; Guillard et al. 2009; Cluver et al. 2010; Lesaffre et al. 2013). In this case, local thermodynamic equilibrium (LTE) conditions are not assumed in the derived properties of the warm gas.

4.1. Fitting One- or Two-temperature Models to the Excitation Diagrams

The transitions we are considering are to the lowest ground-state pure-rotational states of H_2, e.g., 0–0 S(0)$\lambda = 28.22\ \mu$m (corresponding to $J = 2$–0), 0–0 S(1)$\lambda = 17.04\ \mu$m (corresponding to $J = 3$–1), and 0–0 S(2) to 0–0 S(6)$\lambda = 6.11\ \mu$m. These transitions radiate in the wavelength range detectable with the *Spitzer* IRS[12] Assuming that the mid-IR lines are optically thin, the column density of the upper level of each pure-rotational transition is measured observationally from the spectral line flux F of a given transition according to $N_u = 4\pi F/(h\nu A\Omega)$, where h is Planck's constant, ν is the frequency of the transition, A is the Einstein coefficient for the transition, and Ω is the solid angle of the observed region. In LTE, the column density of the upper level is related to both the excitation temperature T and the total column density $N_{\rm tot}$ via $N_u/g_u = N_{\rm tot}\exp(-E_u/kT)/Z(T)$, where E_u is the energy of the upper level transition, k is Boltzmann's constant, and $Z(T)$ is the partition function.[13] $g_u = (2S+1)(2J+1)$ is the statistical weight of the transition, and E_u is the energy of a particular upper level transition. For g_u, S is the spin number for a given J transition, where $S = 0$ for even J (called para-hydrogen) and $S = 1$ for odd J (ortho-hydrogen). The H_2 excitation diagram is usually presented as a plot of $\log_e(N_u/g_u)$ versus E_u/k, and is convenient because, for a single excitation temperature, the slope of a line fit to these points would be proportional to T^{-1}.

It is generally assumed that, for the lower pure-rotational H_2 transitions, the ortho- and para-H_2 species should be in collisional equilibrium. As shown by Roussel et al. (2007) for H_2 densities $\gtrsim 10^3$ cm^{-3}, most of the lower rotational transitions should be thermalized, and temperatures derived from fits to the ortho- and para-H_2 transitions should be consistent. Burton et al. (1992) showed that in collisional equilibrium, the ortho-to-para ratio (OPR) increases from about unity at $T = 75$ K to a constant value of 3 at $T > 250$ K. Since most of the temperatures we derive from the excitation fitting are in the range $120 < T < 600$ K, the equilibrium values of OPR assumed are between 1.8 and 3. After normalizing for this factor, significant deviations from LTE would appear as an offset between the odd and even H_2 transitions when plotted on an excitation diagram. We see no evidence for deviations from equilibrium in any of our observations (see also Paper 1).

A single-temperature fit is usually not found to be realistic, since the excitation diagrams are rarely consistent with a straight line and are often curved. In most cases a two-temperature fit offers a reasonable solution. In the literature, this is a very common approach because it provides a first approximation to the temperatures, column densities, and total H_2 masses derived from the observations. We will generalize this approach later in the paper to consider a power-law distribution of temperatures. However, we will begin with a simple one- or two-temperature fit to these data, under the assumption of LTE. This approach yields interesting insight into the excitation of the gas across this large-scale filament.

Single-temperature solutions were found where there were not enough points to justify a two-temperature fit (22% of these data; see Table 3 for details), and two-temperature solutions were obtained for the other cases. The process for fitting a two-temperature LTE model to these data is iterative. First we create an initial excitation diagram with the line fluxes (from Table 2). Initially we assume an OPR of 3 to obtain a first approximation to the temperature, minimizing the chi-squared deviations for a two-temperature model. Once the chi-squared values are minimized, we assume those temperatures as a first guess and adjust the OPR appropriate for LTE from Burton et al. (1992) and re-run. This process is repeated for several iterations until best-fit values for the temperature and column density are determined. Figure 4 shows an examples of such a fit for a point near the center of the filament. The results of the fitting for the extraction regions of Figure 1(b) are presented in Table 3. For the minority of observations where the 0–0 S(0) line was not detected, we provide a range of possible temperatures for the gas. We use both a regular fit to the

[12] For the Quintet, transitions shortward of the 0–0 S(6) line were not detected.

[13] We assume $Z(T) = 0.0247T/(1-\exp(-6000\ {\rm K}/T))$.

Table 3
Results from One- or Two-temperature Fitting of the Warm Molecular Hydrogen

Region[a]	T_1 (unc.)[b] (K)	OPR_1	$N(H_2)_1$ (10^{19} cm^{-2})	$\Sigma(H_2)_1$ (unc.)[b] (10^6 $M_\odot$ kpc^{-2})	T_2 (unc.)[b] (K)	OPR_2	$N(H_2)_2$ (10^{17} cm^{-2})	$\Sigma(H_2)_2$ (unc.)[b] ($10^4 M_\odot$ kpc^{-2})	Lines (0–0 S(...))
3	154–805[c]	2.5–3.0[c]	2.5–0.05[c]	0.4–0.08[c]	⋯	⋯	⋯	⋯	12
4	223–425[c]	2.9–3.0[c]	1.13–0.24[c]	0.18–0.04[c]	⋯	⋯	⋯	⋯	123
5	205–361[c]	2.9–3.0[c]	1.44–0.28[c]	0.23–0.04[c]	⋯	⋯	⋯	⋯	123
8	199–439[c]	2.8–3.0[c]	1.51–0.18[c]	0.24–0.03[c]	⋯	⋯	⋯	⋯	135
9	187–426[c]	2.79–3.0[c]	1.69–0.2[c]	0.27–0.03[c]	⋯	⋯	⋯	⋯	123
10	154–398[c]	2.54–2.99[c]	4.3–0.2[c]	0.69–0.3[c]	⋯	⋯	⋯	⋯	135
12	184–372[c]	2.77–3.0[c]	1.74–0.2[c]	0.28–0.03[c]	⋯	⋯	⋯	⋯	123
13	227 (34)	2.94	1.67	0.27 (0.16)	732 (73)	3.0	2.50	0.39 (0.08)	0123[5][d]
14	215 (32)	2.89	2.28	0.37 (0.22)	906 (91)	3.0	3.20	0.51 (0.10)	0123456
15	276 (41)	2.98	0.86	0.14 (0.08)	1500 (150)	3.0	0.50	0.01 (0.00)	0123456
16	217 (33)	2.90	1.30	0.23 (0.14)	640 (64)	3.0	2.60	0.42 (0.08)	0123[5][d]
17	179 (27)	2.75	2.72	0.40 (0.24)	620 (62)	3.0	6.70	1.07 (0.21)	012345
18	217–382[c]	2.9–3.0[c]	1.16–0.25[c]	0.18–0.04[c]	⋯	⋯	⋯	⋯	123
19	173–455[c]	2.7–3.0[c]	1.95–0.11[c]	0.31–0.02[c]	⋯	⋯	⋯	⋯	12
20	208 (31)	2.88	0.88	0.83 (0.33)	817 (82)	3.0	6.30	1.01 (0.20)	012345
21	147–825[c]	2.45–3.0[c]	2.81–0.04[c]	0.45–0.06[c]	⋯	⋯	⋯	⋯	12
22	196–378	2.8–3.0[c]	1.55–0.22[c]	0.25–0.04[c]	⋯	⋯	⋯	⋯	123
23	138 (21)	2.30	3.86	0.62 (0.25)	407 (41)	3.0	29.00	4.66 (0.93)	0123[5][d]
24	346 (52)	3.00	0.60	0.10 (0.06)	1500 (150)	3.0	0.30	0.04 (0.02)	01235
25	334 (50)	2.99	0.61	0.10 (0.06)	1461 (146)	3.0	0.30	0.05 (0.03)	01235
26	340 (51)	3.00	0.43	0.10 (0.06)	1500 (150)	3.0	0.20	0.03 (0.01)	01235
27	203–476[c]	2.9–3.0[c]	1.47–0.11[c]	0.23–0.02[c]	⋯	⋯	⋯	⋯	135
28	197–326[c]	2.83–2.99[c]	1.55–0.3[c]	0.25–0.05[c]	⋯	⋯	⋯	⋯	135
29	175–476[c]	2.73–3.0[c]	1.89–0.01[c]	0.46–0.02[c]	⋯	⋯	⋯	⋯	12
30	165–655[c]	2.6–3.0[c]	2.17–0.07[c]	0.35–0.01[c]	⋯	⋯	⋯	⋯	12
31	135 (20)	2.1	3.1	0.5	⋯	⋯	⋯	⋯	01
32	163–348	2.6–3.0[c]	1.73–0.13[c]	0.28–0.02[c]	⋯	⋯	⋯	⋯	12
33	193 (29)	2.80	1.46	0.23 (0.14)	701 (70)	3.0	1.50	0.24 (0.05)	0123[5][d]
34	348 (52)	3.00	0.50	0.10 (0.06)	1500 (150)	3.0	0.20	0.04 (0.02)	01235
35	177 (27)	2.73	2.85	0.50 (0.20)	607 (61)	3.0	8.90	1.43 (0.29)	01235
36	118 (18)	2.00	11.10	1.80 (0.36)	439 (44)	3.0	18.00	2.89 (0.58)	01235
37	143 (22)	2.40	3.46	0.56 (0.22)	464 (46)	3.0	10.80	1.73 (0.35)	0123[5][d]
38	192–469[c]	2.8–3.0[c]	1.61–0.15[c]	0.26–0.03[c]	⋯	⋯	⋯	⋯	123
39	177–354[c]	2.7–3.0[c]	1.86–0.2[c]	0.3–0.03[c]	⋯	⋯	⋯	⋯	123
40	153 (23)	2.50	2.10	0.34 (0.20)	525 (53)	3.0	5.10	0.82 (0.16)	0123[5][d]
41	137.9–667[c]	2.3–3.0[c]	3.32–0.03[c]	0.53–0.005	⋯	⋯	⋯	⋯	123
42	100 (20)	1.58	9.95	1.60 (0.32)	485 (49)	3.0	8.40	1.40 (0.28)	0123[5][d] [d]
43	164 (25)	2.60	3.70	0.59 (0.24)	473 (47)	3.0	10.00	1.61 (0.32)	0123[5][d]
44	349 (52)	3.00	0.52	0.10 (0.06)	1500 (150)	3.0	0.10	0.02 (0.01)	1235
45	363 (54)	3.00	0.46	0.10 (0.06)	947 (95)	3.0	0.90	0.14 (0.03)	012345
46	174 (26)	2.71	3.86	0.60 (0.24)	636 (64)	3.0	4.20	0.67 (0.13)	01235
47	126 (20)	2.10	7.00	1.10 (0.22)	436 (44)	3.0	12.60	2.00 (0.40)	0123[5][d]
48	141 (21)	2.40	3.40	0.55 (0.22)	446 (45)	3.0	11.00	1.80 (0.36)	0123[5][d]
49	164 (25)	2.63	3.18	0.50 (0.20)	559 (56)	3.0	3.80	0.61 (0.12)	01235
50	191–352[c]	1.6–3.0[c]	1.62–0.24[c]	0.26–0.04[c]	⋯	⋯	⋯	⋯	13
52	142 (21)	2.39	5.20	0.80 (0.32)	671 (67)	3.0	4.20	0.68 (0.14)	01235
53	359 (54)	3.00	0.42	0.10 (0.06)	1500 (150)	3.0	0.10	0.02 (0.01)	012345
54	375 (56)	3.00	0.58	0.10 (0.06)	1500 (150)	3.0	0.30	0.05 (0.03)	012345
55	357 (54)	3.00	0.83	0.10 (0.06)	1247 (125)	3.0	0.50	0.09 (0.05)	0123456
56	347 (52)	3.00	0.72	0.10 (0.06)	1500 (150)	3.0	0.20	0.04 (0.02)	012356
57	165 (25)	1.20	4.00	0.63 (0.25)	470 (47)	3.0	11.20	1.80 (0.36)	0123[5][d]
58	243 (36)	2.95	0.90	0.10 (0.06)	106 (104)	3.0	0.60	0.10 (0.02)	01235
59	147 (22)	2.46	5.57	0.90 (0.36)	560 (56)	3.0	5.30	0.86 (0.17)	01235
60	266 (40)	2.97	0.53	0.10 (0.06)	1469 (147)	3.0	0.20	0.03 (0.01)	01235
61	131–1178[c]	2.2–3.0[c]	3.8–0.02[c]	0.6–0.004[c]	⋯	⋯	⋯	⋯	12
62	150 (23)	2.50	3.15	0.51 (0.20)	506 (51)	3.0	4.70	0.76 (0.15)	0123[5][d]
63	152 (23)	2.51	5.34	0.90 (0.36)	470 (47)	3.0	11.10	1.79 (0.36)	01235
64	147 (22)	2.46	8.31	1.30 (0.26)	436 (44)	3.0	23.20	3.73 (0.75)	01235
65	100 (20)	1.59	22.20	3.60 (0.72)	383 (38)	3.0	56.90	9.15 (1.83)	01234
66	140 (21)	2.36	7.09	1.10 (0.22)	408 (41)	3.0	48.60	7.82 (1.56)	01234
67	133 (20)	2.26	8.24	1.30 (0.26)	379 (38)	3.0	42.40	6.81 (1.36)	01234
68	162 (24)	2.60	5.00	0.73 (0.29)	497 (50)	3.0	7.90	1.27 (0.25)	0123[5][d]
69	171 (26)	2.70	3.00	0.48 (0.29)	581 (58)	3.0	3.30	0.53 (0.11)	0123[5][d]

Table 3
(Continued)

Region[a]	T_1 (unc.)[b] (K)	OPR_1	$N(H_2)_1$ (10^{19} cm^{-2})	$\Sigma(H_2)_1$ (unc.)[b] (10^6 $M_\odot$ kpc^{-2})	T_2 (unc.)[b] (K)	OPR_2	$N(H_2)_2$ (10^{17} cm^{-2})	$\Sigma(H_2)_2$ (unc.)[b] ($10^4 M_\odot$ kpc^{-2})	Lines (0–0 S(...))
70	185 (28)	2.80	1.80	0.29 (0.17)	758 (76)	3.0	1.10	0.18 (0.04)	0123[5][d]
71	129–404[c]	2.2–3.0[c]	4.0–0.04[c]	0.6–0.006[c]	⋯	⋯	⋯	⋯	13
72	180 (18)	2.75	1.35	0.2 (0.03)	⋯	⋯	⋯	⋯	013
73	147 (22)	2.50	6.00	1.00 (0.20)	453 (45)	3.0	5.80	0.93 (0.19)	0123[5][d]
74	148 (22)	2.50	6.70	1.50 (0.30)	490 (49)	3.0	9.60	1.50 (0.30)	0123[5][d]
75	162 (24)	2.62	5.90	0.90 (0.36)	441 (44)	3.0	13.20	2.13 (0.43)	0123[5][d]
76	212 (32)	2.89	2.76	0.40 (0.24)	533 (53)	3.0	11.70	1.88 (0.38)	012345
77	277 (42)	2.98	1.39	0.20 (0.12)	715 (72)	3.0	6.10	0.98 (0.20)	0123456
78	182 (27)	2.76	4.48	0.70 (0.28)	639 (64)	3.0	6.50	1.04 (0.21)	012345
79	200 (30)	2.80	2.10	0.34 (0.20)	1035 (104)	3.0	0.60	0.10 (0.02)	0123[5][d]
80	160 (24)	2.60	3.88	0.60 (0.24)	474 (47)	3.0	6.70	1.10 (0.22)	0123[5][d]
81	204 (31)	2.86	1.60	0.30 (0.18)	1500 (150)	3.0	0.50	0.08 (0.04)	01234
82	186 (28)	2.70	2.10	0.34 (0.20)	594 (59)	3.0	3.10	0.50 (0.10)	0123[5][d]
83	186 (20)	2.8	2.6	0.4	⋯	⋯	⋯	⋯	013
85	171 (20)	2.7	1.0	0.16	⋯	⋯	⋯	⋯	013
86	119 (20)	2.00	7.15	1.20 (0.24)	352 (35)	3.0	18.40	3.00 (0.60)	0123[5][d]
87	158 (24)	2.58	5.79	0.90 (0.36)	537 (54)	3.0	4.60	0.74 (0.15)	01235
88	171 (26)	2.69	4.56	0.70 (0.28)	633 (63)	3.0	3.60	0.58 (0.12)	01234
89	184 (28)	2.78	4.26	0.70 (0.28)	551 (55)	3.0	11.10	1.78 (0.36)	012345
90	243 (36)	2.95	2.17	0.30 (0.18)	670 (67)	3.0	8.90	1.44 (0.29)	012345
91	184 (28)	2.77	5.26	0.80 (0.32)	673 (67)	3.0	9.60	1.54 (0.31)	012345
92	179 (27)	2.75	4.79	0.80 (0.32)	637 (64)	3.0	5.00	0.81 (0.16)	012345
93	163 (24)	2.62	5.53	0.90 (0.36)	526 (53)	3.0	6.10	0.98 (0.20)	012345
94	165 (25)	2.64	5.15	0.80 (0.32)	626 (63)	3.0	4.20	0.68 (0.14)	01234
95	130 (20)	2.20	11.40	1.84 (0.37)	403 (40)	3.0	22.40	3.60 (0.72)	0123[5][d]
96	183 (28)	2.80	2.90	0.46 (0.28)	521 (52)	3.0	6.70	1.10 (0.22)	0123[5][d]
99	188 (20)	2.8	1.2	0.2	⋯	⋯	⋯	⋯	013
100	161 (24)	2.60	3.80	0.60 (0.24)	630 (63)	3.0	1.60	0.25 (0.05)	0123[5][d]
101	169 (25)	2.70	4.13	0.66 (0.26)	551 (55)	3.0	4.30	0.70 (0.14)	0123[5][d]
102	189 (28)	2.80	4.29	0.70 (0.28)	634 (63)	3.0	5.90	0.94 (0.19)	012345
103	250 (37)	2.96	2.15	0.30 (0.18)	684 (68)	3.0	7.90	1.27 (0.25)	0123456
104	216 (32)	2.90	3.46	0.60 (0.24)	701 (70)	3.0	9.80	1.57 (0.31)	0123456
105	219 (33)	2.90	2.73	0.40 (0.24)	722 (72)	3.0	5.40	0.87 (0.17)	0123456
106	168 (25)	2.67	7.30	1.20 (0.24)	591 (59)	3.0	5.50	0.89 (0.18)	0123456
107	168 (25)	2.67	6.49	1.00 (0.20)	674 (67)	3.0	3.50	0.57 (0.11)	01234
108	162 (24)	2.62	8.18	1.30 (0.26)	590 (59)	3.0	6.40	1.04 (0.21)	012345
109	185 (28)	2.78	5.46	0.90 (0.36)	619 (62)	3.0	6.30	1.01 (0.20)	012345
110	129 (13)	2.2	6.4	1.02	⋯	⋯	⋯	⋯	01
111	143–454[c]	2.4–3.0[c]	3.0–0.05[c]	0.49–0.09[c]	⋯	⋯	⋯	⋯	13
112	145–430[c]	2.4–3.0[c]	2.9–0.06[c]	0.46–0.01[c]	⋯	⋯	⋯	⋯	13
113	171 (20)	2.7	2.3	0.4	⋯	⋯	⋯	⋯	013
114	160 (24)	2.60	4.20	0.68 (0.27)	638 (64)	3.0	2.50	0.40 (0.08)	0123[5][d]
115	183 (27)	2.77	4.12	0.70 (0.28)	726 (73)	3.0	3.60	0.57 (0.11)	012345
116	214 (32)	2.89	3.52	0.60 (0.24)	696 (70)	3.0	9.50	1.52 (0.30)	0123456
117	221 (33)	2.91	3.22	0.50 (0.20)	687 (69)	3.0	10.80	1.73 (0.35)	0123456
118	194 (29)	2.82	4.77	0.80 (0.32)	691 (69)	3.0	7.60	1.22 (0.24)	012345
119	183 (27)	2.77	5.80	0.90 (0.36)	676 (68)	3.0	5.60	0.90 (0.18)	012345
120	175 (26)	2.72	7.17	1.10 (0.22)	606 (61)	3.0	8.90	1.43 (0.29)	012345
121	190 (29)	2.81	5.15	0.80 (0.32)	653 (65)	3.0	7.10	1.14 (0.23)	0123456
122	205 (31)	2.87	3.89	0.60 (0.24)	658 (66)	3.0	6.10	0.99 (0.20)	012345
123	121 (20)	2.0	8.25	1.3	⋯	⋯	⋯	⋯	01
124	143 (20)	2.4	2.8	0.45	⋯	⋯	⋯	⋯	01
125	150 (20)	2.4	0.2	0.03	⋯	⋯	⋯	⋯	13
126	164–366[c]	2.6–3.0[c]	2.18–0.13[c]	0.35–0.02[c]	⋯	⋯	⋯	⋯	13
127	154 (20)	2.5	4.28	0.67	⋯	⋯	⋯	⋯	013
128	190 (29)	2.80	2.81	0.50 (0.20)	862 (86)	3.0	1.50	0.23 (0.05)	01234
129	195 (29)	2.83	4.57	0.70 (0.28)	690 (69)	3.0	5.60	0.89 (0.18)	0123456
130	225 (34)	2.92	2.90	0.50 (0.20)	683 (68)	3.0	7.80	1.26 (0.25)	0123456
131	186 (28)	2.78	5.32	0.90 (0.36)	655 (66)	3.0	7.70	1.24 (0.25)	0123456
132	181 (27)	2.76	6.79	1.10 (0.22)	643 (64)	3.0	7.80	1.26 (0.25)	012345
133	199 (30)	2.85	4.27	0.70 (0.28)	704 (70)	3.0	6.20	0.99 (0.20)	0123456
134	221 (33)	2.91	3.05	0.50 (0.20)	824 (82)	3.0	3.90	0.62 (0.12)	0123456
135	194 (29)	2.82	4.73	0.80 (0.32)	671 (67)	3.0	4.00	0.65 (0.13)	012345

Table 3
(Continued)

Region[a]	T_1 (unc.)[b] (K)	OPR_1	$N(H_2)_1$ (10^{19} cm^{-2})	$\Sigma(H_2)_1$ (unc.)[b] (10^6 $M_\odot$ kpc^{-2})	T_2 (unc.)[b] (K)	OPR_2	$N(H_2)_2$ (10^{17} cm^{-2})	$\Sigma(H_2)_2$ (unc.)[b] ($10^4 M_\odot$ kpc^{-2})	Lines (0–0 S(...))
139	152 (23)	2.50	4.10	0.65 (0.26)	567 (57)	3.0	3.84	0.62 (0.12)	0123[5][d]
140	182 (27)	2.80	3.30	0.53 (0.21)	584 (58)	3.0	4.10	0.65 (0.13)	0123[5][d]
141	189 (28)	2.80	4.39	0.70 (0.28)	605 (61)	3.0	7.50	1.21 (0.24)	01235
142	213 (32)	2.89	3.88	0.60 (0.24)	693 (69)	3.0	7.70	1.24 (0.25)	0123456
143	185 (28)	2.78	6.61	1.10 (0.22)	692 (69)	3.0	7.90	1.28 (0.26)	0123456
144	176 (26)	2.73	7.09	1.10 (0.22)	616 (62)	3.0	5.70	0.92 (0.18)	012345
145	176 (26)	2.72	6.90	1.10 (0.22)	990.9 (99)	3.0	1.60	0.26 (0.05)	01234
146	156 (23)	2.55	7.94	1.30 (0.26)	832 (83)	3.0	1.60	0.26 (0.05)	012345
147	134 (20)	2.28	5.5	0.89	…	…	…	…	012
149	155–438[c]	2.6–3.0[c]	2.5–0.08[c]	0.4–0.01[c]	…	…	…	…	12
150	129 (20)	2.20	4.70	0.75 (0.30)	579 (58)	3.0	5.10	0.83 (0.17)	0123[5][d]
151	291 (44)	3.00	0.50	0.08 (0.05)	1143 (114)	3.0	0.20	0.02 (0.01)	0123[5][d]
152	189 (28)	2.80	4.20	0.70 (0.28)	565 (57)	3.0	6.90	1.10 (0.22)	0123[5][d]
153	246 (37)	2.95	2.49	0.40 (0.24)	688 (69)	3.0	7.60	1.22 (0.24)	012345
154	193 (29)	2.82	6.20	1.00 (0.20)	697 (70)	3.0	8.20	1.32 (0.26)	0123456
155	157 (24)	2.57	9.25	1.50 (0.30)	409 (41)	3.0	25.50	4.09 (0.82)	01234
156	182 (27)	2.77	2.70	0.40 (0.24)	874 (87)	3.0	1.20	0.19 (0.04)	01234
157	140 (21)	2.36	8.21	1.30 (0.26)	411 (41)	3.0	11.90	1.92 (0.38)	01234
158	126 (20)	2.10	4.60	0.74 (0.30)	815 (82)	3.0	0.60	0.10 (0.02)	0123[5][d]
161	162–339[c]	2.6–3.0[c]	2.2–0.15[c]	0.36–0.02[c]	…	…	…	…	12
162	155 (23)	2.50	4.70	0.76 (0.30)	645 (65)	3.0	1.60	0.30 (0.06)	0123[5][d]
163	191 (29)	2.80	3.10	0.51 (0.20)	714 (71)	3.0	1.70	0.30 (0.06)	0123[5][d]
164	198 (30)	2.84	4.78	0.80 (0.32)	661 (66)	3.0	5.80	0.93 (0.19)	012345
165	216 (32)	2.90	3.78	0.60 (0.24)	709 (71)	3.0	5.80	0.94 (0.19)	012345
166	172 (26)	2.70	6.92	1.10 (0.22)	635 (63)	3.0	7.00	1.12 (0.22)	012345
167	170 (26)	2.68	5.19	0.80 (0.32)	707 (71)	3.0	2.60	0.42 (0.08)	012345
168	149 (22)	2.48	6.69	1.10 (0.22)	470 (47)	3.0	7.90	1.27 (0.25)	01234
169	178 (18)	2.75	1.43	0.23	…	…	…	…	012
170	227 (23)	2.9	0.8	0.14	…	…	…	…	012
171	142 (21)	2.40	4.00	0.63 (0.25)	765 (77)	3.0	1.10	0.20 (0.04)	0123[5][d]
172	213 (32)	2.90	6.20	0.10 (0.06)	1500 (150)	3.0	0.20	0.03 (0.01)	0123[5][d]
173	156 (23)	2.60	5.10	0.82 (0.33)	811 (81)	3.0	0.70	0.01 (0.00)	0123[5][d]
174	165 (25)	2.64	5.99	1.00 (0.20)	645 (64)	3.0	2.10	0.34 (0.07)	01235
175	159 (24)	2.59	10.30	1.60 (0.32)	579 (58)	3.0	6.70	1.07 (0.21)	012345
176	160 (24)	2.60	10.80	1.70 (0.34)	611 (61)	3.0	9.00	1.45 (0.29)	012345
177	163 (24)	2.62	9.51	1.50 (0.30)	635 (63)	3.0	6.00	0.97 (0.19)	012345
178	165 (25)	2.64	7.69	1.20 (0.24)	812 (81)	3.0	2.10	0.33 (0.07)	012345
179	168 (25)	2.67	6.37	1.00 (0.20)	953 (95)	3.0	1.00	0.16 (0.03)	01235
180	141 (20)	2.4	5.87	0.94	…	…	…	…	012
181	141 (20)	2.4	6.3	1.0	…	…	…	…	012
182	147 (22)	2.45	6.30	1.00 (0.20)	596 (60)	3.0	3.70	0.59 (0.12)	01235
183	153 (23)	2.52	7.88	1.30 (0.26)	602 (60)	3.0	3.80	0.60 (0.12)	01235
184	155 (23)	2.50	8.60	1.39 (0.28)	659 (66)	3.0	2.50	0.04 (0.02)	0123[5][d]
185	143 (21)	2.40	16.70	2.70 (0.54)	664 (66)	3.0	2.60	0.42 (0.08)	01235
186	156 (23)	2.56	10.80	1.70 (0.34)	650 (65)	3.0	3.70	0.60 (0.12)	012345
187	156 (23)	2.56	14.40	2.30 (0.46)	651 (65)	3.0	6.00	0.96 (0.19)	0123456
188	151 (23)	2.50	14.70	2.40 (0.48)	435 (43)	3.0	19.60	3.16 (0.63)	01234
189	152 (23)	2.52	14.90	2.40 (0.48)	699 (70)	3.0	3.80	0.61 (0.12)	012345
190	155 (23)	2.54	10.40	1.70 (0.34)	658 (66)	3.0	5.00	0.80 (0.16)	01235
191	134 (20)	2.30	3.00	0.49 (0.29)	412 (41)	3.0	23.60	3.80 (0.76)	0123[5][d]
192	113 (17)	1.89	13.00	2.10 (0.42)	493 (49)	3.0	9.50	1.52 (0.30)	0123[5][d]
193	100 (15)	1.59	23.10	3.70 (0.74)	358 (36)	3.0	36.00	5.79 (1.16)	01235
194	140 (21)	2.37	14.00	2.20 (0.44)	568 (57)	3.0	10.60	1.71 (0.34)	01235
195	158 (24)	2.58	9.80	1.60 (0.32)	681 (68)	3.0	5.80	0.93 (0.19)	01235
196	149 (22)	2.48	16.10	2.60 (0.52)	658 (66)	3.0	5.50	0.89 (0.18)	01235
197	150 (22)	2.49	19.80	3.20 (0.64)	572 (57)	3.0	9.10	1.46 (0.29)	0123456
198	148 (22)	2.47	25.10	4.00 (0.80)	554 (55)	3.0	14.20	2.29 (0.46)	012345
199	156 (23)	2.56	15.70	2.50 (0.50)	560 (56)	3.0	13.10	2.10 (0.42)	012345
200	157 (24)	2.57	11.10	1.80 (0.36)	556 (56)	3.0	10.50	1.69 (0.34)	01235
201	140 (21)	2.40	11.90	1.90 (0.38)	440 (44)	3.0	21.50	3.50 (0.70)	0123[5][d]
202	161–487[c]	2.6–3.0[c]	2.0–0.1[c]	0.67–0.02[c]	…	…	…	…	123
203	148 (22)	2.40	6.10	1.00 (0.20)	678 (68)	3.0	2.40	0.40 (0.08)	0123[5][d]
204	145 (22)	2.40	10.40	1.70 (0.34)	584 (58)	3.0	3.50	0.60 (0.12)	0123[5][d]

Table 3
(Continued)

Region[a]	T_1 (unc.)[b] (K)	OPR_1	$N(H_2)_1$ (10^{19} cm^{-2})	$\Sigma(H_2)_1$ (unc.)[b] (10^6 $M_\odot$ kpc^{-2})	T_2 (unc.)[b] (K)	OPR_2	$N(H_2)_2$ (10^{17} cm^{-2})	$\Sigma(H_2)_2$ (unc.)[b] ($10^4 M_\odot$ kpc^{-2})	Lines (0–0 S(...))
205	146 (22)	2.40	11.80	1.90 (0.38)	489 (49)	3.0	11.70	1.90 (0.38)	0123[5]
206	166 (25)	2.65	7.35	1.20 (0.24)	597 (60)	3.0	7.40	1.18 (0.24)	01234
207	226 (34)	2.92	3.85	0.60 (0.24)	1069 (107)	3.0	1.40	0.22 (0.04)	012345
208	148 (22)	2.46	26.60	4.30 (0.86)	605 (61)	3.0	10.40	1.67 (0.33)	012345
209	155 (23)	2.55	21.20	3.40 (0.68)	634 (63)	3.0	9.80	1.58 (0.32)	012345
210	140 (21)	2.40	27.60	4.40 (0.88)	429 (43)	3.0	36.70	5.90 (1.18)	0123[5][d]
211	151 (23)	2.50	12.90	2.10 (0.42)	429 (43)	3.0	24.10	3.90 (0.78)	0123[5][d]
212	143 (22)	2.40	9.40	1.50 (0.30)	463 (46)	3.0	13.10	2.10 (0.42)	0123[5][d]

Notes.
[a] Regions defined from Figure 1(b).
[b] 1σ uncertainties shown in brackets.
[c] Not enough points to fit two temperatures. Range based on single-temperature fits to lowest three transitions with and without the 3σ S(0) upper limit.
[d] Marginal detection of 0–0 S(5) line provides additional information to allow two-temperature fit.

detected points and a hard lower limit to the temperature by treating the S(0) upper limit as a firm detection. This is important because the 0–0 S(0) provides an anchor point for the coldest gas, and effectively gives an upper limit to the H_2 mass, which is dominated by the cold component. In cases where this was done, the values mapped closely to adjacent positions where S(0) was detected, implying that the lower temperature derived in this way has some validity.

4.2. Power-law Temperature Model

Considering the diverse range of heating environments in the interstellar medium (ISM) in the galaxy, the traditional method of fitting discrete temperature components to the H_2 excitation diagram is only an approximation and may not be realistic in many cases—especially in the presence of shocks. Theoretical studies have demonstrated that H_2 line cooling by molecules in shocks should follow a power-law temperature distribution (Hollenbach & McKee 1979; Burton 1987). Neufeld & Yuan (2008) successfully used a power-law temperature distribution to fit the mid-infrared H_2 rotational-line fluxes of shocked regions in the supernova IC 443.

We follow the approach of Togi & Smith (2016) by assuming a continuous power-law temperature distribution for the H_2, and use this to fit the excitation diagrams and calculate the total H_2 gas mass in the ISM by extrapolating to lower temperatures. We assume that the column density of H_2 molecules is distributed according to a power-law function with respect to temperature, $dN \propto T^{-n}\, dT$, where dN is the number of molecules in the temperature range T to $T + dT$. The model consists of three parameters: the upper and lower temperature bounds, and the power-law index, denoted by T_u, T_ℓ, and n, respectively. T_ℓ can be thought of as the lowest (asymptotic) temperature found in the range of possible temperatures needed to explain the excitation of the gas. If T_ℓ is well constrained (see later), and the single power-law approximation is valid, molecular gas masses can be explored down to temperatures as low as ~50 K, significantly lower than those temperatures that excite the rotational transitions (>80–100 K; Togi & Smith 2016). Keeping the upper temperature, T_u, fixed at 2000 K and varying T_ℓ and n, we fit the H_2 excitation diagram for each square region in the grid of our mapped area of the Quintet. Figure 5 provides an example of a model fit (red solid line) to the observed H_2 line ratios (black points) in the excitation

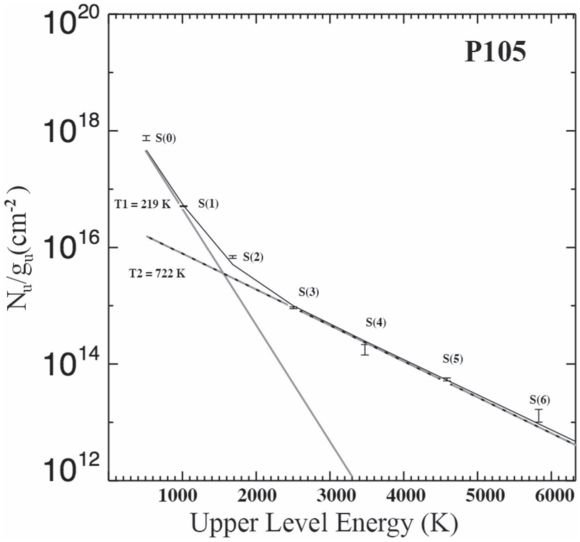

Figure 4. A fit of the excitation diagram of warm molecular hydrogen with two temperatures for position 105 in the center of the the Quintet filament. The gray solid and dotted lines represent the thermal components $T_1 = 219$ K and $T_2 = 722$ K, which contribute to the final fit shown by the black solid line. The values for each of the seven H_2 lines are shown with 1σ uncertainties.

diagram of the square region 105, with $n = 4.4$ in the temperature range 100–2000 K. This is the same region shown in the two-temperature fit of Figure 4, and it is clear that the power-law fit more smoothly captures the change in shape of the excitation diagram than the two-temperature approach in this case. As discussed in Appendix B, there are some regions where the power-law model fits less well, leading to a poorly determined value of T_ℓ.

4.3. MHD Shock Modeling

In a third approach to derive the H_2 physical parameters, and to place the heating of the gas on a more physical footing, we fit the observed H_2 line fluxes with the MHD shock models, using the approach presented in Guillard et al. (2009). We assume that the H_2 emission is powered by the dissipation of mechanical energy in molecular gas at relatively low density ($n_H = 10^2$–10^4 cm^{-3}), as derived by Guillard et al. (2009) and Appleton et al. (2013). We use the grid of MHD shock models presented in Lesaffre et al. (2013). The code computes the

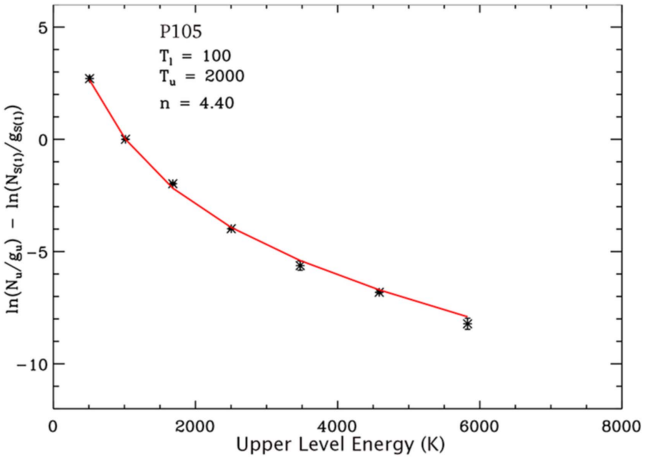

Figure 5. Power-law model fit (red solid line) to the observed H_2 line ratios (black points) in an excitation diagram for the square region numbered 105 in our mapped area (the same region as in Figure 4).

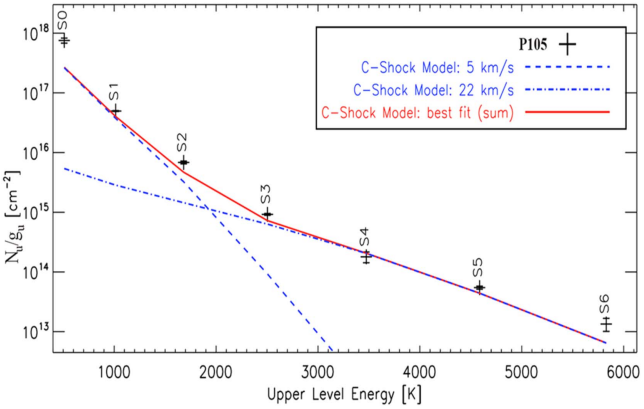

Figure 6. H_2 excitation diagram fitted with a combination of two models at 5 and 22 km s^{-1}. The pre-shock densities are 1×10^4 and 1×10^3 H cm^{-3} respectively.

populations of 150 rotation–vibration H_2 levels in parallel to the MHD equations. The molecular gas is heated to a range of post-shock temperatures that depend on the shock velocity, the pre-shock density, and the intensity of the magnetic field (which is assumed to be perpendicular to the direction of shock propagation). Our grid of shock models include a range of different shock speeds, from 3 to 35 km s^{-1}, and we tested three pre-shock densities, $n_H = 10^2$, 10^3, and 10^4 cm^{-3}. The initial ortho-to-para ratio is set to 3, and the intensity of the pre-shock magnetic field in μG is set to the square root of the pre-shock density in cm^{-3} (i.e., 30 μG at $n_H = 10^3$ cm^{-3}). The magnetic field corresponding to the minimum-energy equipartition is 10 μG, derived from observations of the radio continuum averaged over large kiloparsec scales in the filament by Xu et al. (2003). Therefore, the values used in the models are reasonable, given the much smaller scales that would be involved in the shocks (see Guillard et al. 2009). The H_2 line fluxes are computed when the post-shock gas has cooled down to temperatures of 50 K and 120 K, chosen to compare our shock modeling results to single/two-temperature or power-law fits. At a given pre-shock density, the shock velocity is the only parameter we allow to vary. Figure 6 shows an example of an H_2 excitation diagram fitted with two shock models.

We fit the H_2 excitation diagrams with a combination of two shock velocities and two pre-shock densities. This provides a better fit to the data than fixing the same pre-shock density for both shocks, while keeping the number of free parameters to four.

In reality, we expect a distribution of shock velocities, but Lesaffre et al. (2013) have shown that in the case of a preliminary analysis of the H_2 excitation in Stephan's Quintet (based on a single position in the filament), the favored probability distribution function of the shock velocities is a sum of two narrow Gaussian functions centered at two shock velocities. Following this approach, we simultaneously fit up to seven H_2 rotational lines for each position in the filament, and determine the best combination of shock velocities that minimizes the reduced chi-squared for each set of excitations. The H_2 masses at each point are derived by multiplying the gas cooling time (down to 100 K) by the gas mass flow (the mass of gas swept by the shock per unit time) required to match the H_2 line fluxes (Guillard et al. 2009). The total warm H_2 masses are obtained by summing these over the whole structure (see Section 6 for comparison of the warm gas masses obtained by the various methods).

5. Model Results

5.1. One- or Two-temperature Analysis

Figure 7 shows the distributions of temperatures T_1 and T_2 across the Quintet. The map of T_1, the lower temperature, in Figures 7(a) and (b) shows cooler gas in the northern part of the filament with a quite broad distribution, whereas the temperature peaks ($T_1 > 200$ K) near the center and to the south of the main filament. The situation is similar for the map of component T_2 (Figures 7(c) and (d)) where there are several peaks in the hottest component. The hottest region in both the T_1 and T_2 maps is in the south of the filament. We will see that this is a general result of our modeling. The coolest T_1 and T_2 components lie near the extragalactic star formation site called SQ-A by Xu et al. (2005, see label in Figure1(b)).[14] The fact that the gas is hotter away from this star formation region supports the suggestion of Paper 1, based on an analysis of H_2/PAH ratios, that UV radiation from star formation is not the dominant heating mechanism in the filament. Another feature of the temperature maps shown in Figure 7 is that the warm H_2 component extends significantly in the direction of NGC 7319, and indeed H_2 emission is seen to the very edge of the eastern boundary of the region we are modeling. Unfortunately the spectroscopic diagnostic used in our current analysis (both the IRS LL and SL modules) does not extend far enough to follow this distribution further to the east. However, we know from the maps using the LL module (see for example Figure 1(a)) that the gas does extend all the way to NGC 7319. We will discuss the nature of this eastward extension in Section 7.2.

5.2. Analysis of Power-law Index

Figure 8(a) shows a 2D color plot for power-law indices in the shock region of the Quintet with contours of equal power-law index superimposed. Detailed results are also presented in Table 4. Figure 8(b) shows the same contours superimposed on the optical image of the galaxy. The contour levels map the main shock region of the filament very well, creating the impression of a curved structure that follows faint Hα features seen on the *HST* image. A large number of H_2 molecules are at

[14] We note that not all of SQ-A is covered by our observations.

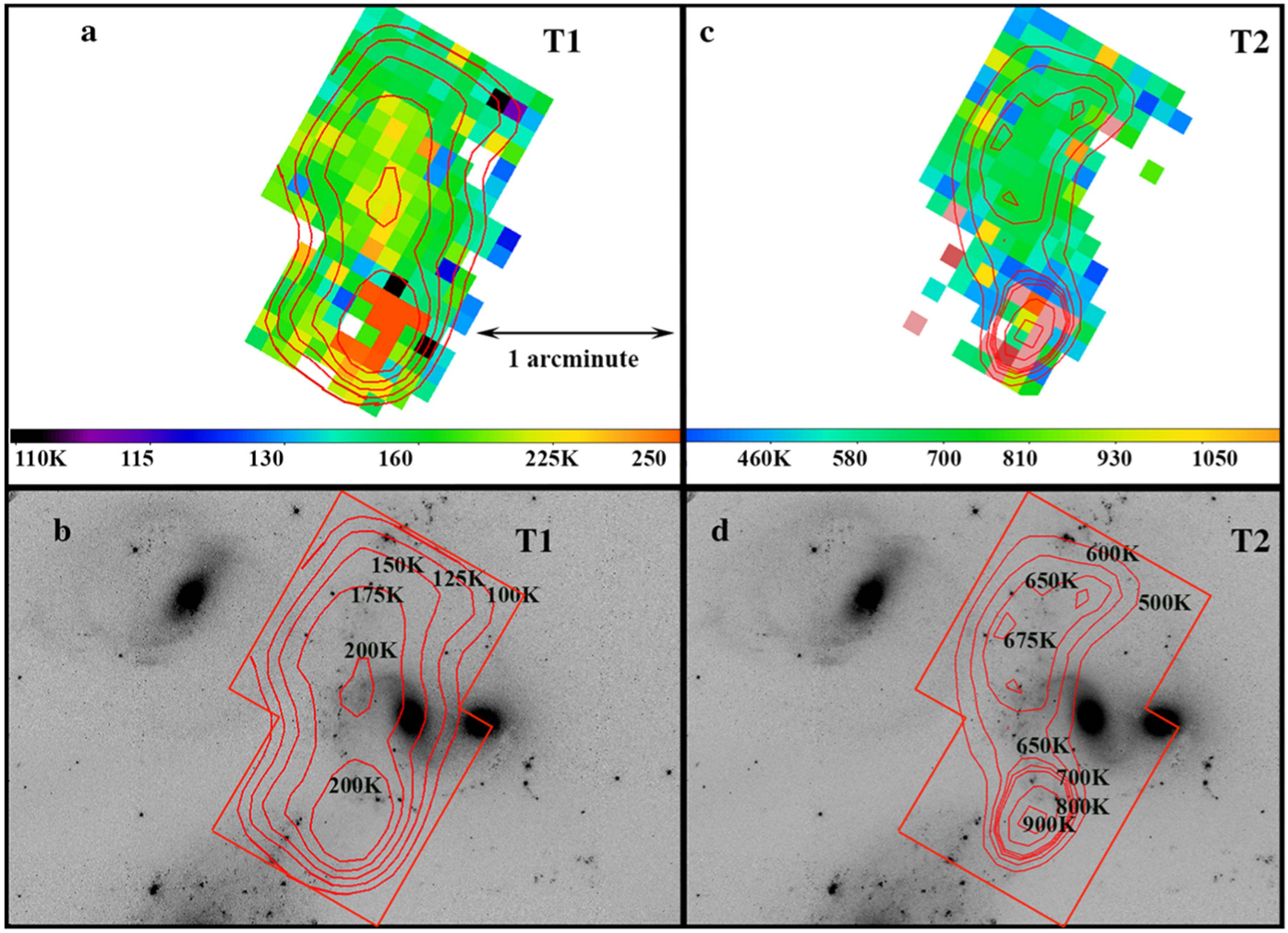

Figure 7. Map of the temperature distribution of the warm H_2 gas derived from a two-temperature fit to the H_2 excitation diagrams at each sampled position. (a) Image of the lowest temperature (T_1) map, with contours in K; (b) the same map superimposed on the F665N *HST* image of the Quintet; (c) image of the higher temperature component (T_2) with contours; (d) the T_2 contours superimposed on the F665N *HST* image. The contour representation includes some spatial averaging to show general trends.

high temperatures, leading to a flatter or lower power-law index in the warmest parts of the shocks because more power escapes from the high-J transitions. This is noticeable in the figure where the power-law index shows a gradient from its highest values of 4.8–5 in the north of the filament, transitioning through the center of the filament (with a peak at 4.45), and reaching the lowest values (4.2–4.3) in the south. Because of the need to include many lines in this fitting, the modeling does not extend as far to the east as the two-temperature fitting, and so the extension in the direction of NGC 7319 is less obvious, although the spreading of the contours in the mid-shock region shows a bulge in the direction of the "bridge" marked in Figure 3.

The values of the power-law index in Figure 8 are almost all lower than the mean found for normal galaxies of 4.84 ± 0.61 (Togi & Smith 2016), and they fall in the asymmetric tail in the distribution found in their study of SINGS galaxies. The tail is populated by SINGS galaxies containing nuclei of Seyferts or LINERs. Indeed the only region that approximates to a normal power-law fit is the region near SQ-A, where the value for n lies between 4.8 and 5.1. In the case of the center of the shock ridge, the values are consistently higher than any seen in the study of the SINGS sample. The shocks appear to be raising the temperature of the gas to much higher levels than are seen in more normal galactic environments. In Section 7.1 we argue that this is a result of higher turbulent energy dissipation there, as measured by an increase in velocity dispersion in the diffuse gas.

Another parameter in the power-law method is the asymptotic value of T_ℓ, the lowest extrapolated temperature obtained from the fitting process. In Appendix B we discuss how we calculate this, and how spatial variations in the H_2 excitation can affect how this lower limit is determined. T_ℓ can affect how much mass in colder gas we estimate from the power-law method.

5.3. Analysis of Shock Models

A combination of two shock velocities is required to match the observed H_2 line fluxes, usually a very low-velocity C-type shock (3–6 km s^{-1}, and a stronger shock (20–35 km s^{-1}), which is consistent with the models of Guillard et al. (2009) and Lesaffre et al. (2013) using limited preliminary data from this same survey. In order to fit best the excitation data for the 0–0 S(0) and 0–0 S(1) transitions, we found better results when

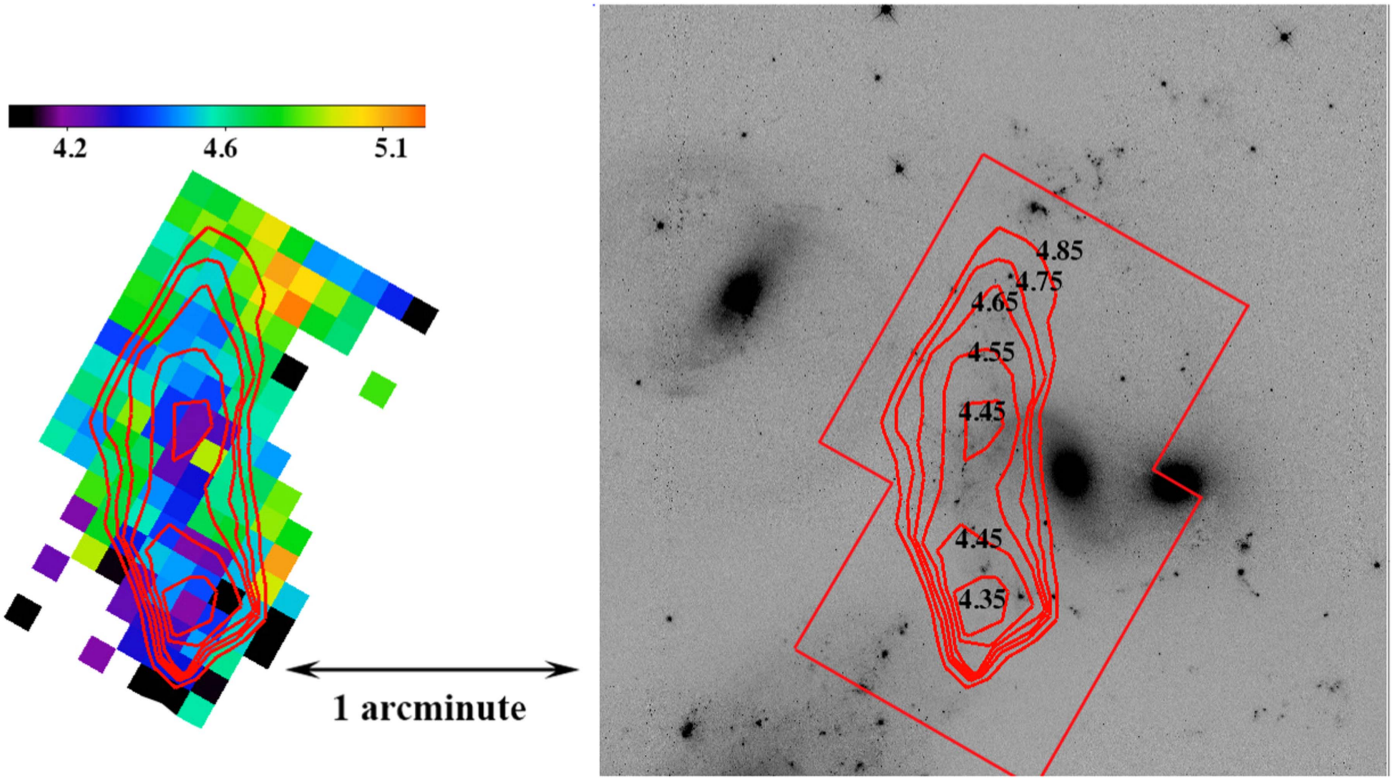

Figure 8. A 2D color plot for the power-law index in our mapped regions of the Quintet. Smooth contours are overlaid on the color plot and the Hα *HST* image from WFC3. The position of the contours clearly marks the shock regions of the Quintet. The center of the shock structure has the lower power-law slope, implying the presence of more excited warm molecular gas. The lowest fitted power-law values are in the center of the ridge line of the shock and to the south. The northern part of the filament has a higher power-law index, implying lower excitation and generally lower temperatures over the range of temperatures sampled. This is similar to that seen in the two-temperature decomposition of Figure 7.

allowing for two different pre-shock densities. The lower velocity shocks are associated with the higher density component. We find that the pre-shock densities that provide the best fit to most of the H_2 line data are $n_H = 10^3\,cm^{-3}$ and a second component with $n_H = 10^4\,cm^{-3}$. On the outside of the ridge and in the bridge regions, pre-shock densities of $n_H = 10^2\,cm^{-3}$ and $n_H = 10^4\,cm^{-3}$ are favored in our models. Although not unique, our fits provide an estimate of the range of shock velocities and pre-shock densities needed to reproduce the H_2 excitation. This phase space is well constrained when six or more H_2 lines are detected (Guillard et al. 2009, 2012), which is the case for ~25% of the spectra.

Since we focus here on the properties of the H_2 excitation itself, this modeling does not attempt to simultaneously fit the H_2 and far-infrared ([O I] and [C II]) line data. Joint fitting of [C II] and H_2 lines in some small extraction regions showed that the [C II]-emitting gas is consistent with excitation by warm H_2 with densities of $n_H \approx 10^{2-3}\,cm^{-3}$ (Appleton et al. 2013). On the other hand, the discovery of pH_2O emission in the same paper requires that some components of the shocked gas must have even higher densities, $n_H > 10^5\,cm^{-3}$. All of this suggests that a broader range of density structure is present in the gas and is not captured by the present models, which fit only the H_2 excitation.

We performed the fitting analysis for all the spectral extractions in Figure 1, and show maps of the two shock velocities in Figure 9. Those maps clearly show the presence of stronger shocks in the center and the southern part of the galaxy-wide shocked filament. The shocks are also stronger in the orthogonal direction of the filament, toward the bridge structure.

Note that the stronger shocks become J-shocks when their speed exceeds the critical velocity corresponding to the sonic point in the flow (Le Bourlot et al. 2002). For a pre-shock density $n_H = 10^2\,cm^{-3}$ and a magnetic field induction $B = 10\,\mu G$ transverse to the flow, the critical velocity is $V_{crit} \approx 21\,km\,s^{-1}$. We note that we ran a grid of nonmagnetic shock models (only J-shocks) and found very poor fits to the lower excitation lines (especially 0–0 S(0)), which stresses the importance of the magnetic field in softening the heating of the shocked gas and enhancing the population of the lower excitation rotational levels with respect to higher ones. The shock model parameters, gas cooling times, mass flows, and warm H_2 masses are provided in Table 5.

6. The Mass of Warm Molecular Gas and the Warm Mass Fraction

The three methods of fitting the excitation diagrams of the warm H_2 allow us to estimate the total warm molecular mass in the areas that we have sampled. For the two-temperature method, the fits for each region can be summed to directly provide a total warm molecular mass for the whole mapped area. For the power-law models, an important factor in determining the total warm molecular mass is the value of the asymptotic temperature T_ℓ (see Section 4.2) determined in the fitting process. This results in two kinds of behavior, gas in the center of the shock in which the bulk of the gas is

Table 4
Power-law Model Results for the Quintet

Region	$n(\delta n)$	T_ℓ (K)	$M(T > 120$ K) ($10^6\,M_\odot$)	$\frac{M(T>120\text{ K})}{M_{\rm total}}$ (%)	Class Type	Region	$n(\delta n)$	T_ℓ (K)	$M(T > 120$ K) ($10^6\,M_\odot$)	$\frac{M(T>120\text{ K})}{M_{\rm total}}$ (%)	Class Type
4	3.44 (0.07)	50	1.27	11.8	I	109	4.78 (0.04)	100	6.58	50.2	II
5	3.84 (3.84)	80	1.49	31.7	III	113	4.19 (0.51)	50	1.20	6.1	I
7	3.78 (3.78)	80	1.26	32.4	III	114	4.52 (0.13)	50	2.12	4.6	I
8	4.19 (4.19)	80	1.67	27.4	III	115	4.57 (0.08)	100	4.47	52.2	II
9	3.65 (3.65)	80	1.01	34.1	III	116	4.25 (0.03)	100	6.68	55.3	II
10	4.37 (0.12)	50	1.33	5.22	I	117	4.20 (0.02)	110	6.84	75.7	II
12	4.24 (4.24)	80	1.35	26.9	III	118	4.40 (0.03)	100	6.28	53.8	II
13	4.62 (0.12)	110	4.23	73	II	119	4.59 (0.04)	90	6.00	35.6	II
14	3.92 (0.03)	80	3.02	26.9	II	120	4.59 (0.03)	90	6.42	35.6	II
15	3.79 (0.05)	50	2.01	8.66	I	121	4.59 (0.03)	85	6.59	29.0	II
16	4.58 (0.12)	125	2.76	100	II	122	4.66 (0.03)	105	6.95	61.4	II
17	4.16 (0.05)	50	2.67	6.29	I	127	4.78 (0.19)	50	1.61	3.66	I
18	4.30 (4.30)	80	1.90	26.3	I	128	4.61 (0.10)	100	3.27	51.8	II
20	3.21 (0.07)	50	0.60	14.4	I	129	4.66 (0.04)	107	6.82	65.7	II
22	4.44 (4.44)	80	1.81	24.8	III	130	4.42 (0.03)	105	6.90	63.4	II
23	4.06 (0.10)	120	2.66	100	II	131	4.49 (0.05)	100	6.36	52.9	II
24	4.34 (0.05)	135	3.83	100	II	132	4.55 (0.07)	90	6.73	36.0	II
25	4.34 (0.05)	120	3.59	100	II	133	4.45 (0.03)	90	6.13	37.0	II
26	4.31 (0.06)	50	2.45	5.54	I	134	4.45 (0.03)	50	6.03	5.04	I
27	4.13 (4.13)	80	1.70	28.2	III	135	4.86 (0.06)	105	7.32	59.7	II
28	4.74 (4.74)	80	2.09	21.9	III	139	4.63 (0.17)	50	1.83	4.15	I
33	4.64 (0.16)	50	1.87	4.13	I	140	4.72 (0.10)	95	3.68	41.9	II
34	4.51 (4.51)	80	3.64	24.1	III	141	4.58 (0.04)	105	5.64	62.0	II
35	4.26 (0.04)	85	3.03	32.5	II	142	4.55 (0.02)	100	7.87	52.4	II
36	4.29 (0.11)	50	2.16	5.61	I	143	4.50 (0.02)	81	7.09	25.8	II
37	4.23 (4.23)	80	1.65	27.0	III	144	4.81 (0.05)	100	6.70	49.9	II
38	3.96 (3.96)	80	1.32	30.1	III	145	4.80 (0.06)	90	6.31	33.5	II
39	4.67 (4.67)	80	1.62	22.6	III	146	4.61 (0.07)	50	3.65	4.25	I
40	4.21 (0.22)	50	1.15	6.02	I	147	4.61 (0.31)	50	0.75	4.24	I
41	3.11 (3.11)	80	0.23	42.4	III	150	4.05 (0.26)	50	0.93	6.92	I
42	3.72 (0.16)	50	0.71	9.22	I	151	4.72 (0.24)	80	2.49	22.2	II
43	4.57 (0.14)	100	2.97	52.1	II	152	4.68 (0.07)	105	5.66	61.2	II
44	4.39 (0.07)	135	3.54	100	II	153	4.47 (0.03)	100	8.01	53.1	II
45	4.15 (0.04)	135	3.10	100	II	154	4.49 (0.04)	85	7.90	30.1	II
46	4.50 (0.07)	50	3.10	4.67	I	155	4.73 (0.09)	85	6.42	27.6	II
47	4.24 (0.28)	50	1.63	5.88	I	156	4.82 (0.09)	70	4.03	12.7	II
48	4.06 (0.09)	50	1.44	6.84	I	157	4.92 (0.16)	50	3.05	3.24	I
49	4.94 (0.09)	95	2.46	39.3	II	158	4.85 (0.34)	50	0.55	3.44	I
52	4.03 (0.16)	50	1.26	7.06	I	162	4.86 (0.15)	50	2.14	3.4	I
53	4.55 (0.04)	135	3.01	100	II	163	4.92 (0.11)	100	4.28	48.9	II
54	3.90 (0.05)	50	3.19	7.91	I	164	4.73 (0.04)	100	7.39	50.6	II
55	4.43 (0.03)	120	5.88	100	II	165	4.57 (0.03)	100	7.71	52.1	II
56	4.51 (0.02)	100	4.77	52.7	II	166	4.59 (0.04)	71	5.42	14.9	II
57	4.55 (0.11)	100	3.27	52.3	II	167	4.69 (0.04)	50	3.63	3.95	I
58	4.35 (0.08)	50	2.25	5.32	I	168	4.81 (0.16)	65	3.02	9.48	II
59	4.78 (0.08)	50	2.36	3.66	I	169	4.99 (0.89)	50	1.26	3.04	I
60	4.17 (0.08)	50	1.57	6.24	I	170	4.79 (0.32)	50	1.01	3.61	I
62	4.56 (0.25)	50	1.51	4.43	I	171	4.68 (0.22)	50	1.02	3.99	I
63	4.98 (0.08)	95	3.47	39.5	II	172	4.78 (0.45)	50	1.22	3.66	I
64	4.55 (0.07)	75	4.51	18.9	II	173	5.21 (0.29)	77	2.59	15.1	II
65	4.22 (0.07)	75	4.39	22.1	II	174	5.03 (0.10)	85	4.07	24.9	II
66	4.18 (0.05)	100	4.94	56	II	175	4.89 (0.05)	65	5.86	9.21	II
67	4.41 (0.08)	90	4.30	37.5	II	176	4.57 (0.04)	50	5.84	4.39	I
68	4.60 (0.12)	80	3.11	23.3	II	177	4.68 (0.05)	60	5.60	7.82	II
69	4.73 (0.15)	85	2.44	27.6	II	178	4.60 (0.05)	50	4.25	4.30	I
70	4.85 (0.16)	85	2.23	26.5	II	179	4.57 (0.06)	50	3.75	4.38	I
72	4.93 (0.39)	80	1.28	20.3	II	180	4.81 (0.25)	50	1.20	3.57	I
73	5.15 (0.22)	80	2.82	14.6	II	181	4.67 (0.21)	50	1.27	4.02	I
74	4.56 (0.15)	50	2.89	4.42	I	182	4.71 (0.11)	50	2.19	3.90	I
75	4.77 (0.11)	100	4.50	50.3	II	183	4.91 (0.08)	54	3.52	4.52	II
76	4.72 (0.07)	120	6.72	100	II	184	5.05 (0.16)	65	4.13	8.32	II
77	4.37 (0.02)	100	5.94	54.1	II	185	5.15 (0.07)	50	4.85	2.65	I
78	4.50 (0.04)	80	4.62	24.2	II	186	4.93 (0.05)	60	5.24	6.56	II

Table 4
(Continued)

Region	$n(\delta n)$	T_ℓ (K)	$M(T > 120$ K) ($10^6\,M_\odot$)	$\frac{M(T>120\text{ K})}{M_{\rm total}}$ (%)	Class Type	Region	$n(\delta n)$	T_ℓ (K)	$M(T > 120$ K) ($10^6\,M_\odot$)	$\frac{M(T>120\text{ K})}{M_{\rm total}}$ (%)	Class Type
79	4.81 (0.13)	90	3.39	33.5	II	187	4.82 (0.05)	50	6.81	3.52	I
80	4.67 (0.12)	85	2.61	28.2	II	188	4.91 (0.06)	75	7.45	15.9	II
81	4.53 (0.13)	87	2.36	32.4	II	189	4.84 (0.04)	50	5.94	3.48	I
82	4.63 (0.04)	100	2.56	51.6	II	190	4.71 (0.06)	50	4.62	3.89	I
83	4.61 (0.31)	100	2.60	51.8	II	191	3.91 (0.24)	50	0.67	7.86	I
86	4.81 (0.20)	68	1.95	11.8	II	192	4.37 (0.13)	50	1.46	5.25	I
87	4.92 (0.11)	80	3.37	20.4	II	193	4.47 (0.10)	50	2.83	4.79	I
88	4.65 (0.10)	80	3.81	22.8	II	194	4.52 (0.05)	50	3.91	4.59	I
89	4.65 (0.04)	110	5.94	72.8	II	195	4.50 (0.04)	50	4.61	4.65	I
90	4.32 (0.03)	110	6.67	74.9	II	196	4.79 (0.05)	50	5.65	3.64	I
91	4.24 (0.02)	70	5.55	17.5	II	197	5.02 (0.05)	56	8.16	4.70	II
92	4.71 (0.05)	95	4.93	41.6	II	198	4.90 (0.03)	50	9.83	3.28	I
93	4.79 (0.08)	85	3.75	27.1	II	199	4.76 (0.06)	50	8.11	3.72	I
94	4.49 (0.08)	50	3.11	4.72	I	200	4.72 (0.05)	50	6.07	3.83	I
95	4.55 (0.07)	50	3.31	4.47	I	201	4.56 (0.08)	50	4.47	4.42	I
96	4.60 (0.21)	100	3.45	51.8	II	202	3.44 (0.21)	50	0.47	11.8	I
99	4.81 (0.32)	100	1.37	49.9	II	203	4.47 (0.25)	50	1.85	4.78	I
100	4.88 (0.20)	85	2.49	26.2	II	204	5.00 (0.17)	50	3.47	3.02	I
101	4.71 (0.12)	85	3.75	27.9	II	205	4.69 (0.07)	50	4.47	3.95	I
102	4.64 (0.04)	100	5.50	51.5	II	206	4.56 (0.05)	50	5.28	4.45	I
103	4.95 (0.09)	198	15.5	100	II	207	4.77 (0.03)	65	9.00	9.93	II
104	4.20 (0.02)	100	6.54	55.8	II	208	4.83 (0.03)	50	9.32	3.51	I
105	4.40 (0.03)	100	5.55	53.8	II	209	4.76 (0.03)	50	9.69	3.73	I
106	4.91 (0.07)	80	5.68	20.5	II	210	4.80 (0.04)	50	9.82	3.60	I
107	4.68 (0.07)	70	4.44	13.8	II	211	4.85 (0.06)	80	7.15	21.0	II
108	4.67 (0.06)	70	4.95	13.8	II	212	4.64 (0.11)	50	3.53	4.13	I

warmer than 100–120 K, and a second set of regions, mainly away from the main shock, where the temperatures extend potentially down to 50 K. The details of how we extrapolate spectra of this second kind is summarized in Appendix B. Finally, the shock modeling also provides an alternative estimate of the amount of warm gas being processed through the shocks, since the models provide the mass flow rate into the shock and the cooling time for a given temperature. The total mass of warm gas is therefore the product of these two quantities for $T > 120$ K. The results are tabulated in Table 1.

Given the different approaches used to measure the H_2 masses, the three methods agree well in terms of how much warm ($T > 120$ K) gas is present over the mapped area. For the two-component temperature fitting method, most of the mass is (as expected) contained in the gas with the lowest temperature (T_1) component ($1.1 \times 10^9\,M_\odot$), with only 1% ($0.12 \times 10^8\,M_\odot$) being contained in the warmer component, T_2. The two-temperature method agrees well with the mass of warm ($T > 120$ K) gas processed through shocks ($1.0 \times 10^9\,M_\odot$). The power-law method yields a slightly lower warm H_2 mass of $(7.1 \pm 1.5) \times 10^8\,M_\odot$ than either of the other methods, but we have been more restrictive in the area sampled by this method. Nevertheless, to within 30%, all three methods are in agreement. As Table 1 shows, the majority of the warm gas that is processed through the shocks lies in the lower velocity shock component, whereas the mass of gas processed through the faster shocks is quite small.

What can we say about the warm to total molecular fraction? Guillard et al. (2012) estimated the total H_2 mass in the Quintet filament from IRAM 30 m observations to be $5 \times 10^9\,M_\odot$ (assuming a value of $N(H_2)/I_{\rm co}$ of $2 \times 10^{20}\,{\rm cm}^{-2}\,({\rm K\,km\,s}^{-1})^{-1}$ appropriate for the Galaxy). Adopting the two-temperature warm H_2 mass, we obtain a warm ($T > 120$ K)/total H_2 mass fraction of 0.22. However, since the IRAM beams did not cover the whole IRS spectral-fitting region, the total mass of gas was only approximately estimated. We also include some estimates of the warm mass fraction obtained by the two-temperature method over the area of three individual IRAM pointings in Table 1. In those cases, where the warm H_2 mass is dominated by hotter gas, the ratio of warm to total H_2 mass drops to 0.1.

An alternative method for estimating to total molecular gas down to some lower temperature has been presented by Togi & Smith (2016). The method relies on extrapolating the power-law index derived from the measured rotational lines to much lower temperatures under the assumption that a single power-law index applies to all the gas. The method, which has a practical lower limit of $T = 50$ K (see Appendix B for more details), has some advantages over conventional methods. For example, it is based on direct emission from the H_2 molecules, and therefore does not need to rely on assumed relationships between other tracers (such as CO) and molecular hydrogen. The power-law method can self-consistently estimate the fraction of warm gas (say $T > 120$ K) compared with the total H_2 mass found by extrapolating the power law down to lower temperatures. Using this method the warm gas fraction is

$$\frac{M(>120\text{ K})}{M_{{\rm total}(T_\ell)}} = \frac{\int_{120}^{T_u} T^{-n} dT}{\int_{T_\ell}^{T_u} T^{-n} dT}, \quad (1)$$

where (see Appendix B) T_ℓ has a practical lower limit of 50 K.

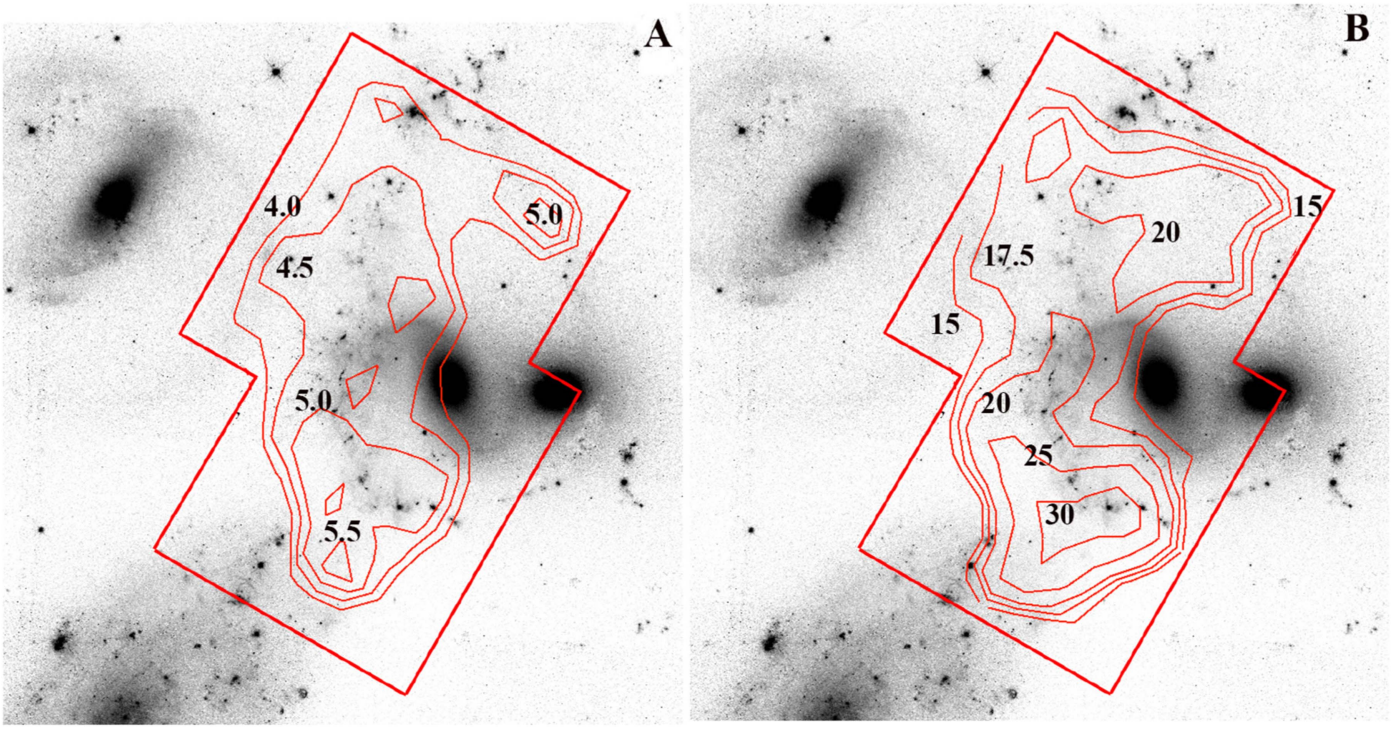

Figure 9. The velocity field (in km s^{-1}) of the low (A) and high (B) shock components required to fit the H_2 excitation diagrams superimposed on the optical *HST* image of the Quintet. The general trend of increasing shock velocity from the north to the south is evident, as well as a bulge in both components to the east toward NGC 7319 (see text). We also note that higher velocity shocks are seen in the northwest between the arms of the tidal filaments from NGC 7318a and 7318b.

Although the average warm fraction over the whole map, using this method, is 0.1 (Table 1), Figure 10 shows that the fraction is >0.5 in the center of the main shock (in a few places it reaches unity), and is approximately 0.6 in the southern region, between NGC 7318b and the foreground galaxy NGC 7320. Given the uncertainty in extrapolating down to low temperatures using the power-law method, and a similar large uncertainty and known scatter in the $I_{co}/N(H_2)$ relationship used by Guillard et al. (2012) in their estimate of the total mass of H_2, the results for the warm mass fraction using the various methods are consistent.

7. Properties across and along the Main H_2 Filament

We present two "sectional slices" through the H_2 structure both across the main shock from west to east (in Figure 11) and along the main shock from south to north (Figure 12). These slices help to illustrate some general properties of the gas in the main filament. The inset images (one per figure) show the direction (arrow) and position of the slices we are considering.

In Figures 11(A) and (B), as we progress from west to east across the main shock, a sharp rise in the fraction of warm gas in the shock is observed, and at the same time a drop in the power-law index at position 104, indicating high overall excitation there. In Figure 11(C), we see that the temperature of the cooler gas (T_1) peaks first, followed by a peak in the warmer component (T_2) further to the east. In Figure 11(D), we show both the molecular mass associated with the hotter (T_2) component and the mass associated with the fast shocks (fast and slow shock velocities are shown in Figure 11(E)). The two track each other and peak at the same position as the minimum in the power-law index. This suggests that the warmer component essentially maps the fast shocks. This is in contrast to Figure 11(F), which shows the mass of gas associated with both the cooler component (T_1) and the low-velocity shock component. Both show a depression in the H_2 mass associated with the slower shocks at the position of the peak, followed by a rise again beyond position 105. There is significantly more mass associated with the cooler components than the warmer, and the depression may be a real deficit of rotationally excited H_2 at the position of the maximum heating. The effect is still present (but less pronounced) in the plot of the total warm H_2 derived from the power-law fitting.

In Figure 11(G) we use the shock modeling to determine the kinetic energy dissipated by the slow and fast shocks. The kinetic energy deposited is $0.5(\dot{M}t_{\rm cool})V^2_{\rm shock}$ [J] (see Table 5), where $\dot{M}$ is the rate of gas processing in $M_\odot$ yr^{-1} (see Table 5). The cooling time, $t_{\rm cool}$, is very short (typically 10^2–10^3 yr). It can be seen that the fast shocks deposit more energy at the position 104, falling off on either side, whereas the slow shocks deposit more energy on either side of the filament, with a decrease at position 104. Nevertheless, the slow shocks appear to deposit more total kinetic energy than the fast shocks. Interestingly, the overall kinetic energy deposited by the slow shocks continues to increase at positions beyond position 106. This is the region that extends into the bridge region between the main shock and NGC 7319.

In Figure 12 we show a very similar set of diagnostic plots to the previous figure, but this time emphasizing a line of points running from south to north along the main ridge of the filament (see inset image and arrow). Here we see a general decrease in excitation from south to north in almost all the indicators. Figures 12(A), (C), and (E) show a general decrease in the warm mass fraction, the temperature (both T_1 and T_2) and model shock velocities (fast and slow) along the filament. On the other hand, the power-law index rises, and the mass associated with the gas also increase northward for all

Table 5
H_2 Fluxes Fitted with Shock Models with Pre-shock Densities $n_H = 10^4$ and 10^3 cm^{-3} for the Slow and Fast Shocks Respectively

Region	V_s[a] (km s^{-1})	Mass Flow (120 K)[b] (10^2 $M_\odot$ yr^{-1})	t_{cool}(120 K)[c] (10^2 yr)	M(120 K)(H_2)[d] (10^5 $M_\odot$)	Mass Flow (50 K)[b] (10^2 $M_\odot$ yr^{-1})	t_{cool}(50 K)[c] (10^2 yr)	M(50 K)(H_2)[d] (10^5 $M_\odot$)
1	6.0	3.25 (0.86)	2.47	0.80 (0.21)	3.23 (0.86)	5.08	1.64 (0.44)
	33.5	3.51 (0.77)	10.86	3.81 (0.84)	2.17 (0.48)	33.27	7.20 (1.59)
2	5.5	6.71 (1.23)	2.30	1.55 (0.28)	6.80 (1.22)	5.42	3.68 (0.66)
	32.5	4.75 (0.26)	6.36	3.02 (0.17)	2.93 (0.16)	32.25	9.44 (0.52)
3	5.5	12.42 (1.32)	2.30	2.86 (0.31)	12.43 (1.32)	5.42	6.74 (0.71)
	32.5	2.92 (0.65)	6.36	1.85 (0.42)	1.76 (0.40)	32.25	5.69 (1.29)
4	7.0	15.25 (0.49)	2.63	4.02 (0.13)	15.22 (0.49)	4.86	7.40 (0.24)
	33.5	2.97 (0.81)	10.86	3.22 (0.88)	1.84 (0.50)	33.27	6.14 (1.67)
5	4.5	73.29 (4.62)	2.29	16.75 (1.06)	72.01 (4.54)	5.91	42.55 (2.68)
	14.5	0.97 (0.05)	4.71	0.46 (0.03)	0.97 (0.05)	6.41	0.62 (0.04)
6	4.5	70.04 (4.91)	2.29	16.00 (1.12)	33.17 (2.24)	5.99	19.87 (1.34)
	21.5	0.10 (0.01)	4.87	0.05 (0.01)	1.40 (0.19)	33.27	4.65 (0.63)
7	4.0	265.90 (18.27)	2.19	58.28 (4.00)	71.57 (4.91)	5.91	42.29 (2.90)
	22.5	0.43 (0.03)	4.80	0.21 (0.01)	0.42 (0.03)	6.48	0.27 (0.02)
8	4.0	263.01 (14.42)	2.19	57.64 (3.16)	247.86 (13.61)	6.38	158.21 (8.69)
	18.0	0.62 (0.03)	4.90	0.30 (0.01)	0.62 (0.03)	6.64	0.41 (0.02)
9	6.5	12.64 (0.59)	2.59	3.28 (0.15)	12.61 (0.59)	4.83	6.09 (0.29)
	33.5	3.59 (0.79)	10.86	3.89 (0.86)	2.23 (0.49)	33.27	7.42 (1.63)
10	4.0	199.64 (13.10)	2.19	43.75 (2.87)	185.54 (12.44)	6.38	118.43 (7.94)
	17.5	0.44 (0.03)	4.93	0.22 (0.01)	0.49 (0.03)	6.61	0.32 (0.02)
11	5.5	5.76 (0.94)	2.30	1.33 (0.22)	5.75 (0.93)	5.42	3.12 (0.50)
	33.0	2.69 (0.60)	8.49	2.29 (0.51)	1.74 (0.39)	32.25	5.62 (1.25)
12	5.5	21.04 (1.21)	2.30	4.85 (0.28)	20.96 (1.20)	5.42	11.37 (0.65)
	34.0	4.30 (0.78)	12.91	5.55 (1.00)	2.71 (0.49)	33.53	9.08 (1.64)
13	4.5	159.70 (4.87)	2.29	36.49 (1.11)	156.82 (4.79)	5.91	92.66 (2.83)
	14.0	0.95 (0.06)	4.64	0.44 (0.03)	0.95 (0.06)	6.35	0.61 (0.04)
14	6.0	38.24 (0.84)	2.47	9.45 (0.21)	38.37 (0.84)	5.08	19.48 (0.43)
	32.5	16.27 (0.70)	6.36	10.35 (0.44)	9.85 (0.42)	32.25	31.76 (1.37)
15	5.5	38.66 (1.23)	2.30	8.90 (0.28)	38.83 (1.22)	5.42	21.05 (0.66)
	32.5	11.91 (0.68)	6.36	7.57 (0.43)	7.17 (0.42)	32.25	23.12 (1.34)
16	5.5	35.43 (1.33)	2.30	8.16 (0.31)	35.26 (1.33)	5.42	19.12 (0.72)
	33.5	3.49 (0.76)	10.86	3.79 (0.82)	2.16 (0.47)	33.27	7.18 (1.56)
17	6.0	30.51 (0.88)	2.47	7.54 (0.22)	30.38 (0.88)	5.08	15.42 (0.45)
	33.0	7.24 (0.62)	8.49	6.14 (0.53)	4.75 (0.41)	32.25	15.31 (1.31)
18	5.5	27.75 (1.23)	2.30	6.39 (0.28)	27.92 (1.21)	5.42	15.14 (0.65)
	25.0	3.05 (0.55)	0.65	0.20 (0.04)	2.50 (0.44)	32.78	8.19 (1.46)
19	5.5	16.84 (1.18)	2.30	3.88 (0.27)	16.85 (1.17)	5.42	9.13 (0.64)
	32.5	2.66 (0.65)	6.36	1.69 (0.42)	1.60 (0.40)	32.25	5.16 (1.29)
20	5.0	25.99 (1.97)	2.32	6.04 (0.46)	26.26 (1.95)	5.99	15.72 (1.17)
	32.5	7.82 (0.66)	6.36	4.97 (0.42)	4.68 (0.40)	32.25	15.08 (1.30)
21	6.0	7.35 (0.80)	2.47	1.82 (0.20)	7.38 (0.79)	5.08	3.75 (0.40)
	32.5	2.59 (0.66)	6.36	1.64 (0.42)	1.54 (0.40)	32.25	4.96 (1.31)
22	5.5	24.65 (1.21)	2.30	5.68 (0.28)	24.61 (1.20)	5.42	13.35 (0.65)
	32.5	2.44 (0.64)	6.36	1.55 (0.41)	1.46 (0.39)	32.25	4.69 (1.26)
23	5.5	44.30 (1.33)	2.30	10.20 (0.31)	44.08 (1.32)	5.42	23.90 (0.72)
	21.0	0.17 (0.03)	4.87	0.08 (0.02)	0.17 (0.03)	6.55	0.11 (0.02)
24	5.5	53.66 (1.29)	2.30	12.36 (0.30)	53.86 (1.28)	5.42	29.20 (0.69)
	24.5	7.48 (0.56)	0.65	0.49 (0.04)	6.34 (0.48)	30.76	19.51 (1.46)
25	5.5	52.02 (1.24)	2.30	11.98 (0.29)	51.83 (1.23)	5.42	28.10 (0.67)
	35.0	11.36 (0.85)	12.43	14.12 (1.06)	7.03 (0.53)	33.70	23.68 (1.78)
26	5.5	35.45 (1.32)	2.30	8.16 (0.30)	35.27 (1.31)	5.42	19.12 (0.71)
	28.0	6.64 (0.62)	0.62	0.41 (0.04)	4.54 (0.42)	27.05	12.27 (1.15)
27	4.0	303.89 (15.60)	2.19	66.60 (3.42)	81.06 (4.16)	5.91	47.89 (2.46)
	22.5	0.36 (0.03)	4.80	0.17 (0.01)	0.35 (0.03)	6.48	0.23 (0.02)
28	4.5	78.34 (4.49)	2.29	17.90 (1.03)	78.44 (4.38)	5.91	46.35 (2.59)
	25.0	4.26 (0.52)	0.65	0.28 (0.03)	3.49 (0.42)	32.78	11.45 (1.38)
29	5.5	18.51 (1.20)	2.30	4.26 (0.28)	18.51 (1.19)	5.42	10.04 (0.64)
	32.5	2.62 (0.65)	6.36	1.67 (0.42)	1.57 (0.40)	32.25	5.06 (1.29)
30	5.5	15.57 (1.22)	2.30	3.59 (0.28)	14.84 (1.25)	5.42	8.04 (0.68)
	32.5	2.81 (0.65)	6.36	1.78 (0.42)	1.83 (0.43)	27.05	4.94 (1.17)
31	6.0	4.40 (0.82)	2.47	1.09 (0.20)	4.37 (0.82)	5.08	2.22 (0.41)
	33.0	2.69 (0.62)	8.49	2.29 (0.53)	1.75 (0.41)	32.25	5.64 (1.31)
32	5.5	10.79 (1.13)	2.30	2.49 (0.26)	10.75 (1.13)	5.42	5.83 (0.61)

Table 5
(Continued)

Region	V_s[a] ($km\ s^{-1}$)	Mass Flow (120 K)[b] ($10^2\ M_\odot\ yr^{-1}$)	t_{cool}(120 K)[c] (10^2 yr)	M(120 K)(H_2)[d] ($10^5\ M_\odot$)	Mass Flow (50 K)[b] ($10^2\ M_\odot\ yr^{-1}$)	t_{cool}(50 K)[c] (10^2 yr)	M(50 K)(H_2)[d] ($10^5\ M_\odot$)
	33.0	2.72 (0.61)	8.49	2.31 (0.52)	1.77 (0.40)	32.25	5.70 (1.29)
33	5.5	23.25 (1.24)	2.30	5.35 (0.29)	23.14 (1.23)	5.42	12.55 (0.67)
	33.5	3.44 (0.75)	10.86	3.73 (0.81)	2.12 (0.46)	33.27	7.05 (1.53)
34	5.5	46.56 (1.25)	2.30	10.72 (0.29)	46.84 (1.24)	5.42	25.40 (0.67)
	24.5	6.50 (0.29)	0.65	0.42 (0.02)	5.55 (0.24)	32.09	17.81 (0.78)
35	6.0	33.18 (0.87)	2.47	8.21 (0.22)	33.15 (0.87)	5.08	16.83 (0.44)
	35.0	10.60 (0.63)	12.43	13.18 (0.79)	6.55 (0.39)	33.70	22.07 (1.32)
36	6.0	23.62 (0.87)	2.47	5.84 (0.21)	23.58 (0.86)	5.08	11.97 (0.44)
	33.0	2.57 (0.67)	8.49	2.18 (0.57)	1.69 (0.44)	32.25	5.46 (1.43)
37	5.5	25.98 (1.19)	2.30	5.98 (0.27)	25.13 (1.21)	5.42	13.63 (0.66)
	33.5	3.57 (0.75)	10.86	3.87 (0.81)	2.10 (0.44)	32.09	6.75 (1.42)
38	5.5	24.70 (1.35)	2.30	5.69 (0.31)	24.66 (1.34)	5.42	13.37 (0.73)
	32.5	2.74 (0.65)	6.36	1.74 (0.41)	1.64 (0.39)	32.25	5.30 (1.27)
39	5.5	19.66 (1.45)	2.30	4.53 (0.33)	19.56 (1.45)	5.42	10.61 (0.78)
	33.0	2.57 (0.60)	8.49	2.18 (0.51)	1.66 (0.39)	32.25	5.37 (1.27)
40	5.5	17.93 (1.12)	2.30	4.13 (0.26)	17.85 (1.12)	5.42	9.68 (0.60)
	33.0	2.66 (0.60)	8.49	2.26 (0.51)	1.72 (0.39)	32.25	5.56 (1.26)
41	6.5	4.31 (0.56)	2.59	1.12 (0.14)	4.29 (0.56)	4.83	2.07 (0.27)
	33.5	3.56 (0.78)	10.86	3.87 (0.85)	2.20 (0.48)	33.27	7.32 (1.61)
42	6.0	11.76 (0.85)	2.47	2.91 (0.21)	11.72 (0.85)	5.08	5.95 (0.43)
	33.5	3.51 (0.77)	10.86	3.81 (0.84)	2.16 (0.48)	33.27	7.19 (1.59)
43	5.5	38.39 (1.24)	2.30	8.84 (0.29)	38.21 (1.23)	5.42	20.72 (0.67)
	33.5	3.47 (0.76)	10.86	3.77 (0.83)	2.15 (0.47)	33.27	7.15 (1.57)
44	5.5	48.30 (1.33)	2.30	11.12 (0.31)	48.71 (1.29)	5.42	26.41 (0.70)
	25.0	6.16 (0.76)	0.65	0.40 (0.05)	5.00 (0.61)	32.78	16.41 (2.01)
45	6.0	35.98 (0.85)	2.47	8.90 (0.21)	35.92 (0.85)	5.08	18.23 (0.43)
	35.0	10.36 (0.90)	12.43	12.88 (1.12)	6.40 (0.56)	33.70	21.57 (1.88)
46	5.0	61.91 (1.99)	2.32	14.38 (0.46)	61.46 (1.98)	5.99	36.81 (1.18)
	22.0	0.34 (0.02)	4.81	0.16 (0.01)	0.34 (0.02)	6.59	0.22 (0.02)
47	6.0	17.87 (0.87)	2.47	4.42 (0.22)	17.82 (0.87)	5.08	9.05 (0.44)
	33.0	2.48 (0.62)	8.49	2.11 (0.53)	1.61 (0.41)	32.25	5.20 (1.31)
48	5.5	25.10 (1.30)	2.30	5.78 (0.30)	24.05 (1.32)	5.42	13.04 (0.71)
	33.5	4.90 (0.67)	10.86	5.33 (0.73)	2.91 (0.40)	32.26	9.37 (1.28)
49	4.0	299.23 (17.97)	2.19	65.58 (3.94)	81.21 (4.81)	5.91	47.98 (2.84)
	16.0	0.43 (0.03)	4.85	0.21 (0.02)	0.37 (0.03)	6.57	0.24 (0.02)
50	4.5	72.30 (5.12)	2.29	16.52 (1.17)	71.04 (5.03)	5.91	41.97 (2.97)
	20.0	0.21 (0.03)	4.95	0.10 (0.01)	0.21 (0.03)	6.65	0.14 (0.02)
51	5.0	16.06 (2.19)	2.32	3.73 (0.51)	111.40 (16.53)	6.38	71.10 (10.55)
	34.0	3.97 (0.77)	12.91	5.12 (1.00)	2.42 (0.44)	31.19	7.54 (1.37)
52	5.0	33.41 (2.05)	2.32	7.76 (0.48)	34.56 (2.02)	5.99	20.69 (1.21)
	31.5	8.11 (0.78)	2.90	2.35 (0.22)	4.49 (0.43)	32.25	14.49 (1.39)
53	6.0	28.42 (0.85)	2.47	7.03 (0.21)	28.54 (0.85)	5.08	14.49 (0.43)
	32.0	4.95 (0.28)	4.49	2.22 (0.13)	2.86 (0.16)	32.25	9.21 (0.52)
54	6.0	42.56 (0.85)	2.47	10.52 (0.21)	41.69 (0.85)	5.08	21.16 (0.43)
	30.5	12.03 (0.32)	0.75	0.90 (0.02)	7.28 (0.20)	27.05	19.68 (0.53)
55	6.0	58.51 (0.84)	2.47	14.47 (0.21)	58.25 (0.84)	5.08	29.57 (0.43)
	33.0	10.76 (0.32)	8.49	9.13 (0.27)	7.14 (0.21)	32.25	23.02 (0.69)
56	6.0	45.19 (0.82)	2.47	11.17 (0.20)	45.17 (0.82)	5.08	22.93 (0.42)
	32.5	7.85 (0.26)	6.36	4.99 (0.17)	4.83 (0.16)	32.25	15.59 (0.52)
57	5.5	42.55 (1.23)	2.30	9.80 (0.28)	42.36 (1.22)	5.42	22.97 (0.66)
	33.0	2.49 (0.61)	8.49	2.11 (0.52)	1.62 (0.40)	32.25	5.22 (1.28)
58	5.0	50.78 (1.88)	2.32	11.79 (0.44)	50.48 (1.86)	5.99	30.23 (1.11)
	35.0	9.46 (0.87)	12.43	11.75 (1.09)	5.82 (0.54)	33.70	19.61 (1.81)
59	5.0	44.20 (2.20)	2.32	10.26 (0.51)	44.37 (2.18)	5.99	26.57 (1.30)
	25.0	2.85 (0.30)	0.65	0.18 (0.02)	2.34 (0.25)	32.78	7.67 (0.81)
60	5.0	38.50 (1.71)	2.32	8.94 (0.40)	38.50 (1.69)	5.99	23.06 (1.01)
	32.5	5.29 (0.75)	6.36	3.37 (0.47)	3.22 (0.46)	32.25	10.38 (1.48)
61	6.0	4.74 (0.75)	2.47	1.17 (0.19)	4.78 (0.75)	5.08	2.43 (0.38)
	32.5	2.90 (0.66)	6.36	1.84 (0.42)	1.75 (0.40)	32.25	5.64 (1.30)
62	5.0	31.44 (1.83)	2.32	7.30 (0.42)	30.21 (1.84)	5.99	18.09 (1.10)
	34.0	3.98 (0.78)	12.91	5.13 (1.00)	2.25 (0.44)	32.78	7.38 (1.44)
63	5.5	38.39 (1.34)	2.30	8.84 (0.31)	38.22 (1.34)	5.42	20.73 (0.72)
	33.5	2.15 (0.31)	10.86	2.34 (0.33)	1.34 (0.19)	33.27	4.44 (0.63)

Table 5
(Continued)

Region	V_s[a] (km s^{-1})	Mass Flow (120 K)[b] (10^2 $M_\odot$ yr^{-1})	t_{cool}(120 K)[c] (10^2 yr)	M(120 K)(H_2)[d] (10^5 $M_\odot$)	Mass Flow (50 K)[b] (10^2 $M_\odot$ yr^{-1})	t_{cool}(50 K)[c] (10^2 yr)	M(50 K)(H_2)[d] (10^5 $M_\odot$)
64	5.5	59.82 (1.40)	2.30	13.78 (0.32)	59.59 (1.39)	5.42	32.31 (0.75)
	35.0	7.00 (1.05)	12.43	8.70 (1.30)	4.35 (0.64)	33.70	14.67 (2.17)
65	6.0	49.63 (0.86)	2.47	12.27 (0.21)	239.69 (23.37)	6.38	152.99 (14.91)
	33.5	3.25 (0.77)	10.86	3.53 (0.84)	28.62 (0.89)	4.83	13.82 (0.43)
66	4.0	302.73 (27.28)	2.19	66.35 (5.98)	284.03 (25.45)	6.38	181.29 (16.24)
	6.5	32.18 (1.07)	2.59	8.34 (0.28)	32.24 (1.06)	4.83	15.56 (0.51)
67	4.0	356.40 (27.33)	2.19	78.11 (5.99)	334.08 (25.50)	6.38	213.24 (16.28)
	6.5	19.19 (1.08)	2.59	4.97 (0.28)	19.29 (1.07)	4.83	9.31 (0.52)
68	5.0	60.79 (2.23)	2.32	14.12 (0.52)	60.35 (2.21)	5.99	36.14 (1.32)
	19.5	0.23 (0.03)	4.92	0.11 (0.02)	0.23 (0.03)	6.49	0.15 (0.02)
69	5.5	28.78 (1.30)	2.30	6.63 (0.30)	28.65 (1.30)	5.42	15.54 (0.70)
	33.0	2.48 (0.60)	8.49	2.11 (0.51)	1.61 (0.39)	32.25	5.19 (1.27)
70	5.0	38.78 (2.10)	2.32	9.01 (0.49)	38.50 (2.08)	5.99	23.06 (1.25)
	22.5	0.13 (0.02)	4.80	0.06 (0.01)	0.13 (0.02)	6.48	0.08 (0.01)
71	5.5	5.49 (1.26)	2.30	1.26 (0.29)	5.47 (1.25)	5.42	2.96 (0.68)
	33.5	3.49 (0.74)	10.86	3.79 (0.81)	1.83 (0.39)	32.25	5.89 (1.26)
72	5.0	22.45 (2.19)	2.32	5.21 (0.51)	22.30 (2.17)	5.99	13.35 (1.30)
	33.5	3.67 (0.74)	10.86	3.98 (0.80)	2.26 (0.45)	33.27	7.52 (1.51)
73	4.0	347.82 (18.20)	2.19	76.23 (3.99)	327.93 (17.19)	6.38	209.31 (10.97)
	20.5	0.18 (0.03)	4.87	0.09 (0.01)	0.19 (0.03)	6.65	0.13 (0.02)
74	5.5	37.44 (1.36)	2.30	8.62 (0.31)	37.32 (1.35)	5.42	20.24 (0.73)
	34.0	3.83 (0.82)	12.91	4.95 (1.06)	2.32 (0.49)	33.27	7.73 (1.64)
75	4.0	497.35 (22.40)	2.19	109.00 (4.91)	435.85 (23.00)	6.38	278.19 (14.68)
	7.5	6.21 (0.53)	2.78	1.73 (0.15)	8.53 (0.72)	4.86	4.14 (0.35)
76	5.0	118.43 (2.15)	2.32	27.50 (0.50)	117.53 (2.13)	5.99	70.38 (1.28)
	16.5	0.88 (0.04)	4.89	0.43 (0.02)	0.88 (0.04)	6.57	0.58 (0.02)
77	6.0	61.18 (0.84)	2.47	15.13 (0.21)	60.92 (0.83)	5.08	30.92 (0.42)
	33.0	13.62 (0.29)	8.49	11.56(0.25)	8.98 (0.19)	32.25	28.95 (0.62)
78	5.0	90.91 (2.23)	2.32	21.11 (0.52)	90.25 (2.21)	5.99	54.05 (1.32)
	20.0	0.63 (0.03)	4.95	0.31 (0.01)	0.63 (0.03)	6.65	0.42 (0.02)
79	4.0	458.46 (16.78)	2.19	100.48 (3.68)	429.65 (15.83)	6.38	274.24 (10.11)
	17.0	0.40 (0.04)	4.85	0.19 (0.02)	0.42 (0.04)	6.57	0.28 (0.03)
80	4.0	369.33 (16.88)	2.19	80.94 (3.70)	347.66 (15.89)	6.38	221.90 (10.14)
	17.0	0.39 (0.04)	4.85	0.19 (0.02)	0.39 (0.04)	6.61	0.26 (0.03)
81	4.5	98.72 (4.55)	2.29	22.56 (1.04)	97.03 (4.47)	5.91	57.33 (2.64)
	19.5	0.24 (0.03)	4.92	0.12 (0.01)	0.24 (0.03)	6.49	0.16 (0.02)
82	4.5	98.89 (4.35)	2.29	22.60 (0.99)	97.16 (4.27)	5.91	57.41 (2.52)
	17.5	0.38 (0.04)	4.93	0.19 (0.02)	0.38 (0.04)	6.58	0.25 (0.02)
83	4.0	375.89 (14.17)	2.19	82.38 (3.11)	354.34 (13.37)	6.38	226.17 (8.53)
	17.5	0.37 (0.04)	4.93	0.18 (0.02)	0.37 (0.04)	6.58	0.25 (0.02)
84	6.0	3.25 (0.86)	2.47	0.80 (0.21)	3.23 (0.86)	5.08	1.64 (0.44)
	33.5	3.51 (0.77)	10.86	3.81 (0.84)	2.17 (0.48)	33.27	7.20 (1.59)
85	6.5	4.50 (0.66)	2.59	1.17 (0.17)	4.47 (0.66)	4.83	2.16 (0.32)
	33.5	3.56 (0.79)	10.86	3.87 (0.86)	2.21 (0.49)	33.27	7.34 (1.64)
86	4.0	267.80 (18.06)	2.19	58.69 (3.96)	252.09 (17.07)	6.38	160.90 (10.89)
	20.0	0.21 (0.03)	4.95	0.10 (0.01)	0.22 (0.03)	6.49	0.14 (0.02)
87	4.0	430.00 (17.70)	2.19	94.24 (3.88)	405.22 (16.65)	6.38	258.64 (10.63)
	15.0	0.53 (0.05)	4.73	0.25 (0.02)	0.53 (0.05)	6.43	0.34 (0.03)
88	4.0	459.12 (18.90)	2.19	100.62 (4.14)	418.44 (18.25)	6.38	267.08 (11.65)
	8.5	3.94 (0.27)	3.15	1.24 (0.08)	4.96 (0.34)	4.88	2.42 (0.16)
89	5.0	106.52 (2.16)	2.32	24.74 (0.50)	105.72 (2.14)	5.99	63.31 (1.28)
	17.0	0.88 (0.04)	4.85	0.43 (0.02)	0.88 (0.04)	6.61	0.58 (0.02)
90	5.0	138.57 (2.07)	2.32	32.18 (0.48)	137.51 (2.06)	5.99	82.35 (1.23)
	19.5	1.25 (0.03)	4.92	0.61 (0.01)	1.25 (0.03)	6.49	0.81 (0.02)
91	5.0	122.11 (2.08)	2.32	28.36 (0.48)	121.21 (2.07)	5.99	72.59 (1.24)
	21.0	1.06 (0.02)	4.87	0.52 (0.01)	1.06 (0.02)	6.55	0.69 (0.02)
92	4.5	185.61 (4.53)	2.29	42.41 (1.04)	182.45 (4.45)	5.91	107.80 (2.63)
	19.0	0.62 (0.03)	4.91	0.30 (0.01)	0.62 (0.03)	6.66	0.41 (0.02)
93	4.0	486.57 (18.38)	2.19	106.64 (4.03)	453.92 (17.37)	6.38	289.73 (11.09)
	13.5	0.86 (0.06)	4.49	0.39 (0.03)	0.95 (0.07)	6.22	0.59 (0.04)
94	4.0	394.19 (18.73)	2.19	86.39 (4.11)	359.27 (18.17)	6.38	229.32 (11.60)
	8.5	3.83 (0.26)	3.15	1.21 (0.08)	4.80 (0.33)	4.88	2.34 (0.16)
95	4.0	442.31 (18.14)	2.19	96.94 (3.98)	381.08 (18.06)	6.38	243.24 (11.53)

Table 5
(Continued)

Region	V_s[a] (km s^{-1})	Mass Flow (120 K)[b] (10^2 $M_\odot$ yr^{-1})	t_{cool}(120 K)[c] (10^2 yr)	M(120 K)(H_2)[d] (10^5 $M_\odot$)	Mass Flow (50 K)[b] (10^2 $M_\odot$ yr^{-1})	t_{cool}(50 K)[c] (10^2 yr)	M(50 K)(H_2)[d] (10^5 $M_\odot$)
	10.5	2.10 (0.13)	3.67	0.77 (0.05)	4.25 (0.26)	5.11	2.17 (0.13)
96	5.0	65.27 (2.19)	2.32	15.16 (0.51)	64.78 (2.17)	5.99	38.80 (1.30)
	17.5	0.37 (0.04)	4.93	0.18 (0.02)	0.37 (0.04)	6.58	0.25 (0.02)
97	7.0	2.28 (0.54)	2.63	0.60 (0.14)	2.27 (0.53)	4.86	1.10 (0.26)
	33.5	3.59 (0.82)	10.86	3.89 (0.90)	2.24 (0.51)	33.27	7.45 (1.71)
98	7.0	2.74 (0.50)	2.63	0.72 (0.13)	2.73 (0.50)	4.86	1.33 (0.24)
	33.5	3.52 (0.83)	10.86	3.82 (0.90)	2.19 (0.51)	33.27	7.29 (1.71)
99	5.0	24.90 (2.22)	2.32	5.78 (0.52)	24.77 (2.20)	5.99	14.83 (1.32)
	34.0	3.92 (0.78)	12.91	5.06 (1.00)	2.36 (0.47)	33.27	7.86 (1.56)
100	4.0	334.88 (18.18)	2.19	73.39 (3.98)	314.09 (17.11)	6.38	200.48 (10.92)
	20.5	0.19 (0.03)	4.87	0.09 (0.01)	0.20 (0.03)	6.65	0.13 (0.02)
101	4.0	444.27 (18.12)	2.19	97.37 (3.97)	415.47 (17.08)	6.38	265.19 (10.90)
	16.0	0.51 (0.04)	4.85	0.25 (0.02)	0.55 (0.05)	6.53	0.36 (0.03)
102	4.5	213.54 (4.56)	2.29	48.80 (1.04)	209.83 (4.48)	5.91	123.98 (2.65)
	18.5	0.76 (0.03)	4.93	0.38 (0.02)	0.76 (0.03)	6.59	0.50 (0.02)
103	5.0	147.03 (2.13)	2.32	34.14 (0.50)	145.90 (2.12)	5.99	87.37 (1.27)
	19.5	1.20 (0.03)	4.92	0.59 (0.01)	1.21 (0.03)	6.49	0.78 (0.02)
104	5.0	145.44 (2.12)	2.32	33.77 (0.49)	144.35 (2.11)	5.99	86.44 (1.26)
	21.0	1.32 (0.03)	4.87	0.64 (0.01)	1.32 (0.03)	6.55	0.86 (0.02)
105	5.0	115.50 (2.06)	2.32	26.82 (0.48)	114.64 (2.04)	5.99	68.65 (1.22)
	22.0	0.72 (0.02)	4.81	0.35 (0.01)	0.72 (0.02)	6.59	0.47 (0.02)
106	4.0	727.72 (18.00)	2.19	159.49 (3.95)	687.10 (17.00)	6.38	438.57 (10.85)
	16.5	0.76 (0.04)	4.89	0.37 (0.02)	0.75 (0.04)	6.57	0.49 (0.03)
107	4.0	610.22 (18.53)	2.19	133.74 (4.06)	572.02 (17.57)	6.38	365.11 (11.21)
	14.0	0.98 (0.06)	4.64	0.45 (0.03)	1.07 (0.06)	6.33	0.68 (0.04)
108	4.0	691.00 (16.59)	2.19	151.44 (3.64)	652.24 (15.65)	6.38	416.31 (9.99)
	16.0	0.89 (0.04)	4.85	0.43 (0.02)	0.89 (0.04)	6.59	0.58 (0.03)
109	5.0	115.93 (2.45)	2.32	26.92 (0.57)	114.65 (2.43)	5.99	68.65 (1.46)
	20.5	0.50 (0.03)	4.87	0.24 (0.01)	0.53 (0.03)	6.65	0.35 (0.02)
110	5.5	8.17 (1.46)	2.30	1.88 (0.34)	94.45 (18.62)	6.38	60.29 (11.88)
	33.5	3.53 (0.76)	10.86	3.83 (0.83)	2.41 (0.44)	32.09	7.72 (1.40)
111	6.5	4.49 (0.69)	2.59	1.16(0.18)	4.46 (0.69)	4.83	2.16 (0.33)
	33.5	3.54 (0.79)	10.86	3.84 (0.86)	2.20 (0.49)	33.27	7.30 (1.64)
112	6.0	6.52 (1.04)	2.47	1.61 (0.26)	6.48 (1.04)	5.08	3.29 (0.53)
	33.5	3.71 (0.78)	10.86	4.03 (0.85)	2.30 (0.48)	33.27	7.66 (1.61)
113	4.0	203.21 (14.30)	2.19	44.54 (3.13)	192.25 (13.52)	6.38	122.71 (8.63)
	18.0	0.32 (0.03)	4.90	0.16 (0.02)	0.32 (0.03)	6.64	0.21 (0.02)
114	4.0	320.08 (18.07)	2.19	70.15 (3.96)	301.49 (16.99)	6.38	192.43 (10.84)
	17.5	0.38 (0.04)	4.93	0.19 (0.02)	0.38 (0.04)	6.58	0.25 (0.02)
115	4.5	179.43 (4.91)	2.29	41.00 (1.12)	176.33 (4.82)	5.91	104.19 (2.85)
	19.5	0.63 (0.03)	4.92	0.31 (0.01)	0.63 (0.03)	6.49	0.41 (0.02)
116	5.0	142.68 (2.29)	2.32	33.13 (0.53)	141.61 (2.27)	5.99	84.80 (1.36)
	20.5	1.32 (0.03)	4.87	0.64 (0.01)	1.32 (0.03)	6.63	0.87 (0.02)
117	5.0	149.61 (2.11)	2.32	34.74 (0.49)	148.48 (2.10)	5.99	88.91 (1.25)
	20.0	1.51 (0.03)	4.95	0.75 (0.01)	1.51 (0.03)	6.65	1.01 (0.02)
118	4.5	264.16 (4.47)	2.29	60.36 (1.02)	259.57 (4.39)	5.91	153.37 (2.59)
	20.0	1.15 (0.03)	4.95	0.57 (0.01)	1.15 (0.03)	6.65	0.76 (0.02)
119	4.5	238.58 (4.83)	2.29	54.52 (1.10)	234.54 (4.75)	5.91	138.58 (2.81)
	19.5	0.83 (0.03)	4.92	0.41 (0.01)	0.83 (0.03)	6.49	0.54 (0.02)
120	4.5	253.80 (4.60)	2.29	58.00 (1.05)	249.48 (4.52)	5.91	147.41 (2.67)
	18.0	1.03 (0.03)	4.90	0.51 (0.02)	1.03 (0.03)	6.64	0.69 (0.02)
121	5.0	124.78 (2.15)	2.32	28.98 (0.50)	123.32 (2.14)	5.99	73.85 (1.28)
	20.0	0.73 (0.03)	4.95	0.36 (0.01)	0.77 (0.03)	6.49	0.50 (0.02)
122	5.0	129.12 (1.99)	2.32	29.98 (0.46)	128.16 (1.97)	5.99	76.74 (1.18)
	21.0	0.61 (0.02)	4.87	0.30 (0.01)	0.61 (0.02)	6.55	0.40 (0.02)
123	4.0	67.58 (13.12)	2.19	14.81 (2.88)	68.21 (12.28)	6.38	43.54 (7.84)
	25.5	2.98 (0.54)	0.63	0.19 (0.03)	2.37 (0.43)	32.78	7.78 (1.42)
124	5.5	8.03 (1.65)	2.30	1.85 (0.38)	7.99 (1.65)	5.42	4.33 (0.89)
	33.5	3.53 (0.76)	10.86	3.83 (0.83)	2.18 (0.47)	33.27	7.24 (1.57)
125	6.0	5.46 (0.86)	2.47	1.35 (0.21)	5.43 (0.86)	5.08	2.76 (0.44)
	33.5	3.60 (0.78)	10.86	3.90 (0.84)	2.22 (0.48)	33.27	7.38 (1.60)
126	4.0	162.78 (13.87)	2.19	35.68 (3.04)	153.84 (13.09)	6.38	98.19 (8.36)
	21.5	0.16 (0.02)	4.87	0.08 (0.01)	0.15 (0.02)	6.57	0.10 (0.02)

Table 5
(Continued)

Region	V_s[a] (km s^{-1})	Mass Flow (120 K)[b] (10^2 $M_\odot$ yr^{-1})	t_{cool}(120 K)[c] (10^2 yr)	M(120 K)(H_2)[d] (10^5 $M_\odot$)	Mass Flow (50 K)[b] (10^2 $M_\odot$ yr^{-1})	t_{cool}(50 K)[c] (10^2 yr)	M(50 K)(H_2)[d] (10^5 $M_\odot$)
127	4.0	227.58 (18.20)	2.19	49.88 (3.99)	215.19 (17.15)	6.38	137.35 (10.94)
	20.5	0.19 (0.03)	4.87	0.09 (0.01)	0.18 (0.03)	6.63	0.12 (0.02)
128	4.5	127.92 (4.50)	2.29	29.23 (1.03)	125.74 (4.43)	5.91	74.30 (2.61)
	17.0	0.46 (0.04)	4.85	0.22 (0.02)	0.46 (0.04)	6.61	0.31 (0.03)
129	4.5	254.67 (4.93)	2.29	58.20 (1.13)	250.26 (4.84)	5.91	147.87 (2.86)
	19.0	0.92 (0.03)	4.91	0.45 (0.02)	0.92 (0.03)	6.66	0.61 (0.02)
130	5.0	137.62 (2.12)	2.32	31.96 (0.49)	136.58 (2.10)	5.99	81.79 (1.26)
	19.5	1.11 (0.03)	4.92	0.55 (0.01)	1.11 (0.03)	6.49	0.72 (0.02)
131	5.0	124.45 (2.08)	2.32	28.90 (0.48)	123.54 (2.06)	5.99	73.98 (1.23)
	20.0	0.84 (0.03)	4.95	0.42 (0.01)	0.84 (0.03)	6.65	0.56 (0.02)
132	4.5	272.62 (4.81)	2.29	62.30 (1.10)	266.63 (4.73)	5.91	157.54 (2.80)
	19.0	1.01 (0.03)	4.91	0.50 (0.01)	1.06 (0.03)	6.59	0.70 (0.02)
133	5.0	122.38 (2.30)	2.32	28.42 (0.53)	121.49 (2.28)	5.99	72.75 (1.36)
	19.0	0.90 (0.03)	4.91	0.44 (0.01)	0.90 (0.03)	6.66	0.60 (0.02)
134	5.0	123.74 (2.26)	2.32	28.74 (0.53)	122.85 (2.25)	5.99	73.57 (1.34)
	19.5	0.83 (0.03)	4.92	0.41 (0.01)	0.83 (0.03)	6.49	0.54 (0.02)
135	4.5	266.75 (3.83)	2.29	60.96 (0.88)	262.14 (3.77)	5.91	154.89 (2.23)
	20.0	0.54 (0.03)	4.95	0.27 (0.02)	0.54 (0.03)	6.65	0.36 (0.02)
136	5.5	7.46 (1.24)	2.30	1.72 (0.29)	7.42 (1.23)	5.42	4.03 (0.67)
	33.5	3.57 (0.76)	10.86	3.88 (0.83)	2.20 (0.47)	33.27	7.33 (1.56)
137	5.5	9.39 (1.29)	2.30	2.16 (0.30)	9.35 (1.28)	5.42	5.07 (0.70)
	33.5	3.44 (0.76)	10.86	3.74 (0.83)	1.80 (0.40)	32.25	5.81 (1.29)
138	5.0	23.98 (1.75)	2.32	5.57 (0.41)	23.81 (1.74)	5.99	14.26 (1.04)
	33.5	3.74 (0.75)	10.86	4.06 (0.82)	2.31 (0.47)	33.27	7.69 (1.55)
139	5.5	22.96 (1.36)	2.30	5.29 (0.31)	22.86 (1.35)	5.42	12.39 (0.73)
	33.0	2.61 (0.61)	8.49	2.21 (0.52)	1.70 (0.40)	32.25	5.48 (1.29)
140	4.5	137.20 (4.94)	2.29	31.35 (1.13)	134.86 (4.86)	5.91	79.68 (2.87)
	16.5	0.51 (0.04)	4.89	0.25 (0.02)	0.51 (0.04)	6.57	0.34 (0.03)
141	4.5	221.42 (4.67)	2.29	50.60 (1.07)	217.55 (4.59)	5.91	128.54 (2.71)
	17.5	0.95 (0.04)	4.93	0.47 (0.02)	0.95 (0.04)	6.58	0.62 (0.02)
142	5.0	150.29 (2.10)	2.32	34.90 (0.49)	149.19 (2.08)	5.99	89.34 (1.25)
	20.5	1.01 (0.02)	4.87	0.49 (0.01)	1.01 (0.02)	6.63	0.67 (0.01)
143	5.0	138.33 (2.05)	2.32	32.12 (0.48)	137.34 (2.04)	5.99	82.25 (1.22)
	20.5	1.00 (0.02)	4.87	0.49 (0.01)	1.00 (0.02)	6.63	0.66 (0.01)
144	4.0	893.29 (17.72)	2.19	195.78 (3.88)	241.53 (4.74)	5.91	142.71 (2.80)
	17.0	0.85 (0.04)	4.85	0.41 (0.02)	0.71 (0.03)	6.64	0.47 (0.02)
145	4.0	851.21 (18.08)	2.19	186.56 (3.96)	799.40 (17.11)	6.38	510.24 (10.92)
	15.5	0.81 (0.05)	4.71	0.38 (0.02)	0.87 (0.05)	6.43	0.56 (0.03)
146	4.0	555.47 (17.44)	2.19	121.74 (3.82)	525.26 (16.47)	6.38	335.26 (10.51)
	22.5	0.35 (0.02)	4.80	0.17 (0.01)	0.35 (0.02)	6.48	0.22 (0.01)
147	5.5	10.11 (1.24)	2.30	2.33 (0.28)	10.07 (1.23)	5.42	5.46 (0.67)
	33.5	3.46 (0.76)	10.86	3.76 (0.83)	1.81 (0.40)	32.25	5.84 (1.29)
148	5.5	8.69 (1.23)	2.30	2.00 (0.28)	8.65 (1.22)	5.42	4.69 (0.66)
	33.5	3.49 (0.76)	10.86	3.79 (0.83)	2.15 (0.47)	33.27	7.16 (1.56)
149	5.5	11.41 (1.07)	2.30	2.63 (0.25)	11.36 (1.06)	5.42	6.16 (0.58)
	33.0	2.70 (0.61)	8.49	2.29 (0.52)	1.76 (0.40)	32.25	5.66 (1.28)
150	5.5	16.06 (1.07)	2.30	3.70 (0.25)	16.00 (1.07)	5.42	8.67 (0.58)
	33.0	2.50 (0.61)	8.49	2.12 (0.52)	1.61 (0.40)	32.25	5.21 (1.28)
151	5.5	29.61 (1.33)	2.30	6.82 (0.31)	29.47 (1.33)	5.42	15.98 (0.72)
	33.5	3.42 (0.76)	10.86	3.71 (0.83)	2.11 (0.47)	33.27	7.03 (1.56)
152	4.0	619.91 (21.11)	2.19	135.86 (4.63)	205.95 (4.72)	5.91	121.69 (2.79)
	7.5	8.91 (0.48)	2.78	2.48 (0.13)	1.21 (0.07)	6.33	0.76 (0.05)
153	5.0	160.69 (2.14)	2.32	37.32 (0.50)	159.48 (2.12)	5.99	95.50 (1.27)
	20.5	1.03 (0.03)	4.87	0.50 (0.01)	1.03 (0.03)	6.63	0.68 (0.02)
154	5.0	159.68 (2.09)	2.32	37.08 (0.48)	158.51 (2.07)	5.99	94.92 (1.24)
	22.5	0.81 (0.03)	4.80	0.39 (0.01)	0.81 (0.03)	6.48	0.53 (0.02)
155	4.0	691.00 (24.76)	2.19	151.44 (5.43)	580.99 (26.25)	6.38	370.84 (16.75)
	7.0	11.58 (0.74)	2.63	3.05 (0.19)	17.23 (1.07)	4.83	8.32 (0.52)
156	4.0	559.37 (17.65)	2.19	122.59 (3.87)	525.44 (16.63)	6.38	335.38 (10.62)
	17.5	0.36 (0.03)	4.93	0.18 (0.02)	0.38 (0.03)	6.61	0.25 (0.02)
157	5.0	54.06 (2.20)	2.32	12.55 (0.51)	52.68 (2.21)	5.99	31.55 (1.32)
	35.0	4.57 (0.80)	12.43	5.68 (0.99)	2.46 (0.43)	32.34	7.95 (1.38)
158	4.0	84.83 (16.59)	2.19	18.59 (3.64)	75.06 (15.71)	6.38	47.91 (10.03)

Table 5
(Continued)

Region	V_s[a] (km s^{-1})	Mass Flow (120 K)[b] (10^2 $M_\odot$ yr^{-1})	t_{cool}(120 K)[c] (10^2 yr)	M(120 K)(H_2)[d] (10^5 $M_\odot$)	Mass Flow (50 K)[b] (10^2 $M_\odot$ yr^{-1})	t_{cool}(50 K)[c] (10^2 yr)	M(50 K)(H_2)[d] (10^5 $M_\odot$)
	34.0	4.05 (0.78)	12.91	5.23 (1.00)	2.23 (0.43)	32.34	7.21 (1.38)
159	5.5	6.75 (1.23)	2.30	1.55 (0.28)	6.71 (1.23)	5.42	3.64 (0.66)
	33.5	3.62 (0.76)	10.86	3.94 (0.83)	2.24 (0.47)	33.27	7.45 (1.56)
160	5.0	18.02 (2.04)	2.32	4.19 (0.47)	125.86 (15.42)	6.38	80.34 (9.85)
	34.0	3.94 (0.77)	12.91	5.08 (1.00)	2.40 (0.44)	30.76	7.40 (1.34)
161	5.0	21.45 (2.21)	2.32	4.98 (0.51)	21.31 (2.20)	5.99	12.76 (1.32)
	33.5	3.81(0.75)	10.86	4.13 (0.82)	2.35 (0.47)	33.27	7.82 (1.55)
162	4.0	289.66 (13.97)	2.19	63.48 (3.06)	273.92 (13.19)	6.38	174.83 (8.42)
	20.0	0.21 (0.03)	4.95	0.10 (0.01)	0.21 (0.03)	6.65	0.14 (0.02)
163	4.5	155.07 (5.08)	2.29	35.44 (1.16)	152.40 (4.98)	5.91	90.05 (2.94)
	18.5	0.28 (0.03)	4.93	0.14 (0.02)	0.28 (0.03)	6.59	0.18 (0.02)
164	5.0	133.99 (2.13)	2.32	31.12 (0.49)	133.01 (2.11)	5.99	79.65 (1.26)
	21.5	0.55 (0.02)	4.87	0.27 (0.01)	0.55 (0.02)	6.57	0.36 (0.02)
165	5.0	149.80 (2.11)	2.32	34.79 (0.49)	148.69 (2.10)	5.99	89.04 (1.25)
	22.0	0.72 (0.02)	4.81	0.34 (0.01)	0.72 (0.02)	6.59	0.47 (0.02)
166	5.0	105.85 (2.22)	2.32	24.58 (0.52)	105.11 (2.21)	5.99	62.94 (1.32)
	22.0	0.50 (0.02)	4.81	0.24 (0.01)	0.50 (0.02)	6.59	0.33 (0.02)
167	4.0	539.22 (16.38)	2.19	118.18 (3.59)	506.55 (15.43)	6.38	323.32 (9.85)
	22.5	0.28 (0.01)	4.80	0.14 (0.01)	0.30 (0.01)	6.59	0.20 (0.01)
168	4.0	413.76 (18.24)	2.19	90.68 (4.00)	340.44 (19.59)	6.38	217.29 (12.50)
	16.5	0.40 (0.05)	4.89	0.19 (0.02)	2.56 (0.32)	5.11	1.31 (0.16)
169	4.0	159.94 (13.95)	2.19	35.05 (3.06)	153.99 (13.08)	6.38	98.29 (8.35)
	25.0	2.87 (0.53)	0.65	0.19 (0.03)	2.37 (0.44)	32.09	7.61 (1.40)
170	5.5	12.64 (1.33)	2.30	2.91 (0.31)	12.59 (1.33)	5.42	6.83 (0.72)
	33.0	2.67 (0.61)	8.49	2.27 (0.52)	1.74 (0.40)	32.25	5.61 (1.29)
171	5.5	12.65 (1.23)	2.30	2.91 (0.28)	145.35 (15.10)	6.38	92.78 (9.64)
	33.5	3.56 (0.76)	10.86	3.87 (0.83)	0.13 (0.02)	6.48	0.09 (0.01)
172	5.0	22.76 (2.08)	2.32	5.29 (0.48)	22.66 (2.06)	5.99	13.57 (1.23)
	34.0	3.93 (0.77)	12.91	5.07 (1.00)	2.37 (0.46)	33.27	7.88 (1.55)
173	4.0	313.75 (13.96)	2.19	68.76 (3.06)	296.72 (13.17)	6.38	189.39 (8.41)
	22.0	0.14 (0.02)	4.81	0.07 (0.01)	0.14 (0.02)	6.59	0.10 (0.02)
174	4.0	521.41 (17.02)	2.19	114.27 (3.73)	491.31 (16.02)	6.38	313.59 (10.23)
	19.0	0.28 (0.03)	4.91	0.14 (0.01)	0.28 (0.03)	6.66	0.19 (0.02)
175	5.0	100.71 (2.11)	2.32	23.39 (0.49)	100.00 (2.10)	5.99	59.89 (1.26)
	21.5	0.33 (0.02)	4.87	0.16 (0.01)	0.33 (0.02)	6.57	0.22 (0.02)
176	5.0	114.64 (2.11)	2.32	26.62 (0.49)	113.82 (2.10)	5.99	68.16 (1.26)
	22.0	0.53 (0.02)	4.81	0.26 (0.01)	0.53 (0.02)	6.59	0.35 (0.02)
177	4.0	806.92 (16.58)	2.19	176.85 (3.63)	760.92 (15.62)	6.38	485.68 (9.97)
	19.0	0.72 (0.03)	4.91	0.35 (0.02)	0.72 (0.03)	6.66	0.48 (0.02)
178	4.0	650.51 (16.49)	2.19	142.57 (3.61)	613.51 (15.53)	6.38	391.59 (9.91)
	22.5	0.42 (0.02)	4.80	0.20 (0.01)	0.42 (0.02)	6.48	0.27 (0.02)
179	4.0	588.99 (17.49)	2.19	129.09 (3.83)	549.53 (16.52)	6.38	350.75 (10.55)
	30.5	9.51 (0.76)	0.75	0.71 (0.06)	5.57 (0.45)	27.05	15.06 (1.21)
180	5.5	14.06 (1.06)	2.30	3.24 (0.25)	160.61 (13.12)	6.38	102.51 (8.37)
	33.0	2.58 (0.61)	8.49	2.19 (0.52)	2.46 (0.43)	28.05	6.89 (1.22)
181	5.5	16.30 (1.29)	2.30	3.75 (0.30)	16.24 (1.28)	5.42	8.81 (0.70)
	33.0	2.51 (0.61)	8.49	2.13 (0.52)	1.63 (0.40)	32.25	5.25 (1.29)
182	4.0	325.80 (16.45)	2.19	71.40 (3.61)	307.89 (15.49)	6.38	196.52 (9.89)
	22.0	0.21 (0.02)	4.81	0.10 (0.01)	0.21 (0.02)	6.59	0.14 (0.02)
183	4.0	475.03 (16.13)	2.19	104.11 (3.54)	448.82 (15.20)	6.38	286.47 (9.70)
	19.5	0.32 (0.03)	4.92	0.16 (0.01)	0.31 (0.03)	6.49	0.20 (0.02)
184	4.0	538.34 (17.94)	2.19	117.98 (3.93)	508.07 (16.87)	6.38	324.29 (10.77)
	18.5	0.26 (0.03)	4.93	0.13 (0.02)	0.26 (0.03)	6.59	0.17 (0.02)
185	4.0	616.56 (16.83)	2.19	135.13 (3.69)	584.78 (15.90)	6.38	373.25 (10.15)
	22.0	0.24 (0.02)	4.81	0.12 (0.01)	0.24 (0.02)	6.59	0.16 (0.01)
186	4.0	710.37 (16.79)	2.19	155.69 (3.68)	670.69 (15.80)	6.38	428.09 (10.09)
	20.5	0.38 (0.02)	4.87	0.18 (0.01)	0.37 (0.02)	6.63	0.25 (0.02)
187	4.0	958.59 (16.74)	2.19	210.09 (3.67)	904.99 (15.77)	6.38	577.64 (10.06)
	20.5	0.58 (0.03)	4.87	0.28 (0.01)	0.57 (0.03)	6.63	0.38 (0.02)
188	4.0	881.65 (18.94)	2.19	193.23 (4.15)	813.83 (18.26)	6.38	519.45 (11.65)
	8.5	5.03 (0.26)	3.15	1.58 (0.08)	6.32 (0.32)	4.88	3.08 (0.16)
189	4.0	823.23 (16.43)	2.19	180.42 (3.60)	779.49 (15.52)	6.38	497.53 (9.91)
	21.0	0.52 (0.02)	4.87	0.25 (0.01)	0.51 (0.02)	6.55	0.34 (0.02)

Table 5
(Continued)

Region	V_s[a] (km s^{-1})	Mass Flow (120 K)[b] (10^2 $M_\odot$ yr^{-1})	t_{cool}(120 K)[c] (10^2 yr)	M(120 K)(H_2)[d] (10^5 $M_\odot$)	Mass Flow (50 K)[b] (10^2 $M_\odot$ yr^{-1})	t_{cool}(50 K)[c] (10^2 yr)	M(50 K)(H_2)[d] (10^5 $M_\odot$)
190	5.0	88.54 (2.19)	2.32	20.56 (0.51)	88.02 (2.17)	5.99	52.71 (1.30)
	35.0	10.52 (0.85)	12.43	13.08 (1.05)	6.51 (0.52)	33.70	21.95 (1.76)
191	5.5	13.70 (1.33)	2.30	3.15 (0.31)	13.73 (1.32)	5.42	7.44 (0.72)
	32.5	2.85 (0.67)	6.36	1.81 (0.42)	1.73 (0.41)	32.25	5.57 (1.32)
192	5.5	22.44 (1.25)	2.30	5.17 (0.29)	22.34 (1.24)	5.42	12.11 (0.67)
	33.5	3.67 (0.76)	10.86	3.99 (0.82)	2.27 (0.47)	33.27	7.55 (1.56)
193	5.5	39.06 (1.21)	2.30	8.99 (0.28)	38.89 (1.20)	5.42	21.09 (0.65)
	33.0	2.52 (0.61)	8.49	2.14 (0.52)	1.63 (0.40)	32.25	5.26 (1.28)
194	5.5	52.85 (1.23)	2.30	12.17 (0.28)	52.66 (1.23)	5.42	28.55 (0.67)
	35.0	10.16 (0.81)	12.43	12.63 (1.00)	6.28 (0.50)	33.70	21.16 (1.67)
195	5.0	92.90 (2.27)	2.32	21.57 (0.53)	93.29 (2.24)	5.99	55.87 (1.34)
	24.5	10.43 (0.52)	0.65	0.68 (0.03)	8.83 (0.44)	30.76	27.16 (1.35)
196	4.0	832.55 (18.77)	2.19	182.46 (4.11)	786.26 (17.63)	6.38	501.86 (11.25)
	22.5	0.45 (0.02)	4.80	0.21 (0.01)	0.44 (0.02)	6.48	0.29 (0.01)
197	4.0	948.66 (20.14)	2.19	207.91 (4.42)	878.54 (19.37)	6.38	560.75 (12.37)
	8.5	5.39 (0.27)	3.15	1.70 (0.09)	6.74 (0.34)	4.88	3.29 (0.17)
198	17.5	1.20 (0.04)	4.93	0.59 (0.02)	1.18 (0.04)	6.58	0.78 (0.02)
	4.0	1000.00 (0.00)	2.19	219.16 (0.00)	1000.00 (0.00)	6.38	638.28 (0.00)
199	5.0	145.99 (2.28)	2.32	33.90 (0.53)	144.97 (2.26)	5.99	86.81 (1.35)
	20.0	0.66 (0.03)	4.95	0.33 (0.01)	0.66 (0.03)	6.65	0.44 (0.02)
200	5.0	111.11 (2.11)	2.32	25.80 (0.49)	110.31 (2.09)	5.99	66.06 (1.25)
	20.5	0.49 (0.03)	4.87	0.24 (0.01)	0.49 (0.03)	6.63	0.33 (0.02)
201	4.0	289.56 (33.40)	2.19	63.46 (7.32)	276.95 (31.31)	6.38	176.77 (19.99)
	6.0	26.79 (1.75)	2.47	6.62 (0.43)	26.62 (1.73)	5.08	13.51 (0.88)
202	6.0	9.37 (0.84)	2.47	2.32 (0.21)	9.39 (0.84)	5.08	4.77 (0.42)
	32.5	2.71 (0.66)	6.36	1.72 (0.42)	1.63 (0.41)	32.25	5.24 (1.31)
203	4.0	281.63 (18.31)	2.19	61.72 (4.01)	266.75 (17.27)	6.38	170.26 (11.03)
	16.5	0.45 (0.04)	4.89	0.22 (0.02)	0.45 (0.04)	6.57	0.29 (0.03)
204	4.0	445.75 (16.88)	2.19	97.69 (3.70)	422.32 (15.94)	6.38	269.56 (10.18)
	17.0	0.37 (0.04)	4.85	0.18 (0.02)	0.37 (0.04)	6.61	0.25 (0.02)
205	4.0	517.93 (19.03)	2.19	113.51 (4.17)	490.28 (17.93)	6.38	312.94 (11.44)
	8.0	5.88 (0.33)	2.93	1.72 (0.10)	5.87 (0.33)	4.88	2.87 (0.16)
206	4.0	551.87 (21.63)	2.19	120.95 (4.74)	523.11 (20.41)	6.38	333.89 (13.03)
	7.0	13.16 (0.59)	2.63	3.47 (0.16)	13.15 (0.59)	4.86	6.39 (0.29)
207	16.0	1.40 (0.04)	4.85	0.68 (0.02)	1.36 (0.04)	6.59	0.90 (0.03)
	4.0	1000.00 (0.00)	2.19	219.16 (0.00)	1000.00 (0.00)	6.38	638.28 (0.00)
208	18.0	1.20 (0.03)	4.90	0.59 (0.02)	1.18 (0.03)	6.64	0.78 (0.02)
	4.0	1000.00 (0.00)	2.19	219.16 (0.00)	1000.00 (0.00)	6.38	638.28 (0.00)
209	19.0	1.26 (0.03)	4.91	0.62 (0.01)	1.24 (0.03)	6.66	0.82 (0.02)
	4.0	1000.00 (0.00)	2.19	219.16 (0.00)	1000.00 (0.00)	6.38	638.28 (0.00)
210	7.5	15.13 (0.37)	2.78	4.21 (0.10)	14.48 (0.37)	4.84	7.00 (0.18)
	4.0	1000.00 (0.00)	2.19	219.16 (0.00)	1000.00 (0.00)	6.38	638.28 (0.00)
211	4.0	644.31 (25.70)	2.19	141.21 (5.63)	609.29 (24.19)	6.38	388.90(15.44)
	6.5	18.86 (0.90)	2.59	4.89 (0.23)	18.87 (0.89)	4.83	9.11 (0.43)
212	4.0	310.45 (25.13)	2.19	68.04 (5.51)	295.11 (23.51)	6.38	188.36 (15.00)
	6.5	12.63 (0.89)	2.59	3.27 (0.23)	12.59 (0.88)	4.83	6.08 (0.43)

Notes.
[a] Model Shock Velocity.
[b] Mass flow through the shock for gas above $T = 120$ K (or 50 K) to allow comparison with previous analysis.
[c] Cooling time for gas above $T = 120$ K (or 50 K).
[d] Total mass of gas shock heated above $T = 120$ K (or 50 K).

components (Figures 12(B), (D), and (F)). Overall there is a relatively flat kinetic energy deposition from the slow shocks from south to north, despite the decrease in overall shock velocities. There is also an indication that the fast-shock kinetic energy decreases from south to north.

What could cause these global differences in warm gas properties and energy deposition on such a large scale? The basic picture that has been presented is that of a collision between the intruder galaxy NGC 7318b and a pre-existing, almost linear, tidal H I filament (Williams et al. 2002). We have argued in previous papers (Appleton et al. 2006; Guillard et al. 2009; Paper 1) that the warm H_2 can be understood in terms of the dissipation of mechanical energy through a turbulent cascade from a large-scale high-energy collision through supersonic turbulence to small scales and higher densities. Guillard et al. (2009) presented a model in which two phases in the pre-shock

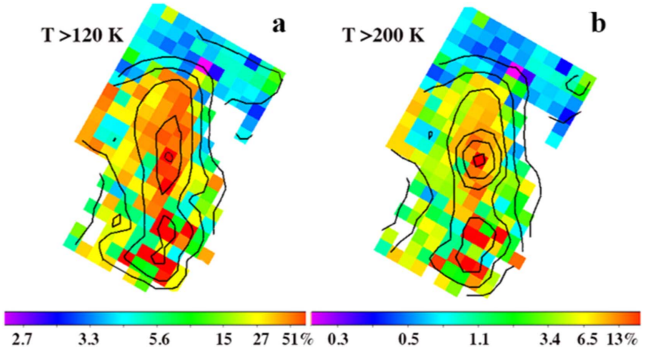

Figure 10. The percentage of warm gas above a given temperature compared with that derived by extrapolating the power law down to 50 K (see text): (a) warm gas above 120 K; contour levels are 10%, 20%, 30%, 40%, 50%, and 60%; (b) for hotter gas with $T > 200$ K, with levels of 1%, 2.5%, 5%, 10%, 15%, and 20%. The plot shows that the warm gas fraction rises along the shock ridge as predicted by the models of Guillard et al. (2009). A smaller fraction is heated to higher temperatures near the shock center. Note also that the region to the east (left) also contains a higher fraction of warm gas in the region of the so-called "AGN bridge."

gas were present in the H I filament before compression by the intruder galaxy. Slightly overdense regions would be compressed by the high-speed shock from the intruder galaxy and would lead to molecular cloud formation on grains that would survive the compression. On the other hand, regions that were originally very underdense would be shock-heated to millions of degrees (generating X-ray emission as observed), and the grains would be destroyed (Guillard et al. 2009). This simple picture provides a working model of the system.

The large extent of the H_2 in the north–south direction is consistent with idea of NGC 7318b colliding with a long tidal filament. The collision, which is believed to be primarily toward the observer from behind the group, may have occurred first in the northern part of the filament, and the point of impact may have progressed along the filament in a southerly direction. The fact that the northern part of the H_2 filament is cooler and heated by lower velocity shocks implies that the energy has had more time to dissipate than in the south, where one might believe most of the current action is.

The northern part of the filament also contains a larger mass of warm gas, which radiates in the lower-*J* lines. This may be related to the structure of the initial target material before the collision of the intruder, implying a density gradient along that filament that is now reflected in an increase in cooler gas. Given the short cooling time of the molecular gas (typically 1000 yr—see Table 5), we might expect this material to continue to cool rapidly. It is interesting that the northern part of the filament contains the extragalactic star-forming region called "SQ-A." SQ-A is the only region of the whole filament that contains significant quantities of H I. Also, unlike the rest of the filament (Konstantopoulos et al. 2014), this is one of the few regions where significant current star formation is occurring (star formation rate $= 1.5\ M_\odot\ \mathrm{yr}^{-1}$; Xu et al. 2003). This may imply that this part of the filament may have cooled sufficiently for H I to re-form and scattered star formation to be initiated. Indeed, Gallagher et al. (2001) showed that SQ-A contains star clusters with a range of ages dating from the initial collision of NGC 7318a with the group (20 Myr ago) to much more recent activity. In fact recent observations support the earlier work (S. Gallagher 2017, private communication), which suggests that star formation activity in the main filament, though currently quite weak, is very recent, and may be increasing in intensity with time.

Previous studies (Cluver et al. 2010; Iglesias-Páramo et al. 2012) suggest a higher level of star formation not just in SQ-A but also, to a lesser degree, in the southern part of the filament, near position 54 of Figure 1(b). Temperatures of the warm gas are a little higher there, but the study by Appleton et al. (2013; region D of that paper) shows that both H_2/PAH and [C II]/PAH ratios are inconsistent with photodissociation regions dominating the H_2 heating there. Indeed, although the H_2 is warmer in that region, the heating is not confined to the H II regions, but is more extensive, which suggests that the extra heating is not caused by star formation.

The structure of the main filament is quite different in the east–west direction, as we have shown. Perhaps surprising is the extent of the gas in the easterly direction, where it continues to the edge of our grid. Long-low observations with IRS extended further to the east than the short-low observations, and so we know that the warm H_2 continues eastward. In Paper 1 we suggested that the eastward extent of the emission was part of a "bridge" to NGC 7319 (see Figure 1(a)). However, such a bridge would have to be quite broad since we detect warm H_2 as far north as position 212 (estimated temperatures of $T_1 = 143$ K and $T_2 = 463$ K). This suggests that a large volume of gas is caught up in the shock heating.

It is worth considering the implications of the kinetic energy deposition in the warm gas. Both across and along the main H_2 filament (the main shock of Figure 1(a)), within each element the kinetic energy deposited every 500–1000 yr (the gas cooling time–see Table 5) is $10^{43.5-44.5}$ J per observational element (6.2 kpc^2). Summing over the whole observed region gives 6.3×10^{46} J (6.3×10^{53} erg), and a total energy flow through the shocks in the warm gas of 4.4×10^{36} W (4.4×10^{43} erg s^{-1}). The total H_2 line luminosity from the whole region (summing over the detected 0–0 S(0)–S(5) lines) is 1.3×10^{35} W (1.3×10^{42} erg s^{-1}), and so the efficiency of conversion of kinetic energy in the shocks into warm H_2 line luminosity is ~3%.

7.1. Connection between Large-scale Gas Kinematics and Regions of Maximal Heating

An interesting question is whether the regions of maximal heating in the shocks (as measured by, for example, the distribution of warm H_2 gas fraction) bears any connection to the large-scale dynamics of the Quintet system. NGC 7318b is colliding with intergroup gas at about 1000 km s^{-1}; Guillard et al. (2009) proposed that, through a turbulent cascade, energy is being transferred to smaller scales and low velocities where a significant fraction of the energy escapes through rotational H_2 and far-IR fine-structure emission (Appleton et al. 2013).

The shock modeling refers to the microscale (parsec scale or smaller) shocks, which represent some of the smallest scales in a turbulent cascade. The large-scale kinematically broad lines measured in the ionized and diffuse molecular gas likely represent the largest velocities and scales in the turbulent cascade. In our picture of the turbulent cascade, we consider the broader lines as being composed of a multitude of narrow molecular shocks and turbulent eddies (<30 km s^{-1}) spread over the full range of observed large-scale stirring (caused by the larger scale collision of NGC 7318a).

If energy is indeed being fed down from large to small scales, then those regions of the gas that show large global

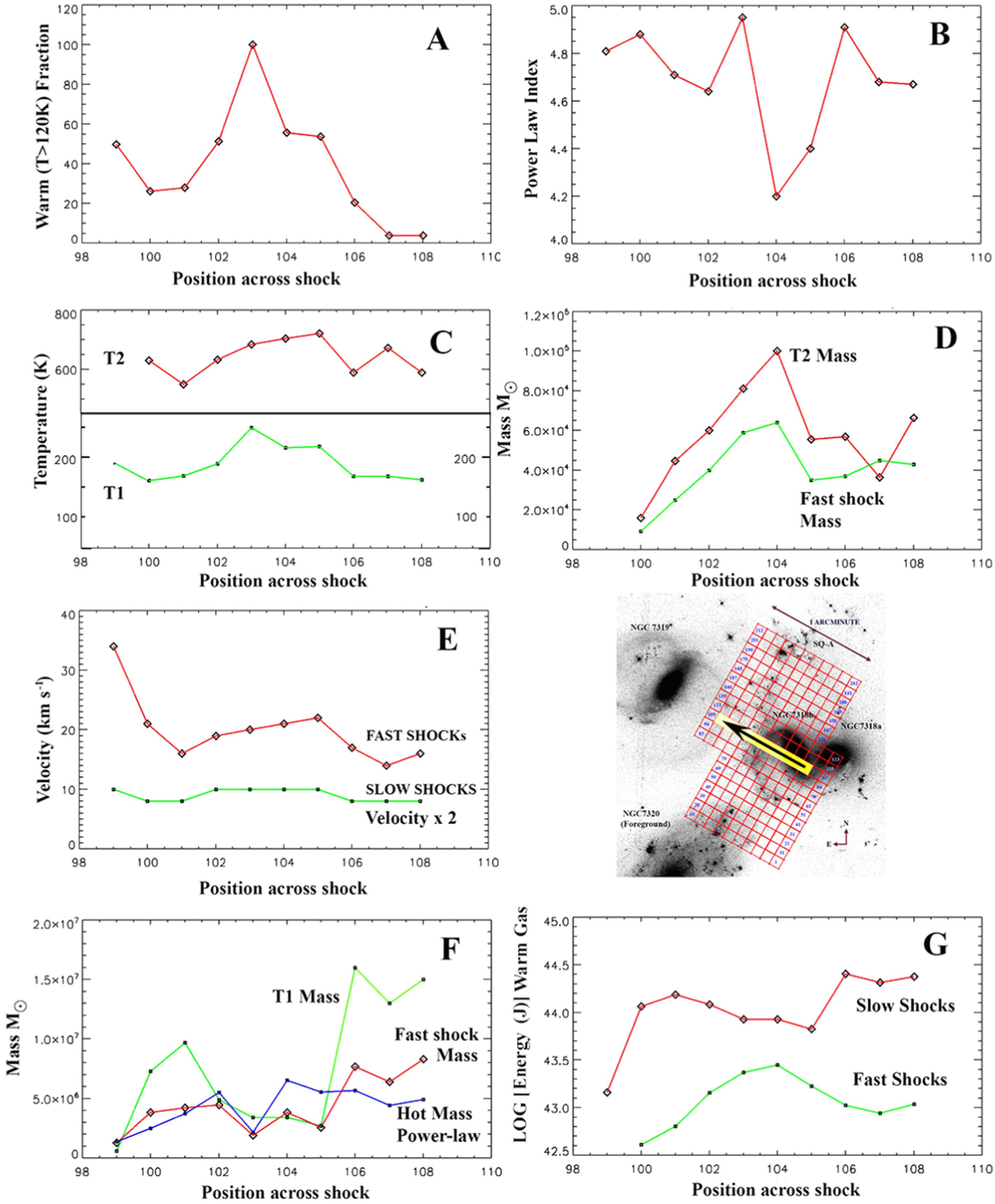

Figure 11. Sectional slices across the H_2 filament following the arrow in the inset image for: (A) warm H_2 fraction for $T > 120$ K, (B) power-law index of H_2 (see text), (C) warm (T_2, red line) and cooler (T_1, green line) temperature distributions derived from two-temperature fits, (D) mass of warm H_2 associated with the warm (T_2, red line) and fast shock (green line) components, showing similar distributions, (E) velocities of the fast (red line) and slower shocks (green line, velocities multiplied by 2 to show structure) needed to excite the H_2, (F) gas mass associated with the cooler T_1 component (green line), the fast shock component (red line), and the warm ($T > 120$ K) power-law mass (blue line), and (G) the kinetic energy in the warm ($T > 120$ K) H_2 component associated with the fast (green line) and slow (red line) shocks.

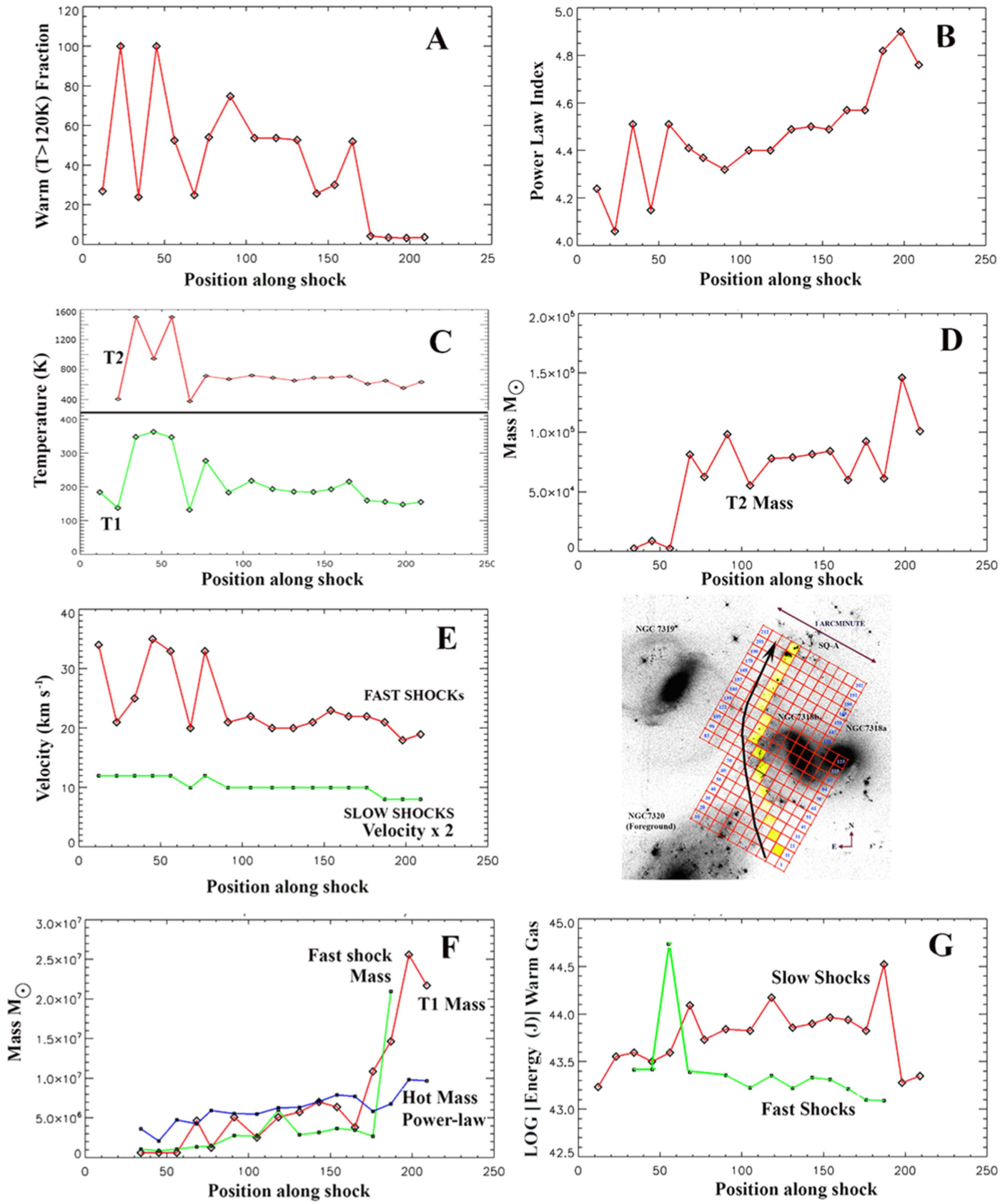

Figure 12. Sectional slices (south to north) along the H_2 filament following the arrow in the inset image for: (A) warm H_2 fraction for $T > 120$ K, (B) power-law index of H_2 (see text), (C) warm (T_2, red line) and cooler (T_1, green line) temperature distributions derived from two-temperature fits, (D) mass of warm H_2 associated with the warm component (T_2, red line), (E) velocities of the fast (red line) and slower shocks (green line, velocities multiplied by 2 to show structure) needed to excite the H_2, (F) gas mass associated with the cooler T_1 component (red line), the fast shock component (green line), and the warm ($T > 120$ K) power-law mass (blue line), and (G) the kinetic energy in the warm ($T > 120$ K) H_2 component associated with the fast (green line) and slow (red line) shocks.

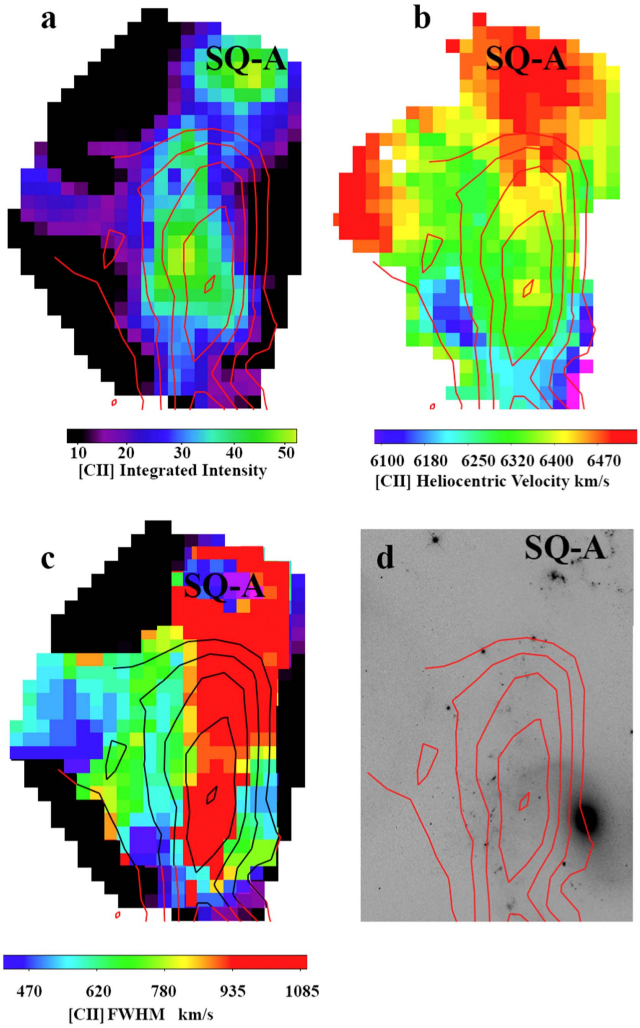

Figure 13. The warm ($T > 120$ K) mass fraction (contours in steps of 10% starting at 10%) compared with the moment maps for the [C II] emission from *Herschel*: (a) [C II] integrated intensity (arbitrary units), (b) [C II] heliocentric mean velocity of the emission (km s^{-1}), (c) [C II] line width (FWHM) (km s^{-1}), and (d) compared with the F665N *HST* visible image. SQ-A, which contains recent star formation, is also shown. The largest warm H_2 gas fraction lies to the west of the main ridge of [C II] emission, but correlates well with the regions of maximum velocity dispersion. This suggests that the [C II] emission maps the leading edge of the main shock, and gas to the west is where the kinetic energy is being deposited, increasing the warm H_2 gas fraction in the post-shocked turbulent regions.

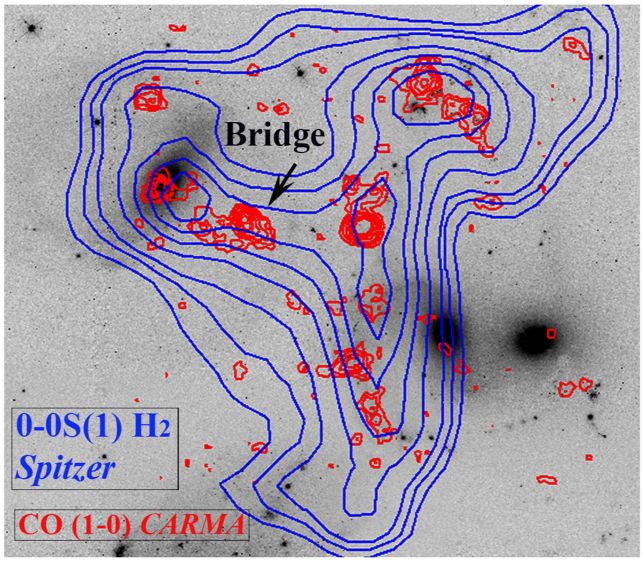

Figure 14. Red contours showing the CARMA CO (1–0) integrated emission (P. Guillard et al. 2017, in preparation) superimposed on the F665N *HST* image (see Guillard et al. 2016 for full discussion of CO emission). Blue contours show the integrated surface density of the 0–0 S(1) 17.08 μm emission covering most of the filament and NGC 7319 from Paper 1. Note that the clumps of CO emission define the main shock but also are scattered along the bridge to NGC 7319.

velocity dispersions should correlate with the regions of maximal heating. Since the velocity resolution of the IRS was not sufficient to map the kinematics of the H_2, we turn to the [C II] emission as a tracer of the diffuse warm molecular gas. It is likely that the warm H_2 is the main collisional partner for the diffuse ionized carbon, leading to the excitation of the [C II] 158 μm transition in the shocked region (Appleton et al. 2013). We show in Figures 13(a)–(c) contours of the warm molecular fraction overplotted on moment maps (intensity, radial velocity map, and line width) for the [C II] emission over the areas that they overlap. Figure 13(d) shows the same contours on the optical image, for reference. From this figure, it is clear that the regions of highest warm fraction correlate most strongly with those regions with the largest (>1000 km s^{-1}) [C II] line width. This implies that the high level of heating of the warm H_2 is strongly correlated with more turbulent line widths (large-scale stirring), as expected from the model of Guillard et al. (2009). We note that the peak in the [C II] emission ridge is offset to the east (Figure 13(a)) from the region of most intense H_2 heating, suggesting that the [C II] emission peaks ahead of the region of maximum kinetic energy dissipation. This would be consistent with the idea that the main shock has a component of motion to the east. It is also consistent with Figure 11, which shows hotter gas, and faster shocks to the east of the main ridge of the peak in the warm gas fraction (Figures 11(D) and (E) compared with 11(A)). Given that the main disturbance driven into the intergalactic gas is a three-dimensional surface, the actual motions in the gas are likely to be quite complex and not easily interpreted without a realistic numerical simulation. None of the existing simulations mentioned in the introduction provides enough detail to explain all the facets of our observations.

7.2. Excitation of Gas in the "Bridge"

Most of the discussion so far has concentrated on the main north–south filament associated with the main shock of Figure 3. We turn now to discuss the emission to the east of the main shock, especially the "bridge" marked in Figure 3. The bridge has been previously detected in X-ray emission and diffuse Hα emission (Trinchieri et al. 2003; Xu et al. 2003), and in warm and cold molecular gas (Paper 1; Guillard et al. 2012). It was not detected in radio continuum emission, unlike the main shock.

As shown in Figure 13(c), by comparison with normal galaxies, even the bridge region has excessively large [C II] line widths of ~500 km s^{-1}, which may explain why so much of the H_2 is excited over such a large area. The bridge structure has its own distinct [C II] kinematics, as can be seen in Figure 13(b), where even in this limited coverage of the full bridge, a strong velocity gradient is seen of 300 km s^{-1} over a

linear scale of ~15 kpc, with the highest velocities seen closer to NGC 7319. The IRAM 30 m CO (1–0) and (2–1) observations of the bridge region by Guillard et al. (2012) show that this region contains multiple broad CO-emitting components with gas at velocities intermediate between those in the extreme north of the group and those in the south (this can been seen also in the [C II] velocity field of Figure 13(b)). Figure 14 shows new, higher resolution observations of some brighter CO condensations within the bridge made with the CARMA interferometer superimposed on the 0–0 S(1) *Spitzer* map. These data (which will be discussed in much more detail in a companion paper: P. Guillard et al. 2017, in preparation) imply a coherent string of multiphase gas emission extending from the Seyfert nucleus of NGC 7319 into the intragroup medium. This raises the possibility that there is an atomic and molecular outflow associated with the nucleus of NGC 7319. A full discussion of this possibility is beyond the scope of the present paper, since both the warm H_2 diagnostics and the [C II] emission do not extend far enough to explore a possible jet-heating scenario.

We have already shown in Section 7 that, as one progresses further east from the main shock, the excitation of the cooler component of the warm H_2 gas remains high. Figures 11(F) and (G) show that in the region of the bridge (positions 106–108) the dominant heating is from slower shocks associated with cooler ($T = 150$ K) gas, which contains a significant mass of H_2. As Figure 11(A) shows, this is also a region with a much lower warm H_2 fraction based on the power-law analysis, suggesting that the balance has shifted to a large reservoir of cooler, but still excited gas in the bridge. We might speculate that the source of heating of this 150 K gas is kinetic energy injected into the medium by an AGN outflow from NGC 7319. This process is evidently less efficient at heating the gas than the collisionally driven shock from NGC 7318b. More work will be needed to explore this possibility in a future paper (Guillard et al. 2016).

8. Conclusions

We have analyzed the two-dimensional excitation distribution of warm molecular hydrogen based on 212 individually extracted mid-IR spectra from *Spitzer* IRS observations of the Stephan's Quintet intergalactic filament. The analysis was conducted on those regions with common IRS short-low and long-low spectral coverage to allow detailed fitting of the molecular excitation. Our main conclusions are as follows.

1. Using simple linear fits to the H_2 excitation diagrams, we have mapped for the first time the temperature and mass distribution of warm H_2 across the intergalactic gas in Stephan's Quintet. The mapped region extends over an area of at least 35×55 kpc^2, and includes the area dominated by shocked gas ahead of the intruder galaxy NGC 7318b. The warmest gas (600–1000 K) is found in the center and to the south of the main filament, with an extension of warm gas extending toward the Seyfert galaxy NGC 7319. The extragalactic star-forming region called "SQ-A," at the northern tip of the main filament, contains the coolest of the warm H_2. A total of 1.1×10^9 $M_\odot$ of warm ($T > 120$ K) H_2 is detected across the entire mapped region, with the largest contribution coming from the cooler ($T \sim 120$–150 K) extended regions on either side of the narrow, highly shocked region, and from SQ-A.
2. We also fit the H_2 excitation diagrams with a power-law distribution of H_2 column density with temperature $dN_{H2} \propto T^{-n}\, dT$. The power-law indices range from $n = 5$ in the north (lower excitation) to lower values (higher excitation) of $n = 4.2$–4.3 in the southern filament. Except in the north, the measured power-law indices are much lower than those seen in normal galaxies, reflecting the high excitation likely resulting from shock heating. The distribution of the lowest power-law values defines a curved band lying to the east and ahead of the intruder galaxy NGC 7318b, as expected if the galaxy is driving a large-scale disturbance into the group-wide gas. The power-law method can self-consistently predict the mass of cold gas at each point in the map. This analysis shows that along the crest of the main filament, where shocks are expected to be the most intense, the warm gas ($T > 120$ K) fraction is between 60% and 100%.
3. We have found that the warm H_2 fraction correlates strongly with the large-scale kinematics of the gas (as measured by the [C II] emission). Where the FWHM of the velocity field is >800 km s^{-1}, the warm H_2 is heated the most strongly. This provides compelling evidence that large-scale turbulent stirring of the diffuse gas caused by the collision of NGC 7318b with the group is able to influence and heat gas on the small scales and at the low velocities needed to excite the rotational H_2 lines.
4. We modeled the H_2 excitation with a molecular shock modeling code (Lesaffre et al. 2013) that computes, along with other common fine-structure lines, the populations of 150 rotation–vibration H_2 levels in parallel to the MHD equations. Although the models are not unique, the best results were achieved with shocks propagating in a molecular medium containing gas with two different pre-shock densities. A system of slow magnetic C-shocks (4–5 km s^{-1}) and faster mainly J-shocks (up to 25 km s^{-1}) was required to explain the observed emission. The models support the idea that the high-speed disturbance caused by the intruder (at 1000 km s^{-1}) has been degraded into millions of slower molecular shocks through the effects of supersonic turbulence.
5. Our results provide a picture of the dissipation of kinetic energy through compressive turbulence (shocks) both along the length of the main filament (north–south) and across it, mainly east–west. Gas temperatures rise, the power-law index flattens, and the velocity of the shocks needed to excite the gas increases as we move from north to south along the main filament. Similar phenomena are seen across the shock in the east–west direction, where the hottest, most intense shocks are seen at the peak of the H_2 surface density, with a slow drop-off on either side. However, although brighter at the peak, the estimated total surface density in warm H_2 actually decreases with this increasing temperature. This may reflect the density structure in the initial pre-shock material that was overrun by the main disturbance from the intruding galaxy, or it may be a result of molecules being increasingly dissociated in the most excited region of the structure.
6. Our analysis shows that the H_2 gas continues to be warm and excited far to the east of the main filament, in the region of the bridge that connects to NGC 7319. Some

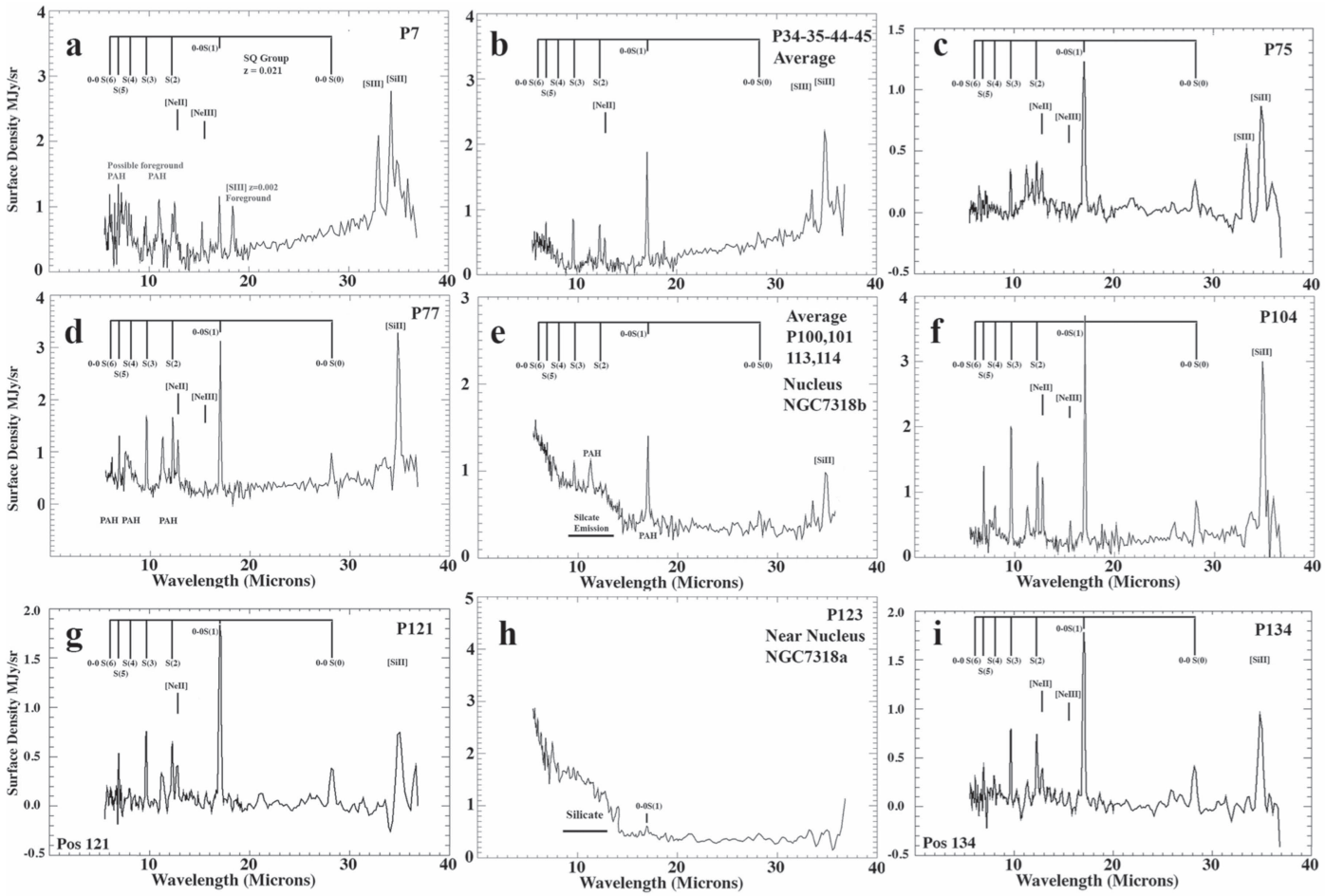

Figure 15. Selected IRS spectra from the spectral grid of Figure 1(b) with main detected lines identified. Spectra from: (a) a near bright H II region in the foreground galaxy NGC 7320, position P7. Note that features of the foreground and background groups are mainly separated; (b) average of four spectra centered on the high-excitation region in the south (P34, 35, 44, 45); (c) behind the main shock (P75); (d) on the main shock–south (P77); (e) the nucleus of NGC 7318b (average P100, 101, 113, 114); (f) main shock–central (P104); (g) AGN bridge region (P121); (h) near the nucleus of NGC 7318a (P123); (i) AGN bridge region (P134).

of this may be related to a known collimated radio jet. Our [C II] observations show an extension of diffuse gas toward the nucleus of this galaxy associated with a kinematically shifting component, but the observations do not extend far enough to conclusively associate this with an outflow. However, our CO (1–0) map from CARMA covers a larger area and shows a string of dense H_2 clumps extending from NGC 7319 in a similar region to the bridge, suggesting a connection with the center of NGC 7319. If the AGN in NGC 7319 is somehow exciting warm molecular hydrogen in that direction, it must have a broad effect, since the warm H_2 gas is extended on a large scale and is generally cooler than the intragroup gas associated with the main filament.

The observations of shock-heated gas in Stephan's Quintet emphasize the wealth of information that can be obtained from rest-frame mid-IR molecular lines, and may point the way toward future studies of turbulent gas at higher redshift with the *James Webb Space Telescope*, *SPICA,* and other possible future facilities. Systems with similar or more powerful rotational H_2 lines were discovered toward the end of the *Spitzer* cryogenic mission. These include a wide range of environments from nearby shock-excited systems and groups (Appleton et al. 2006; Peterson et al. 2012; Cluver et al. 2013; Alatalo et al. 2014), low-redshift radio galaxies (Ogle et al. 2007, 2010, 2014; Nesvadba et al. 2010; Guillard et al. 2012b; Lanz et al. 2015), and central cluster galaxies (Egami et al. 2006; Donahue et al. 2011). It is interesting that the most powerful H_2 emission found to date has been from the Spiderweb protocluster at $z = 2.15$ (Ogle et al. 2012), and from stacked IRS spectra of $z \sim 2$ galaxies (Fiolet et al. 2010). Although the emission mechanism for the high-z gas is not yet clear, the IRS points the way toward potentially important discoveries in the future (Appleton et al. 2009; Guillard et al. 2015).

One question that is raised by the current observations is that of the dominance of molecular hydrogen cooling versus IR fine-structure lines. For example, in the pioneering work of Santoro & Shull (2006), these authors describe how the initial formation of the first galaxy-sized clumps of gas is dominated by cooling from mid- and far-IR rest-frame fine-structure lines (principally [Si II] 34.8 μm, [C II] 157.7 μm and [O I] 63.2/145.5 μm), once the metallicity increases above a critical value (typically $Z > 10^{-3}$ solar). In such a case, the initial collapse of the first clouds would radiate mainly in the metal fine-structure lines, with the mid-IR H_2 lines playing a minor role in the cooling. However, once the collapse is initiated,

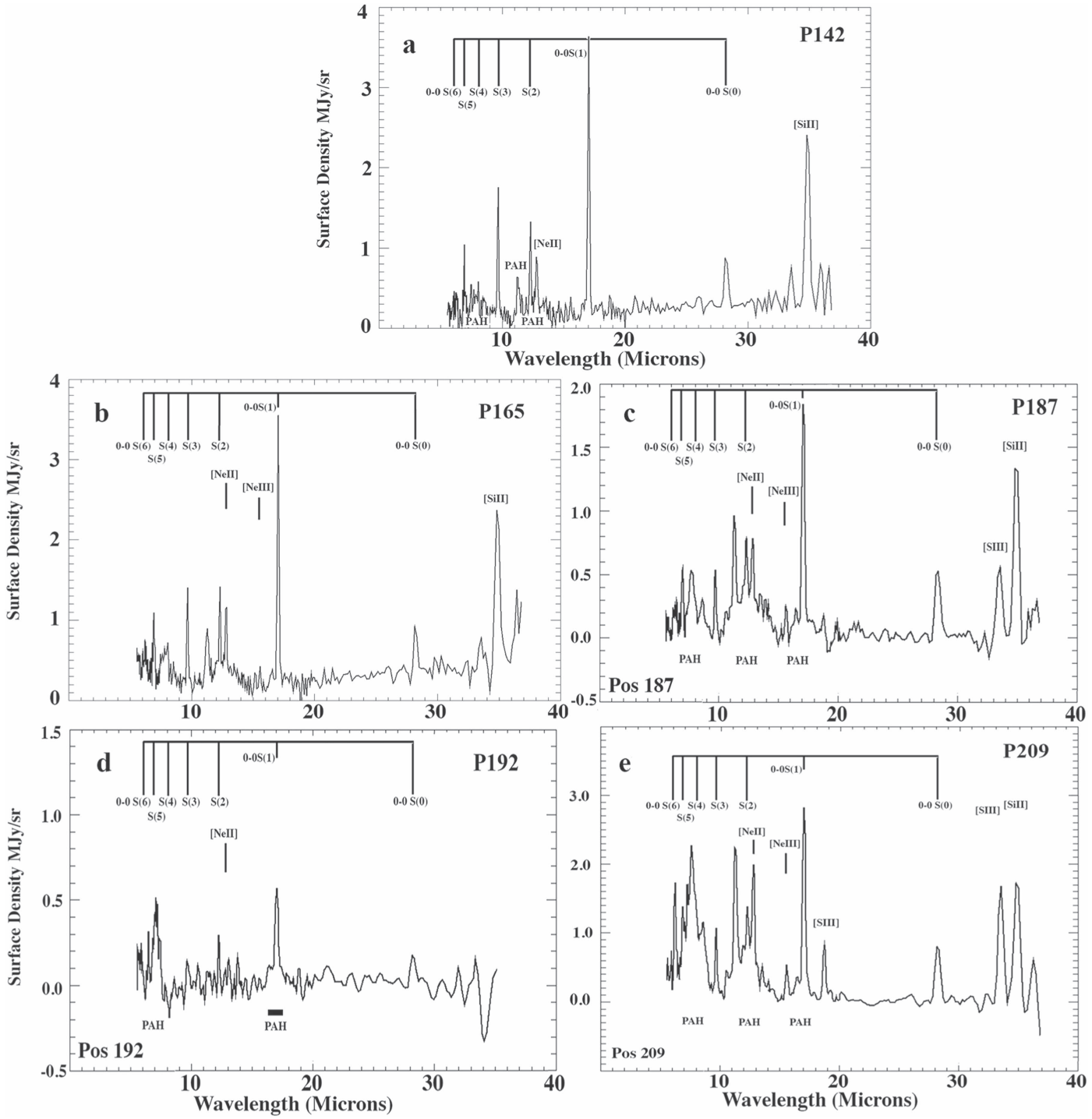

Figure 16. Selected IRS spectra from the spectral grid of Figure 1(b) with main detected lines identified. Spectra from: (a) the main shock–north (P142); (b) the main shock further north (P165); (c) the main shock and beginning of SQ-A complex, including rising PAH features indicating some heating from star formation (P187); (d) in the northern stellar loop from NGC 7318a (P192)—note very faint H_2 lines; (e) SQ-A region (P209) and stronger PAHs.

many complex processes, including shocks and turbulence, could rapidly change the conditions in the gas. Our purely molecular models of Stephan's Quintet's shock (Guillard et al. 2009; Lesaffre et al. 2013, and the current paper) predict comparable H_2 and [C II] line luminosities, as observed (Appleton et al. 2013), even in regions of much higher metallicity than those expected in primordial clouds. A lesson from the Stephan's Quintet system is that the collision of NGC 7318b with a mainly H I tidal arm has resulted in an almost total transformation of the H I into H_2 in 10–20 Myr (see Guillard et al. 2009). We have also shown here that most of the kinetic energy is bound up in the coolest gas heated by low-velocity ($V \sim 4$–$5\ \mathrm{km\ s^{-1}}$) shocks. If low-velocity shocks form at the end-point of a turbulent cascade in gas accreting within dark-matter halos, the H_2 lines may again become important in the cooling of the gas, perhaps forming H_2-bright hotspots. Models investigating conditions in shocked gas with low metallicity are being investigated with this in mind

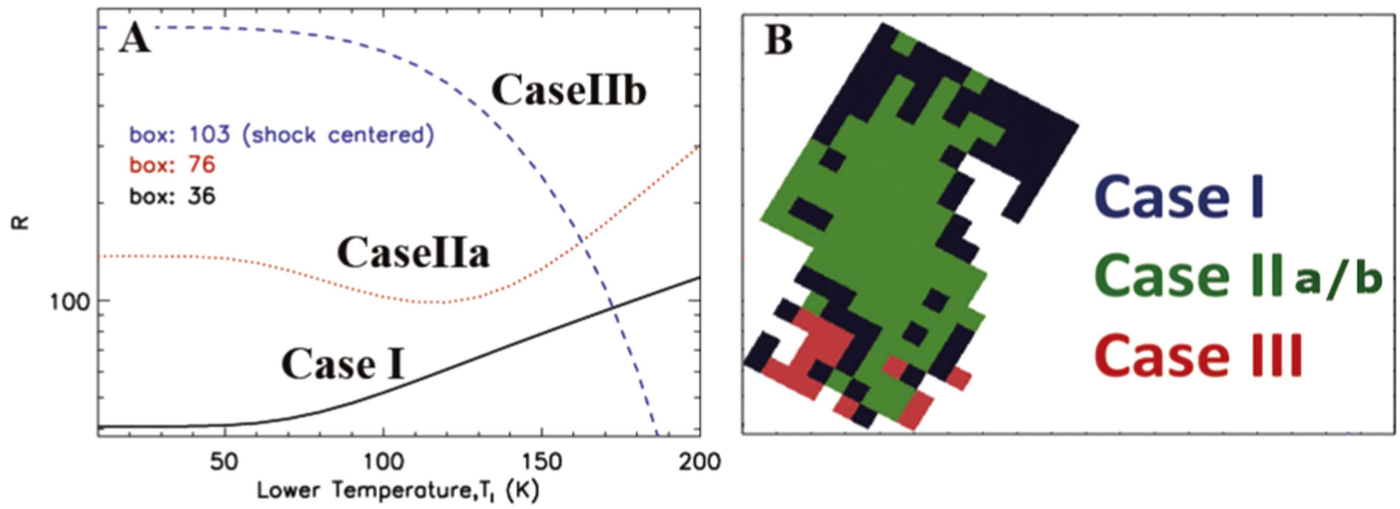

Figure 17. (A) The difference between the model-derived and the observed H_2 line ratios (R) as a function of lower temperature to determine T_ℓ. The black solid, red dotted, and blue dashed curves represent different cases. For the case of the black curve we adopt the value of $T_\ell = 50$ K. The red and blue curves occur in warm regions, where the temperature of all H_2 molecules is high enough to be traced completely by the mid-IR rotational lines. In such cases we adopt the value of T_ℓ at the temperature where we have the minimum deviation. For instance for the red and blue curves we adopt $T_\ell = 120$ and 198 K, respectively, given by our power-law model. (B) The spatial distribution of the extrapolation methods of cases I–III displayed as a schematic diagram covering the mapped area shown in Figure 1(b) (see text). Case III is where the 0–0 S(0) is not detected but the higher-J levels are, implying high temperatures.

(Guillard et al. 2016), and may help to motivate future far-IR attempts to detect rest-frame H_2 emission at redshifts at or beyond the era of reionization.

This paper is dedicated to the work of James Houck of Cornell University (1940–2015), who was the PI of the *Spitzer* IRS instrument. Without his vision and dedication to building a superb instrument, the work described in this paper would never been possible. This work is based, in part, on observations (and archival observations) made with the *Spitzer Space Telescope,* which is operated by the Jet Propulsion Laboratory, California Institute of Technology under a contract with NASA. The work is also based, in part, on observations made with *Herschel*, a European Space Agency Cornerstone Mission with significant participation by NASA. Partial support for the *Herschel* work was provided by NASA through an award issued by JPL/Caltech. U.L. acknowledges support by the research projects AYA2011-24728 and AYA2014-53506-P financed by the Spanish Ministerio de Economía y Competividad and by FEDER (Fondo Europeo de Desarrollo Regional) and the Junta de Andalucía (Spain) grants FQM108.

Appendix A
IRS Spectra of Various Extraction Regions Shown in Figure 1

IRS spectra of various extraction regions shown in Figure 1 are provided in Figures 15 and 16. The properties derived from these and the full set of spectra are presented in Tables 2–5.

Appendix B
Extrapolating the Mass of Gas to Low Gas Temperatures Using the Power-law Method

The power-law analysis described earlier can also make a prediction about the total molecular mass below 100 K (the practical limit for exciting the lowest 0–0 S(0) H_2 rotational line), since we can extrapolate the mass of gas below which the rotational H_2 emission is excited (see Togi & Smith 2016 for more details). This assumes that the same power law derived for warmer gas can be extrapolated to lower temperatures. Increasing the number of extremely cold H_2 molecules below a certain temperature will cause a change in the total molecular gas mass, but will result in an insignificant change in the mid-IR H_2 rotational-line flux. We define the sensitive temperature, T_s, below which H_2 molecules are too cold to cause substantial changes in the mid-IR rotational-line H_2 excitation diagram. In our analysis three different cases emerge in determining T_s, depending on the individual spectral region explored.

1. Case I. We found that for some positions in the filament, as we decrease the lower temperature T_ℓ, the ratio (R) of the difference between the observed and the model fits decreases continuously, and below a certain temperature (T_s) the deviation becomes insignificant and minor change in the model fit occurs. The parameter, R, is defined as

$$R = \sum_{i=1}^{m} \left(\frac{f_{i,\mathrm{mod}} - f_{i,\mathrm{obs}}}{\sigma_{f_{i,\mathrm{obs}}}} \right)^2, \qquad \text{(B1)}$$

where $f = \ln\left(\frac{N_u/g_u}{(N_u/g_u)_{S(1)}}\right)$, $f_{i,\mathrm{mod}}$ and $f_{i,\mathrm{obs}}$ are the modeled and observed flux ratios for the ith line with uncertainty $\sigma_{f_{i,\mathrm{obs}}}$, and the summation is over all the independent line flux ratios. The black solid curve in Figure 17(A) demonstrates this case. In such a scenario we extrapolate our power-law model to 50 K to calculate the total molecular gas mass. The molecular gas mass calculated by extrapolating our model to 50 K correlates with the molecular gas mass derived using the Galactic CO conversion factor, $\alpha_{\mathrm{CO,Gal}}$ (Togi & Smith 2016)
2. Case IIa. As we decrease the lower temperature, T_ℓ, the value of R decreases, but below a certain temperature it starts increasing and at low temperatures shows no significant change. The red dotted curve in Figure 17(A) demonstrates this case in region 76. The value of R decreases until the lower temperature of about 120 K but

increases in the range 50–120 K and remains almost constant below 50 K. In such a case we adopt the corresponding temperature for T_ℓ, here 120 K, where the deviation is found to be minimum. The presence of excess warm molecular gas due to shocks could be the reason for high T_ℓ, and the complete molecular gas in these regions is traced by the mid-IR H_2 rotational lines.

Case IIb. The blue dashed curve is a similar case but the minimum deviation occurs at very high T_ℓ. This was observed in region 103 (see Figure 1(b)), the central shocked region of the Quintet, where the model yields the best-fit value of $T_\ell = 198$ K. The molecular gas in this central shocked region of the Quintet is heated to a temperature of ~200 K.

3. Case III. In some regions the S(0) line is undetected but there are detections of high-J lines of H_2. The S(1) and higher-J lines of H_2 correspond to energy levels $J \geqslant 3$. High-J levels require high temperatures for excitation, which result in high T_s. In such cases we extrapolate our power-law model to 80 K to calculate the total molecular gas mass. Several ultraluminous infrared galaxies, which are local mergers, with warm dust color temperatures have nondetections of S(0) but detection with good signal-to-noise ratio for high-J rotational lines (Higdon et al. 2006; Stierwalt et al. 2014). In these galaxies we need to extrapolate our power-law model to 80 K to recover the total molecular gas mass in order to be consistent with their dynamical mass estimates (Togi & Smith 2016).

We show in Figure 17(B) a schematic map of the distribution of the various cases over the mapped area. The squares of case I (38%) are dark and occupy mainly the cooler northern part of the mapped region, and the median value of warm mass fraction is only 4%. Cases II (54%, green squares) and Case III (8%, red) occupy the regions where the stronger shocks dominate and have median warm mass fractions of 39% and 27% respectively.

Although we detect H_2 in almost every position observed, there are areas near the western and southern borders of the maps where no warm H_2 is detected, even though it lies within the mapping region. We note that there is potentially another possible scenario, where no rotational H_2 lines are detected at all because the gas has too low a temperature to be detected in the mid-IR. Although this is theoretically possible, we assume instead the simpler explanation that there is no molecular gas at these undetected positions. This is probably justifiable, given that both single-dish and interferometric observations confine the CO-emitting gas to similar regions to the warm H_2 distribution. Furthermore, the C^+ emission (Figure 3), which could potential map CO-dark molecular gas (Wolfire et al. 2010), also seems to follow the same spatial distribution as the warm H_2 emission, and so large quantities of intergalactic "dark" molecules are not strongly favored by the current observations.

References

Alatalo, K., Appleton, P. N., Lisenfeld, U., et al. 2014, ApJ, 795, 159
Allen, R. J., & Hartsuiker, J. W. 1972, Natur, 239, 324
Appleton, P., Armus, L., Blain, A., et al. 2009, The Dark Side of Reionization: Probing Cooling in the Early Universe, 2010 Decadal Survey White Paper, arXiv:0903.1839
Appleton, P. N., Guillard, P., Boulanger, F., et al. 2013, ApJ, 777, 66
Appleton, P. N., Xu, K. C., Reach, W., et al. 2006, ApJL, 639, L51
Bahcall, N. A., Harris, D. E., & Rood, H. J. 1984, ApJL, 284, L29
Bitsakis, T., Charmandaris, V., Appleton, P. N., et al. 2014, A&A, 565, A25
Burton, M. G., Hollenbach, D. J., & Tielens, A. G. G. 1992, ApJ, 399, 563
Cluver, M. E., Appleton, P. N., Boulanger, F., et al. 2010, ApJ, 710, 248 (Paper 1)
Cluver, M. E., Appleton, P. N., Ogle, P., et al. 2013, ApJ, 765, 93
Donahue, M., de Messières, G. E., O'Connell, R. W., et al. 2011, ApJ, 732, 40
Egami, E., Rieke, G. H., Fadda, D., & Hines, D. C. 2006, ApJL, 652, L21
Fedotov, K., Gallagher, S. C., Konstantopoulos, I. S., et al. 2011, AJ, 142, 42
Fiolet, N., Omont, A., Lagache, G., et al. 2010, A&A, 524, 33
Gallagher, S. C., Charlton, J. C., Hunsberger, S. D., Zaritsky, D., & Whitmore, B. C. 2001, AJ, 122, 163
Gao, Y., & Xu, C. 2000, ApJL, 542, L83
Geng, A., Beck, A. M., Dolag, K., et al. 2012, MNRAS, 426, 3160
Guillard, P., Appleton, P. N., Boulanger, F., et al. 2016, A&A, submitted
Guillard, P., Boulanger, F., Cluver, M. E., et al. 2010, A&A, 518, A59
Guillard, P., Boulanger, F., Lehnert, M. D., Appleton, P. N., & Pineau des Forêts, G. 2015, in Proc. Annual Meeting of the French Society of Astronomy & Astrophysics, ed. F. Martins et al., 81 (arXiv:1510.02107)
Guillard, P., Boulanger, F., Pineau des Forêts, G., et al. 2012, ApJ, 749, 158
Guillard, P., Boulanger, F., Pineau Des Forêts, G., & Appleton, P. N. 2009, A&A, 502, 515
Guillard, P., Ogle, P. M., Emonts, B. H. C., et al. 2012, ApJ, 747, 95
Hatziminaoglou, E., Hernán-Caballero, A., Feltre, A., & Piñol Ferrer, N. 2015, ApJ, 803, 110
Higdon, S. J. U., Armus, L., Higdon, J. L., Soifer, B. T., & Spoon, H. W. W. 2006, ApJ, 648, 323
Hollenbach, D., & McKee, C. F. 1979, ApJS, 41, 555
Houck, J. R., Roellig, T. L., van Cleve, J., et al. 2004, ApJS, 154, 18
Hwang, J.-S., Struck, C., Renaud, F., & Appleton, P. N. 2012, MNRAS, 419, 1780
Iglesias-Páramo, J., López-Martín, L., Vílchez, J. M., Petropoulou, V., & Sulentic, J. W. 2012, A&A, 539, A127
Konstantopoulos, I. S., Appleton, P. N., Guillard, P., et al. 2014, ApJ, 784, 1
Lanz, L., Ogle, P. M., Evans, D., et al. 2015, ApJ, 801, 17
Le Bourlot, J., Pineau des Forêts, G., Flower, D. R., & Cabrit, S. 2002, MNRAS, 332, 985
Lesaffre, P., Pineau des Forêts, G., Godard, B., et al. 2013, A&A, 550, A106
Li, M. P., Shi, Q. J., & Li, A. 2008, MNRAS, 391, L49
Lisenfeld, U., Braine, J., Duc, P.-A., et al. 2002, A&A, 394, 823
Moles, M., Marquez, I., & Sulentic, J. W. 1998, A&A, 334, 473
Moles, M., Sulentic, J. W., & Márquez, I. 1997, ApJL, 485, L69
Natale, G., Tuffs, R. J., Xu, C. K., et al. 2010, ApJ, 725, 955
Nesvadba, N. P. H., Boulanger, F., Salomé, P., et al. 2010, A&A, 521, A65
Neufeld, D. A., & Yuan, Y. 2008, ApJ, 678, 974
Nikiel-Wroczyński, B., Soida, M., Urbanik, M., Beck, R., & Bomans, D. J. 2013, MNRAS, 435, 149
Ogle, P., Antonucci, R., Appleton, P. N., & Whysong, D. 2007, ApJ, 668, 699
Ogle, P., Boulanger, F., Guillard, P., et al. 2010, ApJ, 724, 1193
Ogle, P., Davies, J. E., Appleton, P. N., et al. 2012, ApJ, 751, 13
Ogle, P. M., Lanz, L., & Appleton, P. N. 2014, ApJL, 788, L33
O'Sullivan, E., Giacintucci, S., Vrtilek, J. M., Raychaudhury, S., & David, L. P. 2009, ApJ, 701, 1560
Peterson, B. W., Appleton, P. N., Helou, G., et al. 2012, ApJ, 751, 11
Petitpas, G. R., & Taylor, C. L. 2005, ApJ, 633, 138
Pilbratt, G. L., Riedinger, J. R., Passvogel, T., et al. 2010, A&A, 518, L1
Poglitsch, A., Waelkens, C., Geis, N., et al. 2010, A&A, 518, L2
Renaud, F., Appleton, P. N., & Xu, C. K. 2010, ApJ, 724, 80
Rigopoulou, D., Kunze, D., Lutz, D., Genzel, R., & Moorwood, A. F. M. 2002, A&A, 389, 374
Rodríguez-Baras, M., Rosales-Ortega, F. F., Díaz, A. I., Sánchez, S. F., & Pasquali, A. 2014, MNRAS, 442, 495
Roussel, H., Helou, G., Hollenbach, D. J., et al. 2007, ApJ, 669, 959
Santoro, F., & Shull, J. M. 2006, ApJ, 643, 26
Smith, B. J., & Struck, C. 2001, AJ, 121, 710
Smith, J. D. T., Armus, L., Dale, D. A., et al. 2007a, PASP, 119, 1133
Smith, J. D. T., Draine, B. T., Dale, D. A., et al. 2007b, ApJ, 656, 770
Spitzer, L., Jr., & Zweibel, E. G. 1974, ApJL, 191, L127

Stierwalt, S., Armus, L., Charmandaris, V., et al. 2014, ApJ, 790, 124
Sulentic, J. W., Pietsch, W., & Arp, H. 1995, A&A, 298, 420
Sulentic, J. W., Rosado, M., Dultzin-Hacyan, D., et al. 2001, AJ, 122, 2993
Suzuki, T., Kaneda, H., Onaka, T., & Kitayama, T. 2011, ApJL, 731, L12
Togi, A., & Smith, J. D. 2016, ApJ, 830, 18
Trinchieri, G., Sulentic, J., Breitschwerdt, D., & Pietsch, W. 2003, A&A, 401, 173
Trinchieri, G., Sulentic, J., Pietsch, W., et al. 2005, A&A, 444, 697
van der Hulst, J. M., & Rots, A. H. 1981, AJ, 86, 1775
Williams, B. A., Yun, M. S., & Verdes-Montenegro, L. 2002, AJ, 123, 2417
Wolfire, M. G., Hollenbach, D., & McKee, C. F. 2010, ApJ, 716, 1191
Xu, C. K., Iglesias-Páramo, J., Burgarella, D., et al. 2005, ApJL, 619, L95
Xu, C. K., Lu, N., Condon, J. J., Dopita, M., & Tuffs, R. J. 2003, ApJ, 595, 665